XRD line profile analysis for understanding the influence of cold work on ageing behaviour in 304HCu steel

By

MANOJ KUMAR RAJA
(Enrollment No: ENGG02201104029)

Indira Gandhi Centre for Atomic Research, Kalpakkam

A thesis submitted to the
Board of Studies in Engineering Sciences

In partial fulfillment of requirements
for the Degree of

DOCTOR OF PHILOSOPHY

of

HOMI BHABHA NATIONAL INSTITUTE

January, 2020

Homi Bhabha National Institute
Recommendations of the Viva Voce Committee

As members of the Viva Voce Board, we certify that we have read the dissertation prepared by **Manoj Kumar Raja** entitled **"XRD line profile analysis for understanding the influence of cold work on ageing behaviour in 304HCu steel"** and recommend that it may be accepted as fulfilling the dissertation requirement for the Degree of Doctor of Philosophy.

Chairman-**Dr. G. Amarendra** G. Amarendra **Date:** April 30, 2021

Guide / Convener-**Dr. C. K. Mukhopadhyay** **Date:** 30/04/2021

Co-Guide -**Dr. Anish Kumar** **Date:** 30/4/21

External Examiner- **Prof. Satyam Suwas, IISc, Bangalore** Satyam Suwas **Date:** 30/04/2021

Member 1-**Dr. Arup Dasgupta** **Date:** 30/04/2021

Member 2-**Dr. A. Nagesha** **Date:** 30/4/2021

Member 3-**Dr. S. Rangarajan** **Date:**

Technology Adviser-**Dr. S. Mahadevan** **Date:** 30/4/2021

Final approval and acceptance of this dissertation is contingent upon the candidate's submission of the final copies of the dissertation to HBNI.

I hereby certify that I have read this dissertation prepared under my direction and recommend that it may be accepted as fulfilling the dissertation requirement.

30/4/21

Date: 30/04/2021
Place: Kalpakkam

(Dr. Anish Kumar)
Co-Guide

(Dr. C. K. Mukhopadhyay)
Guide / Convener

STATEMENT BY AUTHOR

This dissertation has been submitted in partial fulfillment of requirements for an advanced degree at Homi Bhabha National Institute (HBNI) and is deposited in the library to be made available to borrowers under rules of the HBNI.

Brief quotations from this dissertation are allowable without special permission, provided that accurate acknowledgement of source is made. Requests for permission for extended quotation from or reproduction of this manuscript in whole or in part may be granted by the Competent Authority of HBNI when in his or her judgment the proposed use of the material is in the interests of scholarship. In all other instances, however, permission must be obtained from the author.

R. Manoj Kumar

(Manoj Kumar Raja)

Date: 31/01/2020
Place: Kalpakkam

DECLARATION

I, hereby declare that the investigation presented in the thesis entitled "XRD line profile analysis for understanding the influence of cold work on ageing behaviour in 304HCu steel" submitted to Homi Bhabha National Institute (HBNI), Mumbai, India, for the award of Doctor of Philosophy in Engineering Sciences, is the record of work carried out by me under the guidance of Dr. C. K. Mukhopadhyay, Head, Non-Destructive Evaluation Division, Metallurgy and Materials Group, Indira Gandhi Centre for Atomic Research, Kalpakkam. The work is original and has not been submitted earlier as a whole or in part for a degree / diploma at this or any other Institution/University.

R. Manoj Kumar

(Manoj Kumar Raja)

Date: 31/01/2020

Place: Kalpakkam

List of publications arising from the thesis

Journals Published

1) **R. Manojkumar**, S. Mahadevan, C. K. Mukhopadhyay and B.P.C. Rao,"Aging behavior of 17-4 PH stainless steel studied using XRDLPA for separating the influence of precipitation and dislocations on microstrain," *J. Mater. Res., 32, 2017, p4263.*

2) **R. Manojkumar**, S. Mahadevan, C. K. Mukhopadhyay and M. N. Singh, "Study on the influence of prior cold work on precipitation behaviour of 304HCu stainless steel during isothermal aging," *Metall. Mater. Trans. A, 50, 2019, p5476*

Communicated:

1) **R. Manojkumar**, S. Mahadevan, C. K. Mukhopadhyay, Anish Kumar and A. K. Sinha, "XRD line profile analysis for characterizing the deformation modified 304HCu steel during isothermal ageing," in *Metall. Mater. Trans. A (communicated paper # E-TP-20-102-A)*

Conference/Symposium

1) **R. Manojkumar**, S. Mahadevan, and C.K. Mukhopadhyay, "Characterizing the ageing behaviour of prior cold worked 304HCu stainless steel using electrical conductivity and X-ray diffraction technique," in *Research Scholars Meet on Materials Science and Engineering of Nuclear Materials , Kalpakkam, May 7-9, 2018*

2) **R. Manojkumar**, S. Mahadevan, A. Viswanath, S. Arun Kumar, and B. Purnachandra Rao, "Application of electrical conductivity as an NDE tool for microstructural evaluation during cold rolling and thermal ageing," in Proc. of *Indian National Seminar and Exhibition on Non Destructive Evaluation NDE-2015, Hyderabad, November 26-28, 2015,* http://www.ndt.net/?id=21108.

3) **R. Manojkumar**, S. Mahadevan, B. P. C. Rao and T. Jayakumar, "A comparative study of broadening observed in aged 17-4 PH steel by modified Williamson Hall approach and Stephen's model," in *1st International Conference on Scattering and Diffraction Techniques for Material Characterization ICSDTMC2013, NIT-Rourkela, December 13-15, 2013.*

R. Manoj kumar

(Manoj Kumar Raja)

Date: 31/01/2020
Place: Kalpakkam

SOLELY DEDICATED TO MY FAMILY MEMBERS AND MENTORS

ACKNOWLEDGEMENTS

This thesis would not have been possible without the support and encouragement of many people who contributed and extended their valuable co-operation in the completion of the research work. I feel short of words in expressing my appreciation for their help at various stages of this work.

I would like to take this opportunity of expressing my sincere gratitude to my thesis supervisors ***Dr. C. K. Mukhopadhyay*** and ***Dr. Anish Kumar***, for their continuous support to my work, encouragement, enthusiasm and immense knowledge. I would specially like to thank ***Dr. S. Mahadevan***, technical advisor of my doctoral committee in defining the problem and scope of this work. Their tremendous zeal, vast knowledge, guidance and infinite patience helped me in my research work and writing this thesis. They have been always a source of motivation for me in difficult times during the research work. I express my deep sense of appreciation for their support and for energizing me to overcome all the hurdles.

I thank my doctoral committee members ***Dr. G. Amarendra***, ***Dr. A. Nagesha***, ***Dr. Arup Dasgupta, and Dr. S. Rangarajan*** for their encouragement, insightful comments and timely suggestions during the course of the thesis work.

I am grateful to ***Dr. B. Purna Chandra Rao***, Director, Fast Reactor Fuel Cycle Facility (FRFCF), IGCAR and ***T. Jayakumar*** former Director, Metallurgy and Materials Group (MMG), IGCAR for initiating me in to this work.

I extend my heartfelt thanks to the present Director, MMG, IGCAR ***Dr. Shaju K. Albert*** and Director, IGCAR ***Dr. A. K. Bhaduri*** for permitting me to pursue the research work for this extended time.

I would like to extend my heartfelt thanks to ***Shri. A. Viswanath,*** and ***Shri P. Durga Prasad*** for sharing their experience and helping me in sample preparation for this work. I would like to acknowledge the contributions of ***Dr. C. R. Das***, MTD in obtaining hardness measurements. ***Shri. S. Arun Kumar, Smt. T. Nivetha*** and ***Shri M. M. Narayanan*** are remembered for all the small contributions they have made.

I thank my fellow colleagues ***Dr. Govind Kumar Sharma, Dr. S. Thirunavukkarasu, Dr. K. V. Rajkumar, Dr. B. Sasi, Dr. Saravanan, Shri G. V. K. Kishore, Shri G. M. S. K. Chaitanya, Shri V. Arjun, other NDED members*** and ***Research scholars*** for their timely help, useful technical discussions, suggestions, and moral support.

Last but not the least, my deepest gratitude is to my family for their support which brings belief and hope into my life. I remember my mother ***Smt. Rama devi*** and mother in law ***Smt. Kanya kumari*** for their sacrifices in taking care of my children during the work. Finally, I express my sincere and heartfelt thanks and appreciation to my wife ***Pragna Lakshmi*** for her love, and commitment. It is also my duty to put on record the love and affection shown by my children ***Praman Krishna Charvik*** and ***Pranam Shiva mayan***. They understood my needs during the last year and motivated me wholeheartedly at home and spared me from their requirements during the thesis.

(**Manoj Kumar Raja)**

Table of contents

LIST OF FIGURES

LIST OF TABLES

ABBREVATIONS

XRD	X-ray Diffraction
TEM	Transmission Electron Microscope
WPPF	Whole Profile Pattern Fitting
WPPM	Whole Powder Pattern Modeling
XRDLPA	XRD line profile analysis
WH	Williamson Hall
mWH	modified Williamson-Hall
WA	Warren-Averbach
PH	Precipitation Hardening
ODS	Oxide-dispersive Strengthened
AUSC	Advanced Ultra Super Critical
304HCu	Cu- modified 304 grade austenitic stainless steel
SEM	Scanning Electron Microscope
JMA	Johnson–Mehl–Avrami
PSF	Profile Shape Function
FWHM	Full Width At Half Maximum
BCC	body centred cubic
FCC	face centred cubic
CW	Cold work
Eqn.	Equation
Fig.	Figure

SYMBOLS

2θ	Diffraction angle
K	Diffraction vector
d_{hkl}	Interplanar spacing between *(hkl)* plane
a	Lattice parameter
δ	Lattice misfit
ε	Misfit strain
D	Crystallite size
α	Microstrain from mWH method
α'	Microstrain from 2nd order mWH method
b	Burgers vector
R_e	outer cut off radius of dislocations
$A(L)$	Fourier coefficient of XRD profile as a function of column length L
$A_S(L)$	Size Fourier coefficient
$A_D(L)$	strain Fourier coefficient
$\langle \varepsilon^2(L) \rangle$	mean square strain
L	Column length
$\bar{c}$	Average contrast factor of dislocations
η	Cauchy content of the pV function
ρ	Dislocation density
f	Precipitate fraction
n	Avrami exponent
k	Reaction rate constant
t	Ageing time
S_{400} & S_{220}	Stephens strain parameters
α_S	Stephens microstrain
H	Hardness
λ	Wave length
σ	Electrical conductivity
GOF	Goodness of Fit
P_0, P_1	Warren Averbach parameters
§	Chapter section

7 Conclusions and future scope

The summary provided in § 4.10 elucidates in detail the comparison of the results obtained from various XRD peak profile analysis approaches in 17-4 PH steel during thermal ageing. In § 5.4, the key results of the influence of prior deformation on precipitation kinetics that takes place in 304HCu steel is presented. The § 6.5 summarizes the key findings obtained from the isothermal ageing studies carried out on prior deformed 304HCu steel. The following section brings out the salient points and compares the results obtained by using XRD line profile analysis, hardness and electrical conductivity.

7.1 Conclusions

- ➢ The study of thermal ageing behaviour of 17-4PH steel by various XRDLPA revealed
  - Linear correlation between microstrain (α') determined form mWH method [based on Eqn. (2.31)] and microstrain (α_S) determined from Stephens phenomenological model.
  - The difference in microstrain ($\Delta\alpha_d$) between strain estimated by Stephens model and mWH method [based on Eqn. (2.30)] shows a linear behaviour with dislocation density (ρ).
  - The dependency of microstrain with column length is derived with an expression of Eqn. (4.2), which includes long range (P_0) and short range (P_1) strain fields along with a second order term.
  - The variation in P_0 is correlated with the variation in strain determined from the mWH method (using Eqn. (2.30) with FWHM) which showed dominant precipitate induced effects.

- The study of isothermal ageing behaviour of prior deformed 304HCu steel revealed
    - Ageing induced precipitation causes increase in hardness and conductivity.
    - The JMA fit for electrical conductivity and hardness are used to study the precipitation kinetics and the accelerated precipitation is attributed to precipitation on dislocations which are formed during deformation.
    - The enhanced changes in electrical conductivity and hardness are attributed to lowering of activation energy by 0.73 and 4.225 kJ/mol or equivalent ageing temperature of 654 and 672 °C due to 10% and 20% cold deformation.
    - The change in lattice parameter in deformation modified 304HCu steel is larger which is attributed to higher precipitation aided by the dislocation nodes that are formed during deformation.
    - The variation in lattice parameter and conductivity with ageing shows similar behaviour which indicates precipitation process.
    - The change in microstrain indicates the microstructural changes due to changes in dislocations and precipitation in 10% and 20% deformation modified 304HCu steel.
- The term P_1 is linearly correlated with dislocation density (ρ) indicating the strain due to dislocations shows 1/L dependence as a function of column length (L). This dependency has been shown in isothermally aged 17-4 PH steel and deformation modified 304HCu steel.

7.2 Future scope

The studies carried out in this work have clearly demonstrated the applicability of the XRD line profile analysis, hardness and electrical conductivity measurements to study ageing induced precipitation in the microstructure under the influence of prior deformation. It would be worthwhile to address the following issues for better understanding:

- The precipitation kinetics of each individual phase can be studied by using multiphase Kolmogorov-JMA model in computational thermodynamics softwares.
- Linking the asymmetric broadening and peak shape obtained from XRD profiles to the microstructural evolution will improve the analysis.
- The study of precipitation kinetics of prior cold worked samples at various temperatures would enable comparing of influence of ageing temperature on deformation enhanced precipitation kinetics.
- The implication of the proposed XRD approach for separating the precipitation and dislocation effects towards microstrain in other precipitation strengthened steels such as Ni-based INCONEL alloy can be studied.
- The varied response of hardness and electrical conductivity due to ageing followed by deformation can be used to separate the effects of precipitation and dislocations.

ABSTRACT

In this study, the X-ray diffraction line profile analysis (XRDLPA) is carried out to understand the influence of dislocations caused during deformation on precipitation behaviour of 304HCu steel. The XRDLPA are used to separate the profile broadening due to the effects of crystallite size and microstrain in a material. Various XRDLPA viz. modified Williamson Hall (mWH) method, Warren-Averbach (WA) method and Stephens phenomenological model are applied to compare the variations in microstrain obtained. Towards this objective, isothermally aged 17-4PH steel is considered for comparative analysis of microstrain. The 17-4PH steel is a lath martensitic steel with high dislocation structure which shows precipitation dominant strengthening during thermal ageing. The comparative analysis helps to understand the influence of precipitation and dislocations on the microstrain in the matrix. From this study the column length dependency of microstrain from WA analysis is derived in terms of long range strain parameter (P_0) and short range strain parameters (P_1 & P_2). The comparative analysis has shown that the long range and short range strain field are related to precipitate induced and dislocation density induced microstrain respectively.

To demonstrate the approach of separating the simultaneous effects due to precipitates and dislocations on microstrain, austenitic structured 304HCu steel is considered. 304HCu steels, under solution annealed condition has very low dislocation density and in order to introduce dislocations, the material is cold deformed. During ageing of prior deformed 304HCu steel both precipitation as well as dislocation annihilation take place.

The precipitates formed in 304HCu steel are affected by prior deformation which is characterized by hardness and electrical conductivity. The hardness and electrical *conductivity vary on ageing at higher temperatures due to precipitation of fine copper rich phases, niobium carbonitrides [Nb(C,N)] and $M_{23}C_6$ phases. The changes observed in hardness and electrical conductivity during isothermal aging at 650 °C of prior deformed 304HCu steel are analysed by using the Johnson-Mehl-Avrami equation. The early peaking of hardness and conductivity in prior cold deformed samples indicate that precipitation kinetics gets accelerated due to formation of precipitates on dislocation nodes which are formed during deformation. The change in reaction rate estimated from variation in conductivity using JMA equation is interpreted as an equivalent lowering of activation energy or as an increase in ageing temperature.*

The XRD peak profiles from high energy synchrotron source of prior cold worked and aged 304HCu steel samples are able to reveal the precipitate peaks of MX and $M_{23}C_6$ phases that are formed during ageing. The precipitation process influences the microstructure by altering the lattice parameter as well as microstrain in the matrix. The observed variation in lattice parameter with ageing is higher in prior deformed 304HCu steel which is attributed to higher precipitation along dislocations. The misfit strain caused by coherent precipitates that are formed during ageing shows contribution to microstrain in all initial conditions of 304HCu steel. The variation in microstrain determined from mWH approach with ageing of prior cold worked 304HCu steel showed dominant dislocation annihilation effects on initial ageing and dominant precipitation effects on further ageing. The validation of column length dependent microstrain determined from WA approach with dislocation density variation is made. Thus, the study enables in understanding the influence of precipitation in the presence of dislocations by determining lattice parameter, microstrain, hardness and electrical conductivity.

Chapter 1

1 Introduction

X-ray diffraction (XRD) is used for many decades and it provides useful information about crystalline solids which are made-up of systematic arrangement of atoms with different Bravais lattice structure. There are different kinds of crystalline solids such as metals and alloys, minerals, inorganic compounds, polymers and organic materials, whose microstructure can be characterized by XRD technique. The microstructure of metals and alloys can directly affect the macroscopic and microscopic properties. When these materials are used for industrial applications, they get exposed to external stresses and structural/lattice imperfections are formed, which in turn change the material properties. Material characterization signifies the role of lattice imperfections in determining the properties of materials. The material properties like mechanical, electrical, thermal, magnetic, optical etc are related to the microstructural features, which can be characterized by different methods of investigation. Besides the application of XRD technique for material characterization, there are several other techniques to characterize materials based on the probe of inspection. The most commonly used characterization techniques are optical microscopy, electron microscopy, positron annihilation, neutron diffraction, eddy current, ultrasonic etc with different probes (light, electron, positron, neutron, electrical current, ultrasonic waves) of inspection. Even though, the electron microscope provides direct imaging of the microstructure of a material under study, the X-ray diffraction (XRD) is still a promising technique which has emerged much before electron microscopy. The evolutionary transformation observed in XRD with availability of synchrotron radiation in X-ray regime with higher brilliance and improvements in analogue to digital detectors has improved the XRD peak resolution with lesser peak aberration. Additionally, the whole diffraction profile pattern using Rietveld refinement method [**1**,**2**] to the synchrotron source based XRD line profile was employed for material characterisation.

1.1 X-ray powder diffraction

In 1895, W.C. Roentgen discovered X-rays while investigating cathode rays from a Crookes tube and observed the fluorescent screen to glow by an invisible rays which he named as 'X' radiation. In 1913, Lawrence Bragg and his father William Henry Bragg proposed that the scattering of X-rays by planes in crystalline materials interfere constructively producing diffraction pattern and is known as Bragg's diffraction [**3**]. This phenomenon occurs because the wavelength of X-rays and spacing between the planes in the crystal are typically having the same order of magnitude. The Bragg's established a relation among diffraction angle (2θ), interplanar distance (d_{hkl}) of (hkl) plane and wavelength (λ) of the incident x-rays based on the condition of constructive interference. The constructive interference occurs when the total path length between pair of waves reflected by neighboring (hkl) planes is equal to an integer multiple of the wavelength and is given as $2d_{hkl} \sin\theta = n\lambda$. Earlier to Bragg, Laue (1912) had carried out the first experiment using white radiation of X-rays on a single crystal and derived Laue equations which reduce to Bragg's law [**4**]. However, most materials are not single crystals and are composed of many crystalline particles oriented in all directions called as powder or polycrystalline. In 1916, Paul Scherrer worked along with his PhD supervisor, Peter Debye and proposed a method known as powder/Debye-Scherrer method for structure analysis of polycrystalline samples using X-rays [**5**]. In 1917, Albert Hull developed this method independently at General Electric Research Laboratory, US [**6**].

The X-ray powder diffraction is a nondestructive technique which gives information about the microstructural features qualitatively like crystal size, strain due to dislocations and strain due to coherent particles; and quantitatively like secondary phase fractions and dislocation density. These microstructural features can be obtained from X-ray line profile broadening or from Fourier coefficients of the XRD peaks. The synchrotron source provides better peak profile resolutions and has been used for carrying out X-ray line profile analysis in the present dissertation.

1.2 Synchrotron Radiation

The principle of synchrotron accelerator is to accelerate the charged particles in circular path, which was first invented by Veksler [**7**] in 1944. In 1945, Edwin McMillan [**8**] developed the first electron synchrotron which emits synchrotron radiation in the ultraviolet regime. In the synchrotron, under the influence of external magnetic field, the charged particles follow curved path due to Lorentz force and can be accelerated in a closed loop. The synchrotron/brehmsstrahlung radiation is an electromagnetic radiation emitted from moving charged particles which are accelerated by applying external magnetic field in a direction perpendicular to their motion. The development of high current synchrotron storage rings which were successfully brought online in 1960s [**9**] has enabled the production of high intense and coherent brehmsstrahlung radiation ranging from radio-frequency to hard X-ray wavelengths.

1.2.1 Indian synchrotron radiation source

India has constructed two synchrotron storage ring facilities (Indus-1 & Indus-2) and Indus-1 was commissioned in the year 1999 [**10**]. The nominal electron current injected in to these two synchrotrons is achieved by a common injector system consisting of a microtron and a booster synchrotron as shown in the schematic (Fig. 1.1). At first, the electrons from the microtron (20 MeV) are accelerated to an energy of 450 MeV in the booster synchrotron. The accelerated electrons from booster synchrotron are continuously injected into Indus-1 till the current reaches a value of 100 mA. For the injection into Indus-2, a 550 MeV beam is extracted from booster synchrotron at every second till the desired current is achieved. Subsequently, the energy of electron beam in Indus-2 is ramped to 2.5 GeV.

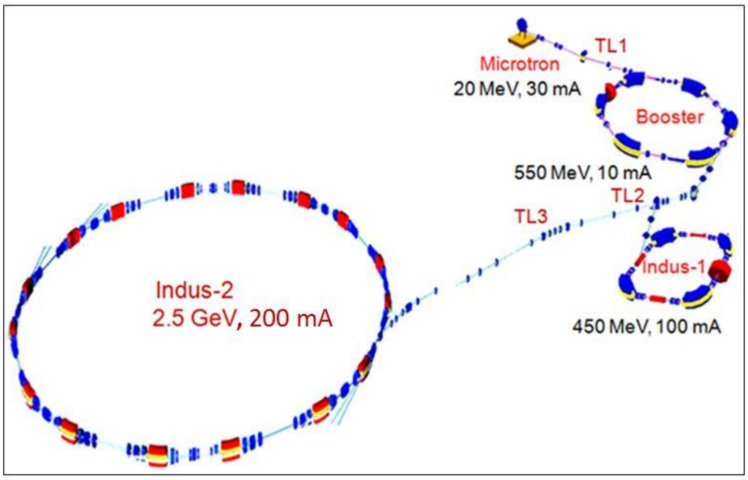

Fig. 1.1 The schematic shows the microtron, booster synchrotron, Indus-1 and Indus-2 storage ring setup along with transfer lines TL-1, TL-2 and TL-3 [**10**].

If electrons of energy in the order of GeV are accelerated with an external magnetic field of Tesla force, the emitted electromagnetic waves will be in the order of X-ray wavelength. The critical wave length of the radiation emitted by electron beam depends up on the energy E (GeV) and applied magnetic field strength B (T). The energy spectrum of synchrotron radiation from 2.5 GeV electron storage ring (Indus-2 synchrotron) at bending magnet (1.5 Tesla) is shown in Fig. 1.2. The critical wave length of the radiation emitted by electron beam of energy E (2.5 GeV), accelerated in a magnetic field of strength B (1.5 T) is given by λ_C (0.198 nm) = $1.86 / E^2 B$.

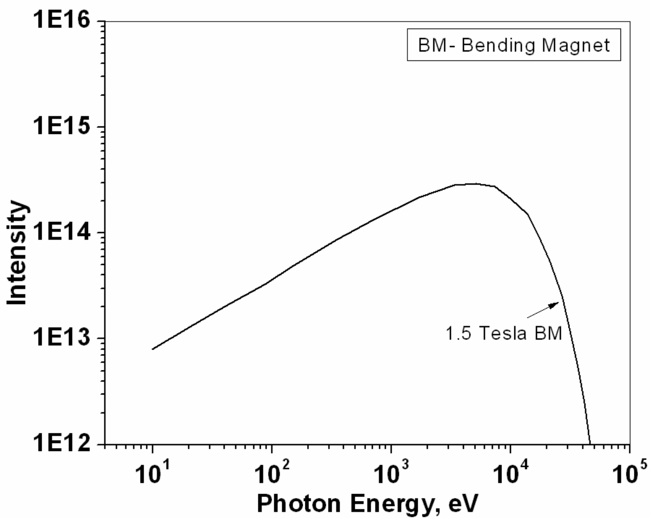

Fig. 1.2 The synchrotron radiation emitted from electron beam of 2.5 GeV energy at bending magnet of 1.5 Tesla field [11].

The usage of synchrotron has increased because of its overall advantages. The advantages of synchrotron radiation over conventional laboratory sources are: broad spectrum, high intense photon flux, sharper resolution, tunability of wave length, less divergence, lower background, and less instrumental effects. The intense highly collimated incident beam coupled with an analyser crystal provides a superior resolution and very good counting statistics and peak-to-background ratio. These characteristics of synchrotron radiation are beneficial to study the microstructural information, such as domain size and lattice deformations [12] and the evolution of low volume fractions of secondary phases under different ageing conditions [13].

1.3 XRD line profile analysis

The X-ray diffraction profile analyses are used for many decades to characterize the microstructural behaviour of materials. The XRD pattern consists of a series of peaks diffracted from different planes. These diffracted peaks obey Bragg’s condition whose scattering amplitude is based on structure factor. The profile parameters like peak position, peak intensity, peak shape and peak width obtained from the XRD pattern can be used to characterize various microstructural features of different materials.

1.3.1 Lattice parameter measurement

The length of the sides and the interaxial angles of a unit cell are called lattice parameters. The lattice parameters which can be determined from XRD peak positions are not constant; and they can vary with change in temperature, pressure and alloying elements. The error in peak position determination occurs mainly due to systematic errors (sample displacement) and random errors (measurement). Precise measurement of lattice parameter (a) determined from Bragg's equation depends on precision in $\sin\theta$. As the error in $\sin\theta$ at higher angles is less, the higher order diffraction lines can be used for accurate determination of lattice parameter. Since, we cannot measure a backward reflected diffraction line i.e., at diffraction angle of $2\theta \sim 180°$, the extrapolated (a) value at higher angle is calculated from the plot of measured (a) value with measured θ value. But the error in measured (a) value is not linear at different diffraction angles and it approaches the true value of (a) at higher angles. The Cohen's method and Nelson-Riley method are most important and frequently used methods among all other extrapolation methods for accurate determination of lattice parameter. These extrapolation methods accomplish the elimination of the systematic errors and reduction in the random errors that exist in the measurement of (a) value.

The accurate determination of lattice parameter provides information about true density of the material, interstitial or substitutional solid solutions and can be used for determining thermal-expansion coefficient [**14**]. The study of lattice parameter at different ageing conditions has been carried out by various authors [**15**,**16**,**17**]. The increase in lattice parameter was observed in iron ball milled powder at different milling speed, which was attributed to the surface energy of the crystals [**15**]. The lattice parameter was used as a complimentary way of studying the precipitation of intermetallics that occur during thermal ageing of Ni based superalloy Inconal 625 [**16**]. Khan et al. [**17**] studied the variation in lattice parameter of Ni based super alloy with ageing and it was attributed to the change in phase composition.

1.3.2 Phase identification and quantification analysis

The indexing of XRD peaks with *hkl* value of a primary phase aids in the identification and presence of additional phases that exist in the matrix. Any unknown pattern of the secondary phases is compared with the reference pattern which are published as powder diffraction File (PDF) in International Centre for Diffraction Data (ICDD). Alexander and Klug [**18**] reported a theoretical basis of X-ray absorption in the quantification of phases. The peak intensity of a particular phase depends upon its concentration. When there are different phases present in the sample, then the integrated intensity for i^{th} phase is proportional to its volume fraction (V_i) as given by

$$I_i = \frac{K_2 R_i^{hkl} V_i}{2\mu_i} \quad \ldots \quad (1.1)$$

where the total volume fraction is

$$\sum_{i=1}^{n} V_i = 1 \quad \ldots \quad (1.2)$$

K_2 is an instrumental factor, R is the theoretical intensity and μ_i is absorption coefficient of that particular phase.

There are different quantitative phase analysis methods among which the two most important methods are the direct comparison method and the internal standard method [**14**]. In all these methods, the common feature of measurement of volume fraction of a particular phase depends upon the measurement of ratio of the intensity of diffraction line of that phase with that of the reference phase, also known as reference intensity ratio (RIR). So, the reference intensity ratio (RIR) is calculated using Eqn. (1.1) for different phases and by substituting these values in Eqn. (1.2), one can determine the volume phase fraction of that particular phase.

1.3.3 X-ray line profile broadening

In powder diffraction pattern, the profile broadening is a convolution of instrumental and sample effects. The physical parameters i.e., crystallite size and strain mainly contribute to the specimen broadening. In general, the specimen broadening due to crystallite size is symmetrical in nature and varies as a function of diffraction angle. The specimen broadening increases due to incomplete interference of the diffracted X-rays, as the crystallite size becomes smaller. The inherent specimen broadening of a perfect crystal with larger crystallite size and without any defect broadening is called as Darwin width. The Darwin width can be approximated with a delta function and usually it is represented by a Lorentzian profile shape function [**19**]. In general no sample is perfect and most of the crystalline defects are introduced during formation or growth or by additional treatments. There are different types of lattice defects (Table 1.1), which are classified into point, linear and planar defects. When the defect density is low, these defects can be imaged by using transmission electron microscope (TEM). If the defect density is higher or crystallite size is very small, then the direct imaging by TEM is complicated and defects cannot be resolved. In such cases, the diffraction pattern is used to study the defect structure. These lattice defects will act as sources of strain in the matrix and scattering due to these defects decay asymptotically resulting in diffraction peak broadening [**20**]. The strain in the matrix will also shift the diffraction peak from the un-strained peak position resulting in a change in the lattice parameter. However, the microstrain will not shift the peak and will only broaden the peaks.

Table 1.1 Types of lattice defects

Point defects	Vacancies Substitutional atoms Interstitial atoms
Linear defects	Dislocations
Planar defects	Stacking faults Anti-phase boundaries
Volume imperfections	Voids and precipitates

Ungar [**21**] has defined the lattice defects into three groups based on the following argument: 1) The point defects such as vacancies or interstitial or substitutional defects observed in solid solutions, will distort the strain field locally. The clusters of point defects forming void or precipitate of different phases are treated as volume defects. The volume defects causing misfits between coherent precipitates and the matrix also act as a source of strain. 2) The linear defects/ dislocations influence the strain field to decay as $1/r$ (r-distance from the defect) causing the peak to broaden in an anisotropic way. 3) The planar defects will influence the XRD pattern differently as compared to the point and linear defects. The strain fields due to planar defects are homogeneous and space independent causing the peaks to shift. The planar defects such as stacking fault present in a crystal will influence only a particular set of planes resulting in the shift of peak position of that particular peak, while the other peaks have no effect due to stacking fault. The stacking faults are generally seen in heavily deformed materials. Ungar [**21**] has summarized that the lattice defects are the cause of different peak profile features observed in X-ray and neutron diffraction patterns.

1.3.4 Analytical XRD profile fitting methods

The profile fitting will help in extracting the line profile parameters viz., peak position, maximum intensity, peak shape, full width half maxima (FWHM), integral breadth and some other shape parameters. The two most common profile shape functions used in profile fitting are Gaussian or Lorentzian functions [**22**]. During 1980s, the different analytical line profile functions i.e., pseudo-Voigt [**23**], Pearson VII [**24**] and split Pearson VII [**25**] functions are developed and have been demonstrated to get best X-ray line profile fitting [**2**,**26**]. Using these fitting functions for all XRD profile reflections and representing the background with a suitable polynomial function, the line profile parameters can be refined. This approach is called whole profile pattern fitting (WPPF) or pattern decomposition (PD). The least square refinement of diffraction profile was first carried out by Rietveld [**1**]. Young and Wiles have improvised the Reitveld method by considering different profile shape functions in Rietveld refinement model [**2**]. By using Rietveld refinement method, the physical parameters such as lattice parameter, crystal structure, crystalline defects and crystallite size can be extracted from the profile parameters. The applicability of this approach i.e., by least square fitting the whole profile which has overlapping reflections will minimize the truncation errors as compared with the fitting of each individual peak profiles. Langford et al. [**27**] have carried out whole pattern fitting for nanocrystalline distortion-free materials.

In whole powder pattern modeling (WPPM), the entire diffraction pattern is modeled directly in terms of physical parameters by describing the microstructural features. The instrumental effects and background are accounted during whole powder pattern modeling. In this model the structure refinement is achieved by comparing the calculated XRD pattern with the experimental XRD pattern. However the challenge in this model is to obtain the realistic quantities from the sample microstructure. Based on the difficulties, relatively simple cases of high symmetric materials are easily modeled in this approach. Scardi and Leoni proposed WPPM and applied the same on ball milled Ni powder [**28**]. The Multiple Whole Profile (MWP) fitting method based on Fourier transforms of the measured profiles for all reflections were incorporated in the Convoluted Multiple Whole Profile (CMWP) software package [**29**,**30**]. The CMWP approach was implemented for the determination of crystallite size-distribution and dislocation structure of Al-Mg alloys. The multi peak fitting carried out by Kuzel [**31**], used Wilkens model of approximation for dislocation structures to describe the dislocation induced diffraction profiles.

1.3.5 Studies of different XRD line profile analytical methods to separate the profile broadening effects

For separating the effects of crystalline size and strain contribution in specimen broadening, various methods have been developed by many authors. In 1953, Williamson Hall (WH) method was developed, for separating size and strain contributions to line breadths that was based on their order dependence [**32**]. Warren and Averbach [**33**] proposed a method which is based on the formalism of Stokes and Wilson [**20**] for separating the contributions of crystallite size and strain from the Fourier coefficients of Bragg reflections. Enzo et al. [**34**] used pseudo-Voigt function to describe the intrinsic diffraction line profiles and its Fourier transform are analysed based on Warren-Averbach (WA) method. In 1993, Balzar &

Ledbetter [**35**] proposed double Voigt method for deconvoluting the effects of Fourier size and strain coefficients by considering both size and strain broadened profiles as Voigt functions. In this approach, the analytical form of Voigt function is considered to determine the size-strain Fourier coefficients analytically. However, anisotropic strain broadening is common due to dislocations and in such cases the Williamson-Hall or Warren-Averbach methods can be used only for isotropically broadened peaks of different orders. Ungar & Borbely [**36**] proposed modified Williamson-Hall method and a modified Warren-Averbach method to interpret the anisotropic strain broadening by the concept of dislocation contrast factors.

Another approach for quick, simple and elegant analysis is single peak profile analysis (SPPA) [**37**]. Rigorous analyses of single peak line profile in terms of Fourier coefficients are able to interpret the microstructural properties i.e., the initial slope of Fourier coefficient is proportional to the reciprocal of mean thickness of the crystal and its initial curvature sets a lower limit to the mean square strain [**38**]. The analysis of Fourier coefficients of single line profiles is mainly based on the theory of Warren-Averbach method. Another single peak method is based on the restricted moments or variance of a diffraction peak known as variance method. This method was first suggested by Tournarie [**39**] and then developed by Wilson [**40**]. The analyses in terms of breadth parameters is to fit the single Bragg reflection with Voigt function and to assume that the shape of the line profile due to size and strain broadening is mixture of both Cauchy and Gaussian components respectively [**41**].

Various authors carried out comparison studies on different size-strain analytical methods and proposed different methodologies for faster and better results [**42**,**43**,**44**]. Keijser et al. [**37**] reviewed on different materials using SPPA method which gave justified results as of multi peak profile analysis. A simple method of single peak Fourier analysis was proposed by Nandi et al. [**42**] which adopts exponential approximation for size coefficients at smaller column length (L) values. This study is carried out using different approaches of SPPA viz., Mignot-Rondot , Zocchi and initial slope methods and compared with the two peak analysis method on a series of platinum catalyst particles supported on silica gel. The analysis based on initial slope method gave more reliable microstrain values. Marinkovic et al. [**43**] used fundamental parameters approach [**45**] of profile fitting for carrying out Warren-Averbach (WA) method on bohmit powder and compared the results with Balzar method [**35**] and Enzo method [**34**]. The results of volume weighted average crystallite size determined using WA method was under estimated as compared with Balzar and Enzo method. Ghosh et al. [**44**] studied the titanium base aluminium alloys using X-ray diffraction. The average size, r.m.s strain, effective domain size, faulting probabilities and dislocation density obtained from WA method profile analysis were compared with that obtained from Rietveld method. The observed deviation was attributed to the assumption of Gaussian nature of size and strain diffraction profiles in WA method.

1.4 Strengthening of materials by fine particles

The second phase particles which are dispersed in supersaturated solid-solution results in localized internal stresses. The strengthening due to secondary phase particles is usually additive to the solid-solution strengthening [**46**]. In precipitation strengthened steels, the secondary phases with fine particle size are formed on ageing at lower temperatures, which are common sources of strengthening. The strengthening mechanism mainly depends up on the shape, size, volume fraction and inter-particle spacing of precipitate particles. The newly formed fine precipitate particles can be coherent or in-coherent with the lattice of the alloy matrix. The precipitate gets nucleated on ageing resulting in microstructural changes.

The strain field in the matrix caused by coherent precipitates increases the hardness at earlier stage of ageing which is known as precipitation hardening or age hardening. However, on further ageing the precipitates get coarsened and the coherency with matrix is lost resulting in reduction of strain and hardness.

On the other hand, the fine precipitate particles which are in-coherent and uniformly distributed in the matrix will cause dispersion strengthening. Theoretically, there are many other ways to introduce dispersion strengthening in the matrix by adding insoluble metallic particles (Eg. Oxide dispersion strengthened (ODS) alloys). The advantage of dispersion strengthening is that the solubility of in-coherent secondary phases in the matrix is very less even at elevated temperatures resulting in thermal stability at very high temperatures. The secondary phases which are formed in solid solution especially carbides and nitrides have less solubility even at higher temperatures which also results in thermal stability (Eg. 304HCu steel).

1.4.1 Studies on age hardening behaviour alloys

There are various grades of precipitation hardening (PH) stainless steels (17-4 PH, 15-5 PH and PH 13-8 Mo) and maraging steels (M250, C250 and T250) which show strengthening behaviour due to the presence of intermetallic precipitates. The 17-4 PH stainless steel (SS) is a precipitation hardening steel with 17Cr-4Ni and 3-4% copper added martensitic steel. In general, the solubility of copper particles in 17-4 PH steel is less even at lower ageing temperature (~380 °C) [**47**]. During initial ageing at lower temperatures, the precipitation of fine copper particles causes strain in the matrix. Mirzadeh and Najafizadeh [**48**] have studied the effect of ageing temperature and time on precipitation hardening behaviour of 17-4 PH stainless steel. Mahadevan et al. [**47**] applied XRD technique for studying the changes in microstrain and characterized the precipitation behaviour in 17-4 PH steel. Mahadevan in his thesis demonstrated that the strengthening in 17-4 PH SS is due to coherency strengthening arising from Cu precipitates and the modulus strengthening arising due to the difference in shear modulus of the precipitates and that of the matrix [**49**].

The M250 grade maraging steel shows strengthening behaviour due to the presence of hexagonal $Ni_3(Ti,Mo)$ and Fe_2Mo intermetallic precipitates. Vasudevan et al. [**50**] reported that the initial hardening in two different (C-250, T-250) maraging steels is due to hexagonal closed pack (*hcp*) structure of Ni_3Ti precipitates which favors good lattice fit (coherent) with the bcc martensite structure. However, the retention of high strength at longer ageing time was attributed to the presence of fine Fe_2Mo precipitates. The effect of precipitation in precipitation hardenable steels and maraging steels have been demonstrated by using different techniques viz., magnetic Barkhausen noise [**51**], ultrasonic velocity [**52**], X-ray diffraction [**16**,**53**], differential scanning calorimetry [**54**], hardness [**55**], and resistivity [**56**] measurements.

1.4.2 Studies on dispersive strengthening alloys

The precipitation hardening alloys (Iron, aluminium, nickel and titanium based alloys) employ secondary phase particles such as nitrides, carbides, oxides and carbonitrides to achieve dispersion strengthening [**46**]. Oxide-dispersive strengthened (ODS) ferritic steels are synthesized by adding the yttria (Y_2O_3) dispersoids for nuclear applications due to their excellent creep strength and swelling resistance [**57**]. Indeed the ODS material is designed for the application of fuel cladding tubes in fast neutron reactors, where internal stresses developed during service exposed conditions will influence the microstructure of ODS steels. Sallez et al. [**58**] have determined the crystallite size and dislocation density by using

XRD measurements and attributed the changes to microstructural evaluation of ODS steel by recovery and recrystallization.

304HCu is a Cu modified AISI type 18Cr-8Ni austenitic stainless steel (grade 304) developed for high temperature operational applications of boiler tubes in advanced ultra super critical (AUSC) thermal power plants. The copper (~3 wt%) which is present in this steel improves its creep strength and corrosion & oxidation resistance for operating in a high temperature and high pressure environment conditions of around 600 °C and 30 MPa respectively [**59**]. In this steel, the nano-size Cu-rich phase grows very slowly and the size is about 30-40 nm till 10,000 h ageing at 650 ℃, which results in precipitation strengthening [**60**]. The experimental and modelling investigations showed that precipitation of $M_{23}C_6$ and MX carbides increases with ageing duration [**61**]. It is reported that, Cr-rich $M_{23}C_6$ and Nb-rich M(C,N) precipitates are formed at grain boundaries and in the grains respectively on ageing time for 5000 h [**60**]. The precipitation hardening behaviour observed at higher ageing durations is due to distribution strengthening developed from all fine precipitates such as dispersive Nb(C,N) and Cu-rich phases that are formed during ageing [**62**]. Also, these precipitates do not change in size with time (on ageing for longer durations) which confirms the microstructural and phase stability at high temperatures between 600 – 800 °C and on ageing for longer durations [**63**,**64**,**65**]. Many attempts have been made to quantify the precipitate fraction and characterize the microstructural changes in 304HCu steel using electrical resistivity, hardness, optical microscopy, XRD, SEM and TEM [**56**,**61**,**66**].

Chi et al. [**60**] have investigated the precipitation behaviour of 304HCu steel which is aged at temperature of 650 °C by means of three dimensional atom probe (3DAP), scanning electron microscope (SEM), transmission electron microscope (TEM) and hardness measurements. From 3DAP, the formation of Cluster of Cu-rich particles at 1 h ageing duration in 304HCu steel is found and the variation in concentration of Cu element in the cluster along with other elements of Fe, Cr, Ni was brought out at different ageing durations. The TEM studies on samples aged for 10000 h at 650 °C revealed an average size of 35 nm Cu particles. The micro-hardness measurements show an increase with ageing time and keeps steady value at 8000 h of ageing.

1.5 Ageing behaviour studies using XRDLPA

XRD studies of microstructural features i.e., lattice parameter, phase quantification, crystallite size, microstrain, and dislocation density were adopted by various authors to characterize the ageing behaviour of different metals, alloys and compounds. Lahrman et al. [**67**] measured lattice mismatch to correlate with the precipitation strengthening in γ'-precipitate-hardened nickel-base superalloy using X-ray diffraction (XRD), electron diffraction and by considering interface dislocation analysis. Ungar et al. [**68**] have made an attempt to correlate the internal stress with broadening of the X-ray line profiles. The dislocation structure and long range internal stress developed in ultrafine copper crystals during deformation by equal-channel angular pressing was investigated by using X-ray diffraction line profile analysis [**36**]. The synchrotron based XRD strain broadening analysis were carried out on copper foils to get better resolution peaks as well as less absorption losses. The study provides the information of the change in lattice parameter and dislocation density with applied load by considering the contrast factor caused by dislocations in the broadening [**69**]. Mahadevan et al. [**53**] correlated the microstrain (α) determined from modified WH approach with hardness and used it for characterizing the precipitation hardening behaviour of M250 grade maraging steel. Assuming that the observed increase in microstrain (α) with ageing time at temperature of 755 K (482 °C) is due to precipitation, the Avrami exponent (n) in the kinetics of precipitation was determined. Similar approach of XRD line profile analysis was carried out on 17-4 PH steel during precipitation ageing and the microstrain (α) is correlated with hardness [**47**]. Further, the evolution of dislocation density determined based on modified Williamson Hall method was used for characterizing the tensile deformation behaviour of advanced ODS steels [**70**]. The modified Warren Averbach method was implemented to the XRD peak profiles of high temperature creep samples of EK-181 steel to study the evolution of dislocation density due to the influence of nitrogen concentration [**71**].

1.6 Studies on hardness and electrical conductivity measurements

The hardness is the measure of strength of a material which depends upon the different microstructural features such as grain size [**72**,**73**], dislocation density [**74**], fine dispersive particles [**75**] and modulus [**76**] of the lattice. The hardness has been used to correlate the microstructural changes due to thermal ageing in different materials by Vasudevan et al. [**77**] Rajkumar et al. [**78**], Mahadevan et al. [**47**] and Huang et al. [**65**]. The variation observed in electrical resistivity and hardness are able to demonstrate the precipitation kinetics by using Johnson–Mehl–Avrami (JMA) in 17-4 PH steel [**56**,**48**].

Various studies showed that the age hardening behaviour could be characterized with the help of electrical resistivity/conductivity measurements. Lendvai et al. [**79**] correlated the changes observed in resistivity with the precipitation of G.P Zones that takes place during isothermal ageing of Al-Zn-Mg alloy. The volume fraction of Guinier-Preston (G.P) Zone precipitates which are formed during isothermal ageing of Al-Zn-Mg alloy, are determined using X-ray small angle scattering (XSAS). Viswanathan et al. [**56**] carried out the resistivity measurements to study the kinetics of precipitation in 17-4 PH steel. The electrical conductivity measurements were able to characterize cold working, thermal ageing and phase transformation. Manojkumar et al. [**80**] carried out the conductivity measurements for characterising the cold working as well as thermal ageing behaviour in 316 stainless steel. The phase transformation of β Ti-alloy (body centred cubic) to α Ti-alloy (hexagonal closed pack structure) on ageing is analysed from the conductivity measurements.

1.7 Motivation and objectives

A brief introduction on the applications of XRD line profile analysis, electrical conductivity and hardness measurements for characterizing microstructural changes have been presented. Earlier studies on precipitation behaviour in 304HCu steel were carried out by imaging the microstructure at different ageing durations and temperature between 600-800 °C.

The 304HCu steel which finds application in boiler tubes are formed by various hot forming processes such as forging, extrusion and rolling. Formation of U-bend in these boiler tubes is equivalent to that of cold working and their use at higher temperatures causes ageing induced changes. The cold deformation induced dislocations play a critical role during high temperature ageing, by influencing the precipitation kinetics. Dutta et al. [**81**] have proposed a model to describe the precipitation kinetics during isothermal ageing following deformation of Nb-containing microalloyed steels. Hong et al. [**82**] reported that the presence of strain-induced defects in the matrix results in early formation of precipitates mainly along the deformation bands in 347 austenitic stainless steel.

The scope of the present dissertation is to fulfill the gaps and satisfy the need for studying deformation induced precipitation behaviour of 304HCu steel at different cold working conditions by XRDLPA, which provides hunch into the microstructural evolution. The complimentary methods of hardness and electrical conductivity measurements were used to provide the information of deformation induced precipitation in 304HCu steel.

The simultaneous evolution in microstructure by annihilation of dislocations and growth of precipitates during ageing in steels consisting of dislocations in the matrix due to either solution annealed or prior deformation will change the microstrain.

- ➢ *To understand the changes observed in microstrain during thermal ageing and relate the cause of strain broadening to the microstructural changes such as dislocation density and precipitation kinetics it is essential to carry out XRDLPA.*
- ➢ *To meet this objective, the microstrain determined from different XRD line profile analyses (XRDLPA) like conventional mWH method, Fourier WA method and multi-dimensional distribution of lattice metrics based WPPF tool which is available in the open domain are reviewed.*

In order to study precipitation occurring at elevated temperature of 650 °C in cold worked 304HCu steel and to study the influence of cold working on precipitate kinetics in 304HCu steel, the hardness and electrical conductivity measurements are analysed. All solute atoms which cluster in the form of precipitates during ageing are difficult to estimate using conventional quantitative analysis.

- ➢ *Hence, the fraction of precipitates formed during ageing can be correlated by estimating the change in hardness and electrical conductivity. The reaction rate and Avrami exponent can be determined to understand the kinetics of precipitation in* *cold worked (strain induced dislocations) and isothermally aged 304HCu steel (precipitation and dislocation annihilation).*

- *The change in precipitation kinetics due to prior cold work needs to be correlated, with an equivalent change in apparent activation energy as well as an equivalent change in isothermal temperature.*

The different types of precipitates such as Cr-rich $M_{23}C_6$, Nb-rich M(C,N) and Cu-rich phases are formed during ageing. The dislocations created in cold worked 304HCu steel get annihilated during initial ageing. The new vacancies created due to dislocations will accelerate the precipitation. The precipitation of copper which contributes coherency strength will increase microstrain.

- *Synchrotron X-ray diffraction provides better resolution peak which would help to identify the fine precipitate phases formed in the material and to account the increase in precipitation with changes in lattice parameter obtained from the shift in matrix peak positions.*
- *To ascertain the ageing behaviour of 304HCu steel by XRD profile analysis, it would be worthwhile to derive normalized mean square strain and crystallite size from XRDLPA and to correlate with the microstructural evolution that takes place during ageing.*
- *To explore the changes observed in microstrain after ageing of the SA and cold worked specimens of 304HCu steel and bring out correlation with hardness.*
- *Finally, to validate the approach of separating the simultaneous changes in microstructure due to dislocation annihilation and precipitation, the column length*

dependent microstrain obtained from Fourier analysis is correlated with dislocation density.

Chapter 2

2 Theoretical considerations

According to Bragg's law, it is known that when X-rays interact with a polycrystalline material, the X-rays get diffracted in certain angles. The study of diffracted peaks and their shapes using various analytical methods will help in characterizing the microstructure of the crystalline material. In this chapter, the mathematical formalisms of XRD peak shape, peak broadening, profile functions and the theoretical aspects of different approaches for separating the size and strain contributions to peak broadening are reviewed. The strain anisotropy and its logarithmic distribution in Fourier transform of XRD peak profiles are also discussed in the present chapter.

2.1 Shape of the XRD peaks

The spectrum of X-ray peaks at different diffraction angles represents the position of lattice points in the crystalline material in reciprocal space. The XRD peaks are not sharp and some broadening is observed. The peak positions and intensities of Bragg reflections having certain peak width can be determined by fitting to suitable peak shape functions. The simplest and most commonly used profile shape functions (PSFs) for profile fitting are Gaussian ($I_G(x)$) and Lorentzian ($I_L(x)$) shape functions which are given by

$$\mathrm{I_G}(x) = \mathrm{e}^{-(\ln 2)\left(\frac{2x}{W_G}\right)^2} \qquad \cdots \qquad (2.1)$$

$$\mathrm{I_L}(x) = \frac{1}{1 + (2x/W_L)^2} \qquad \cdots \qquad (2.2)$$

where $x = (2\theta - T_p)$,

2θ = angle of diffracted beam

T_p= angle of Bragg's peak position

W_G = FWHM of the Gaussian profile,

W_L = FWHM of the Lorentzian profile.

Khattak and Cox (1977) have shown the use of simple Gaussian or Cuachy-Lorentz functions in their X- ray diffraction line profiles [**22**]. Usually, the real peak shape functions lie between the Lorentz and Gauss functions. The earlier works of profile analysis carried out by Suortti et al. [**83**] and Adams & Hewat [**84**] have demonstrated that in the case of angular dispersive patterns, the simple Gaussian or Lorentzian functions are less satisfactory. In order to improve the fitting, a variety of profile shape functions (PSF) have been attempted for fitting XRD peak profiles with different combinations of Gaussian and Lorentzian functions viz., Voigt function [**25**], the pseudo-Voigt function [**2**] and the Pearson VII function [**85**]. The Voigt function (*V*) is given by a convolution of Lorentzian and Gaussian function. The Voigt-function can be calculated numerically using the complex error function. The shape of Pearson VII (*PVII*) function varies from purely Lorentzian to Gaussian function based on the shape factor (*m*, which varies from 1 to ∞). The pseudo-Voigt (*pV*) is given by the fractional summation of Lorentzian and Guassian based on a mixing parameter (η). Considering Eqn. (2.1) & Eqn. (2.2), the mathematical formulism for Voigt (*V*), Pearson VII (*PVII*) and pseudo-Voigt (*pV*) profile shape functions are as follows:

$$V(x) = I_G(x) \otimes I_L(x) = \mathrm{I}_0 \int_{-\infty}^{+\infty} I_G(x')I_L(x - x')\, dx' \quad \cdots \quad (2.3)$$

$$\mathrm{PVII}(x) = \mathrm{I}_0 \frac{1}{(1 + x^2/ma^2)} \quad \cdots \quad (2.4)$$

$$pV(x) = \mathrm{I}_0[\eta I_L(x) + (1 - \eta)I_G(x)] \quad \cdots \quad (2.5)$$

where $x = (2\theta - T_p)$,

$a = \left(2^{\frac{1}{m}} - 1\right)/(W/2)^2$,

m = shape factor

x' - integral parameter

η = Cauchy content of the pV function

(1-η) = Gaussian content of the pV function

W = FWHM of the profile

I_0 = Intensity at peak maximum.

The left-right asymmetry observed in the X-ray diffraction profiles can be incorporated in these PSFs with left and right side of the peaks of different (FWHM) widths. The basic demands of PSFs are that they should be mathematically simple, computationally possible, best least square fit and moreover should be a combinational function of Lorentzian and Gaussian. There were several more PSFs which were compared by Young and Wiles [**2**] for the application of whole pattern profile fitting and concluded that pseudo-Voigt and Pearson type VII function show most promising results. Howard & Snyder [**85**] evaluated a wide variety of shape functions and concluded that the split- Pearson VII function combined with either a Gauss- Newton or a Marquardt optimization algorithm gives excellent fit to diffraction lines. David and Matthemam [**86**] incorporated Voigt function in refinement program and assessed the diffraction line profiles. Prabal Dasgupta [**87**] has reviewed the use of pseudo-Voigt functions for X-ray diffraction profiles and concluded that the Cauchy content must be greater than 0.328 for a meaningful accurate results in terms of data on crystallite size.

2.2 Convolution of peak functions

In an ideal crystalline material, the distribution of atoms within a lattice is repeated in a unique way throughout the crystallite causeing the XRD line to broaden by a finite width known as Darwin width [**88**]. In real crystalline materials the presence of lattice imperfections and the limitation of crystallite dimension which determines the microstructure and geometrical aberrations in real experimental conditions will affect the shape and broadening of XRD peaks. From the above consideration, the observed XRD line profile is said to be convolution of two independent shape functions 1) specimen shape function, $g(2\theta)$ and 2) instrumental shape function, $f(2\theta)$. The process of convolution is one in which the product of two functions is integrated over all space. It can be written as

$$h(2\theta) = g(2\theta) \otimes f(2\theta) = \int_{-\infty}^{+\infty} g(x') f(2\theta - x')\, dx' \qquad \cdots \qquad (2.6)$$

where $h(2\theta)$ represents observed peak shape function. The $g(2\theta)$ arises due to microstructural properties of the specimens under investigation and $f(2\theta)$ arises due to imperfect experimental conditions such as spectral distrubution, beam divergence, receiving slit, sample transparency, flat sample, sample displacement error and other factors. The observed XRD peak is a convolution of all these sources in addition to the background.

The instrumental broadening can be determined using a defect free sample because the observed XRD line broadening from defect free sample is completely due to instrumental effects. Once instrumental shape broadening is separated from the experimental line broadening, the material properties can be determined from the sample shape broadening. The instrumental broadening ($f(2\theta)$) i.e., the observed full width at half maximum (FWHM) which is a function of diffraction angle (θ) is given by Caglioti formula [**89**]:

$$f(2\theta) = (U tan^2\theta + V tan\theta + W)^{1/2} \qquad \cdots \qquad (2.7)$$

where U, V and W are the instrumental parameters. The Eqn. (2.7) is valid if the peak shape functions are Gaussian, pseudo-Voigt and Pearson VII functions. Futher, the mixing function (η) is also a function of 2θ. For Lorentzian shape function, the instrumental broadening (*f'(2θ)*) is given by [**89**]

$$f'(2\theta) = \frac{U}{cos\theta} + Vtan\theta \qquad \cdots \qquad (2.8)$$

For any particular source and instrumental setup, the U, V, W parameters are unique. With the availability of exceptionally precise and high resolution neutron or synchrotron powder diffractometer, the instrumental profile becomes sufficiently narrow and the total broadening is significantly due to microstructural defects in specimen such as crystallite size, mean square strain and faults. Further, the intensity due to the specimen (g) is convolution of functions due to size, microstrain and faulting which is given by

$$g = g_{size} \otimes g_{strain} \otimes g_{fault} \qquad \cdots \qquad (2.9)$$

The process of extracting the microstructural features (size, strain and fault) is known as XRD line profile analysis (XRDLPA). The deconvolution of these shape functions (*f(2θ) & g(2θ)*) can be solved analytically based on the multiplicative property of the Fourier transforms and the sample coefficient can be obtained from the following equation:

$$G(t) = \frac{H(t)}{F(t)} \qquad \cdots \qquad (2.10)$$

where *H(t)*, *F(t)* and *G(t)* are the Fourier transforms of *h(2θ), f(2θ) & g(2θ).* From Eqn. (2.10), the cosine and sine Fourier coefficients of *g(2θ)* are obtained. These Fourier coefficients are further used to interpret the lattice defects which constitute the microstructure of the specimen.

The whole profile pattern fitting which is established by Young and Wiles [**2**] have incorporated instrumental effects in to the profile shape functions with a model of angle dependent Caglioti expression (Eqn. (2.7) & (2.8)). This is based on the principle that the angle dependent Caglioti expression is considered as FWHM in the commonly used profile shape functions of Pearson type VII, Voigt, and pseudo-Voigt functions.

2.3 XRD profile specimen broadening parameters

The most significant physical sample parameters which will broaden the profile shape function of specimen contribution ($g(2\theta)$) are crystallite size and strain. It would be worth to study the effect of broadening due to average crystallite size and microstrain which is of immense interest in material characterisation.

2.3.1 Size Broadening

The first step towards the determination of crystallite size from XRD line profile broadening was made by Scherrer in 1918 [**90**]. Scherrer worked on structure analysis of colloidal particles (silver & gold) and the cause of broadening was attributed to coherently scattering crystallites. Scherrer derived a relation between crystallite size and peak broadening by assuming certain ideal conditions, such as an incident beam composed of perfectly parallel and strictly monochromatic radiation on a monodisperse powder. If the crystal is sufficiently large enough, there exist a set of planes from the surface to the deep in the crystal which cause destructive interference in all directions other than at Bragg's angle. But for small crystals, the complete cancellation does not occur and hence a significant peak width due to finite crystallite size is observed.. This peak width increases with decrease in crystallite size. From the condition of destructive interference a relation between crystallite size and peak broadening was derived which came to be known as Scherrer equation:

$$D = \frac{k\lambda}{\beta_s cos\theta} \qquad \cdots \qquad (2.11)$$

where D is crystallite size, λ is the wavelength, θ is the half of diffraction angle, β_S is peak breadth and k is Scherrer constant frequently referred to as crystallite-shape factor [**91**]. In Eqn. (2.11), the crystallite size can be defined in different ways as perpendicular length to the diffraction planes or square root of crystallite surface area or cube root of the crystallite volume. The width β_S can be considered from full width at half maximum or integral line width of the Bragg's peak, still the definition of Scherrer equation remains the same. But the dependency of Scherrer constant (k) in addition to crystallite shape, will depend up on the definitions of the average crystallite size and the peak breadth. Langford and Wilson [**92**] have made an excellent discussion about the shape factor (k) values. The shape factor (k) can be between 0.62 - 2.08. In a polycrystalline material there are many crystallites with different size which can be characterized by size distribution function. The most commonly used size distribution function is lognormal distribution especially for TEM observations [**93**]. The size distribution obtained from diffraction analysis and TEM investigations are almost same in strain-free nano-sized powder particles [**94**,**95**]. Langford et al. [**27**] have discussed the size distribution obtained from XRD profiles and TEM observations. The effect of size distribution on the shape of the XRD profile is likely to lengthen its tail. In crude approximation, the profile shape function of crystallite size is considered to be Lorentzian function. Ideally, the shape of crystallite size function lies between a Gaussian and a Lorentzian function and tends to somewhat more Lorentzian with increase in the size of dispersion. The profile shape broadening contributed by the specimen was attributed to only crystallite size till 1930s. It should be noted that, Eqn. (2.11) is valid if there is negligible strain broadening.

2.3.2 Strain broadening

In 1944, Stokes and Wilson [**20**] attributed the broadening in XRD line profile of cold worked materials to the apparent strain, resulted from different approximations such as 1) breaking of crystals in to small crystallites, 2) presence of crystal grains of different lattice parameters and 3) distortion of large crystal grains. When a polycrystalline material is subjected to deformation and the deformation of crystal is extended to larger distances then the strain is said to be macrostrain or uniform strain. If the distortion of the crystal is non uniform and varies from one grain to another then the strain is called localized strain or microstrain. The effects of uniform and non uniform strain are observed in XRD line profile by shifting the peak position and by increasing the peak width respectively. The strain is defined as the fractional deviation from the original dimension ($\Delta d/d$). By differentiating the Bragg's law, we obtain a relation between broadening (β) and the total strain (ε) as follows [**14**,**20**]

$$\beta_D = \Delta 2\theta = -\frac{2\Delta d}{d}\, tan\theta = -2\varepsilon tan\theta \quad \cdots \qquad (2.12)$$

2.3.3 The distribution of strain field

The distribution of non uniform strain can be approximated in many ways based on the lattice defects and their distortion field. Stokes and Wilson [**20**] have assumed that the non uniform strain is equally and likely distributed from zero to maximum of compressive and tensile strain. For estimating the maximum compressive or tensile strain ε_{max}, the total strain (ε) from Eqn. (2.12) was divided by two and we get

$$\varepsilon_{max} = \frac{\beta_D}{4tan\theta} \quad \cdots \quad (2.13)$$

When the strain field is distributed in Gaussian form, then the corresponding root mean square strain (ε_{rms}) is given by

$$\varepsilon_{rms} = \frac{\beta_D}{2\sqrt{2\pi}tan\theta} \quad \cdots \quad (2.14)$$

Krivoglaz and Ryaboshapka [**96**] described the strain in terms of a random distribution of dislocations in a finite crystal. For this model, the Fourier transformation of line profile were calculated. Krivoglaz derived the mean square strain $\langle\varepsilon^2\rangle$ (which can be determined using Warren-Averbach method) with a function of crystal size (D) and Fourier column length (L) as given below:

$$\langle\varepsilon^2\rangle = \frac{\rho\bar{C}b^2}{4\pi}\ln\left(\frac{D}{L}\right) \quad \cdots \quad (2.15)$$

where ρ is the dislocation density, $\bar{C}$ is the dislocation contrast factor (see § 2.5) and b is the Burgers vector of the dislocations. In Krivoglaz model the strain $\langle\varepsilon^2\rangle$ diverges when the crystal size increases. Wilkens solved this problem by introducing the concept of restrictedly random dislocation distributions in a cylindrical body [**97**]. In this model Wilkens function ($f(\eta)$) [where η is function of (R_e /L) amd R_e is outer cut off radius of dislocations] was introduced instead of crystal size D and the expression for mean square strain is expressed as

$$\langle\varepsilon^2\rangle = \frac{\rho\bar{C}b^2}{4\pi}f\left(\frac{L}{R_e}\right) \quad \cdots \quad (2.16)$$

The full expression for Wilkens function $f(\eta)$ is given in [**98**] and the function is approximated as logarithmic at smaller values of η which has the following explicit form [**99**] :

$$f_1(\eta) = \frac{7}{4} - log2 - \log(\eta) \qquad \cdots \qquad (2.17)$$

The Wilkens model was derived on the assumption that the strain filed is restricted to a cylinder of radius R_e. Gaál [**100**] developed a model for a far more general distribution of dislocations, in which a configuration of polarized dislocation dipoles leads to asymmetric strain broadening.

Balzar and Ledbetter [**35**] assumed that both size and strain broadening follow Voigt functions and their convolution is again Voigt function which is known as double-Voigt method. He considered the Fourier coefficients of line broadening by a Voigt function:

$$A(L) = \exp[-2L\beta_C - \pi L^2 \beta_G^2] \qquad \cdots \qquad (2.18)$$

where β_C is Cauchy width and β_G is Gaussian width. By comparing the Voigt function of strain Fourier coefficient with the strain coefficient from the approach of assumed Gaussian exponent [**101**], the mean square strain is derived as follows:

$$-2\pi^2 L^2 K^2 \langle \varepsilon^2(\mathrm{L}) \rangle = -\,[2L\beta_{DC} + \pi L^2 \beta_{DG}^2]$$

$$\langle \varepsilon^2(\mathrm{L}) \rangle = \left(\frac{1}{K^2}\right) \left[\frac{\beta_{DC}}{\pi^2 L} + \frac{\beta_{DG}^2}{2\pi}\right] \qquad \cdots \qquad (2.19)$$

where β_{DG} & β_{DC} are Gaussian and Cauchy components of broadening due to distortion.

2.4 XRDLPA for separating size and strain effects

There are different XRD line profile analytical methods which can be used for separating the specimen broadening due to the effects of crystallite size and strain.

2.4.1 *Williamson Hall method*

In Williamson Hall method [**102**], the line breadths of Bragg reflections were attributed to simultaneous small particle size and strain broadening. The variation of total broadening with diffraction angle indicates the predominating behaviour of strain broadening particularly at higher Bragg angles. The Willaimson Hall method assumes both the size and strain breadths as Cauchy such that the total broadening β is summation of size and strain broadening as

$$\beta = \beta_S + \beta_D$$

by substituting the broadening due to size and strain obtained from Eqn. (2.11) & (2.13), the total broadening is linear with tanθ function and it is written as

$$\beta cos\theta = \frac{k\lambda}{D} + 4\varepsilon sin\theta \quad \cdots \quad (2.20)$$

$$\beta^* = \frac{k}{D} + 2\varepsilon K \quad \cdots \quad (2.21)$$

where $\beta^* = \beta \cos\theta / \lambda$ and $K = 2\sin\theta \, / \, \lambda$. By plotting β^* against diffraction vector K, the resultant linear least square fit will have an intercept which is inversely proportional to crystallite size (D) and slope of the plot which is proportional to microstrain (ε). The plot between broadening and diffraction vector is known as Willaimson Hall (WH) plot. In Williamson-Hall (WH) equation [Eqn. (2.21)], the Scherrer constant k takes 1 for integral breadth and if full width at half maximum is used when k takes 0.9. If diffraction peak breadths are more Gaussian, then the square of total broadening is summation of squares of size and strain breadths and the Williamson-Hall equation is:

$$(\beta^{*})^2 = \left(\frac{1}{D}\right)^2 + (2\varepsilon K)^2 \qquad \cdots \qquad (2.22)$$

Even though the diffraction profile shapes are mixture of both Cauchy and Gaussian, the appropriate Williamson-Hall equations are used to separate the size and strain components.

2.4.2 Warren-Averbach method

To separate the effects of crystallite size and microstrain on the diffraction line broadening, the Warren-Averbach method [**33**] uses Fourier based analysis. In this method, the cosine Fourier transformation of diffraction profile is shown as the product of size and distortion Fourier coefficients. The Fourier transformation of diffraction profile is given by

$$A(L,K) = A_S(L)\, A_D(L,K) \qquad \cdots \qquad (2.23)$$

Since $A_S(L)$ is the order-independent size Fourier coefficient and $A_D(L,K)$ is the order dependent strain Fourier coefficient or (distortion coefficient), the size and strain effects can be separated by taking logarithm on both sides in Eqn. (2.23)

$$A(L,K) = A_S(L)\, A_D(L,K) \qquad \cdots \qquad (2.23)$$

and we get

$$\ln(A(L,K)) = \ln(A_S(L)) + \ln(A_D(L,K)) \quad \cdots \qquad (2.24)$$

where L is the column length defined as the length in the direction of diffraction vector (K) which is an integer (n) multiple of Fourier unit length (a_3). The column length is given by $L = na_3$ and

$$a_3 = \frac{\lambda}{2(sin\theta_2 - sin\theta_1)} \qquad \cdots \qquad (2.25)$$

wherein $2\theta_1$ and $2\theta_2$ are angular range between which the Fourier transformation of diffraction profile is analysed. Halder and Wagner [**101**] have approximated the distortion Fourier coefficient with an Gaussian exponential function for smaller values of L as

$$A_D(L, K) = exp\left[-\frac{2\pi^2 L^2 \langle \varepsilon^2 \rangle}{d_{hkl}^2}\right] \qquad \cdots \qquad (2.26)$$

Using the exponential distortion expression in Eqn. (2.24), we get

$$\ln(A(L, K)) = \ln(A_S(L)) - 2\pi^2 L^2 K^2 \langle \varepsilon^2(L) \rangle \quad \cdots \qquad (2.27)$$

where $\langle \varepsilon^2(L) \rangle$ is the mean square of the strain component perpendicular to the reflecting planes averaged over the column length L and $K^2 = 1/d_{hkl}^2$(d_{hkl} is spacing between *hkl* planes). Using the Warren-Averbach expression [Eqn. (2.27)], the separation of size-strain is possible; if at least two orders of reflections are available. The Warren-Averbach (WA) plots of logarithm of Fourier coefficients with $1/d_{hkl}^2$ at different column lengths are linear plots which give column length dependent size coefficient $A_S(L)$ from the intercept and mean square strain $\langle \varepsilon^2(L) \rangle$ from the slope. The column length dependency of mean square strain $\langle \varepsilon^2(L) \rangle$ has been detailed in § 2.3.3. The surface weighted crystallite size (D_{eff}) can be determined from the slope of size coefficient plot at L→0 [**103**]:

$$\left[\frac{dA_s(L)}{dL}\right]_{L\to 0} = -\frac{1}{D_{eff}} \qquad \cdots \qquad (2.28)$$

2.5 Strain anisotropy and the contrast factors of dislocations

The presence of defects such as dislocations and faults in a crystalline material can produce anisotropic strain broadening. The anisotropy in strain means that the broadening of diffraction profiles due to strain does not increase monotonically as a function of diffraction order (K) or with *hkl* indices. The anisotropic behaviour of strain contribution to line broadening and Fourier coefficients depends upon order of the peak, orientation of dislocation line, Burgers vector, elastic constants, effective outer cutoff radius, diffraction vector and column length [**99**,**104**,**105**]. The theory of dislocations of XRD line broadening was described by orientation factor or contrast factor ($\bar{C}$) based on Eqn. (2.16). The individual contrast factors of dislocations characterize the relative orientation of dislocation lines, Burgers vector (b) and diffraction vector (K) i.e. for example, there exists no effect of line broadening due to dislocations if $b.K = 0$. In a polycrystalline material only the average contrast factor can be determined from the experimental observations. For the purpose of Rietveld structure refinement, a few phenomenological models were proposed based on the anisotropic elastic constants, by Rodriguez-Carvajal [**106**], Popa [**107**] and by Stephens [**108**]. Ungar and Borbely [**36**] accounted the strain anisotropy in the analysis of line breadths and Fourier coefficients by using average contrast factor of dislocations. It has been shown by Ungar and Tichy [**109**] that in the case of untextured cubic polycrystalline or randomly oriented dislocations system, the values of average contrast factors can be expressed by a linear function of fourth-order polynomials of *hkl* indices and the contrast factors are given by

$$\bar{C}_{hkl} = \bar{C}_{h00}(1 - qH^2) \quad \cdots \quad (2.29)$$

where $H^2 = (h^2k^2 + k^2l^2 + l^2h^2)/(h^2 + k^2 + l^2)^2$, $q = B/A$ with A and B as constants which depend on elastic constants of the material and $\bar{C}_{h00} = A$, is the average contrast factor corresponding to the indices *h00*. The expression for contrast factors [Eqn. (2.29)] given by Ungar and Tichy [**109**] is similar to the equation derived for random displacement of atoms in elastically anisotropic cubic crystals by Stokes & Wilson [**20**]. If the values of q and $\bar{C}_{h00}$ are known the average contrast factor can be determined. Ungar et al. [**110**] calculated and compiled the values of q and $\bar{C}_{h00}$ for the most common slip systems in the f.c.c and b.c.c systems using which the average contrast factors have been graphically parameterized.

2.5.1 Modified Williamson-Hall method and Warren-Averbach method

The presence of strain anisotropy due to dislocations and faults will lead to non linear size-strain plots of WH and WA methods. The modified Williamson-Hall and Warren-Averbach line profile methods proposed by Ungar and Borbely [**36**] have shown that by taking into account of contrast factor caused by dislocations in WH and WA methods will enable in determination of anisotropic strain caused by dislocations. The modified Williamson-Hall (mWH) expression for line broadening is given by

$$\beta^* = 1/D + \alpha\left(\mathrm{K}\bar{\mathrm{C}}^{1/2}\right) + O(\mathrm{K}^2\bar{\mathrm{C}}) \quad \cdots \quad (2.30)$$

where $\alpha = (\pi A^2 b^2/2)^{1/2}\rho^{1/2}$ is called the *hkl* independent or normalised root mean square strain and O indicates non-interpreted higher-order terms. The variable A is a constant depending on the effective outer cut-off radius of dislocations (R_e), b is the Burgers vector, ρ is the dislocation density and $\bar{C}$ is the average contrast factor of the dislocations.

In the case of dislocation containing materials, the total broadening at $K\bar{C}^{1/2} \rightarrow 0$ is analytical and even function of $K\bar{C}^{1/2}$. Thus the mWH plot starts with zero slope, based on the assumption, Ungar et al. [**111**] derived the following equation:

$$\beta^{*} = 1/D + \alpha'\left(K\bar{C}^{1/2}\right)^{2} + O(K^{2}\bar{C})^{2} \quad \cdots \qquad (2.31)$$

where O stands for higher order terms related to two particle correlation in dislocation ensemble. Ungar et al. [**109**] provided a procedure for experimental determination of average contrast factor $\bar{C}$ from q and $\bar{C}_{h00}$ factors using quadratic form of mWH plot:

$$(\beta^{*})^{2} = (1/D)^{2} + \alpha^{2}\left(K\bar{C}^{1/2}\right)^{2} + O(K^{2}\bar{C})^{2} \quad \cdots \qquad (2.32)$$

Subtituting Eqn. (2.29) into Eqn. (2.32), we get

$$[(\beta^{*})^{2} - (1/D)^{2}]/K^{2} \approx \alpha^{2}\bar{C}_{h00}(1 - qH^{2}) \quad \cdots \qquad (2.33)$$

The best fit of linear regression of the above equation by varying the value of D versus H^2 can provide q value from the slope and $\bar{C}_{h00}$ determined from elastic constants.

In modified Warren-Averbach method, the WA expression Eqn.(2.27) is modified with mean square strain (Eqn. (2.15)) proposed by Krivoglaz [**104**] which is based on dislocation model for small L and, we get

$$\ln(A(L)) = \ln(A_{S}(L)) - \rho B L^{2}\, ln\left(\frac{R_{e}}{L}\right) K^{2}\bar{C} + O(K^{2}\bar{C})^{2} \quad \cdots \qquad (2.34)$$

where $B = \pi b^2/2$ and the scaling factor here is $K^{2}\bar{C}$ instead of K^2.

2.5.2 Phenomenological model

In the phenomenological model proposed by Stephens [**108**], the anisotropic peak broadening of diffraction profiles is taken into account and the corresponding anisotropic strain is obtained as discussed below. The lattice spacing *d* between planes with miller indices *hkl* is given by

$$1/d^2 = M_{hkl} = Ah^2 + BK^2 + Cl^2 + Dkl + Ehl + Fhk$$

where A, B, C, D, E and F are metric parameters of the reciprocal lattice. Considering that the strain broadening causes a distribution of these metric parameters, the variance of M_{hkl} can be determined.

According to this model the anisotropic broadening (Γ) and its corresponding anisotropic strain (δ_{hkl}) for each *hkl* plane are

$$\Gamma(\mathrm{hkl}) = [S_{400} + (S_{220} - S_{400})H^2]^{\frac{1}{2}} tan\theta a_o^2 \quad \cdots \qquad (2.35)$$

$$\delta_{hkl} = \frac{\delta d}{d} = \frac{\pi[\sigma^2(M_{hkl})]^{\frac{1}{2}}}{(180M_{hkl})} \quad \cdots \qquad (2.36)$$

where, the variance of M_{hkl} is stated as

$$\sigma^2(M_{hkl}) = \sum_{HKL} S_{HKL}\, h^H k^K l^L \quad \cdots \qquad (2.37)$$

and S_{ABC} are the anisotropic strain parameters defined for H+K+L = 4. For cubic system $S_{400} = S_{040} = S_{004}$, $S_{220} = S_{202} = S_{022}$ and the values of other S_{HKL} are zero. From the two values of S_{400} and S_{220}, strain along each of the *hkl* directions can be estimated.

2.6 Rietveld method

The Rietveld method introduced by H. M. Rietveld [**1**] is a whole profile fitting method, in which all the diffraction peaks are fitted with analytical profile shape functions (PSF) by including the background. The most commonly used PSFs for profile fitting are discussed in § 2.1. The refinement of these PSFs can be simulated from the structure model or non-structural model. The simulated pattern is generally constructed from the physical properties of different kind of lattice defects to obtain a best fit over the maxima and tail region of the observed peak profile intensities. In non-structural model, the refinement is done until the best fit is obtained between the observed and calculated pattern without any structural constrain.

The best least square fit is achieved by obtaining a minimal residual value between experimentally observed and calculated patterns. To evaluate the quality of fitting, the weighted residual error (R_{wp}) is determined as follows

$$R_{wp} = \left[\frac{\sum w_i[I_{oi} - I_{Ci}]^2}{\sum w_i(I_{oi})^2}\right]^{1/2} \qquad \cdots \qquad (2.38)$$

where I_{oi} and I_{ci} are the experimentally observed and calculated intensities and the weights w_i are inversely proportional to the variance of each individual intensity value $(1/(I_{oi})^{0.5})$. The measure of goodness of fit (GoF) describes the discrepancy of observed values with calculated values by comparing the weighted residual error (R_{wp}) with the expected residual error (R_{exp}):

$$GoF = \frac{R_{wp}}{R_{exp}} \qquad \cdots \qquad (2.39)$$

The R_{exp} is defined as the minimum R_{wp} value reachable using a certain number of refinement parameters:

$$R_{exp} = \left[\frac{(N-P)}{\sum w_i (I_{oi})^2}\right]^{1/2} \qquad \cdots \qquad (2.40)$$

where N is the number of experimental data points and P is the number of fitting parameters. The refinement continuous till the GoF value converges and reaches near 1. The profile fit analysis can be improved by employing the instrumental and wavelength dispersion functions, where we get realistic specimen parameters. After the refinement, the profile parameters like the peak position, profile width and integrated intensity are obtained accurately which describes the specimen features such as crystallite size and microstrain. The final step is to separate the order independent size effects and order dependent strain effects from the specimen broadening. Howard and Snyder in the program SHADOW [**112**] considered simple isotropic broadening with profile shape as convolution of two Lorentzian shape functions. The modeling will yield another Lorentzian function due to crystallite size and microstrain. Bremen Rietveld Analysis and Structure Suite (BRASS) program [**113**], which employs phenomenological model proposed by Stephens [**108**], accounts for the anisotropic broadening and will yield crystallite size and microstrain parameters with Lorentzian and Gaussian shape functions. The Fourier modeling of XRD line profiles due to linear and planar defects are incorporated in Whole Powder Pattern Fitting (WPPF) Rietveld method by Scardi and Leoni [**114**]. In this approach an analytical function is adopted to fit the experimental profiles and the profile parameters are connected by suitable microstructural conditions. The alternative method to WPPM is Convoluted Multiple Whole Profile (CMWP) software package which is based on fitting the theoretical Fourier coefficients or inverse Fourier coefficients to the observed pattern after deconvolution of instrumental broadening [**30**]. In this model each peak position and intensity are constructed independently to determine the median and standard deviation of domain size distribution, dislocation density (ρ), outer cutoff radius (R_e) and contrast factor parameters. There are many other Rietveld refinement programs such as GSAS [**115**], FuLLPROF [**116**], XMAX [**117**] in which the profile broadening due to lattice defects can be modeled.

2.7 Hardness measurements

Hardness is defined as the resistance to the localized plastic deformation induced by external mechanical load or indentation. A hardness test is generally conducted to determine the suitability of a material to fulfill a certain purpose. The hardness measurement methods are classified in to three different types depending on the manner in which the tests are conducted, such as scratch, indentation, and rebound methods. Scratch hardness test is generally used for measuring the relative hardness of various minerals by scratching with other material. In rebound method, the indenter (generally ball shaped) is dropped from a height on to the metal surface. The rebound method provides hardness in terms of the rebounding height of the indenter. Conventional indentation hardness tests, such as Brinell, Vickers, Rockwell, and Knoop hardness, provide a single hardness value which is most useful as it correlate to different properties of the material, such as wear resistance, ductility, and strength.

In this section, only Vickers indentation hardness test is discussed. In Vickers test, a square pyramid shape diamond indenter is used. The perfect indentation looks like square shape as shown in Fig. 2.1a. The sinking of metal around the flat faces causes the indentation shape looks like pincushion as shown in Fig. 2.1b. The ridging of the metal around the faces of indenter causes barreled shape indentation as shown in Fig. 2.1c. The shape of indentation basically indicates the type of ageing treatment undergone by the material, such as annealing, cold work, strain ageing, and age hardening [**46**].

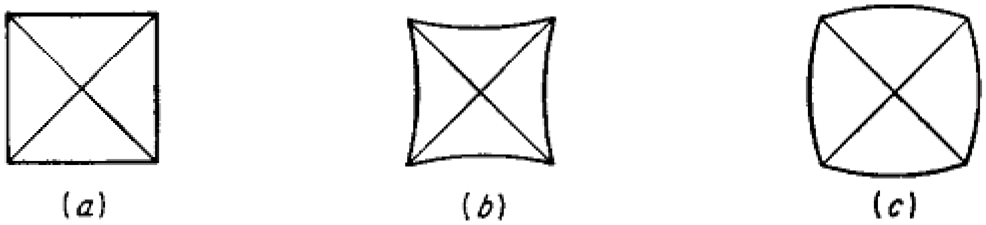

Fig. 2.1. Shape of pyramid indentations a) perfect indentation, b) pincushion indentation and c) barreled indentation

2.8 Electrical conductivity measurements

The electrical conductivity is one of the most important physical properties of engineering materials. The electrical conductivity is defined as the ease of flow of electron particle in the material. Based on Ohm's law the electrical conductivity is defined as the ratio of current density to electrical field strength. The Drude model for electron conduction in solid materials states that the current density, J is dependent upon the number of electrons per unit volume, n_e, the charge per electron, e, mass of electron, m, the relaxation time or mean free time between ionic collisions, τ and the electrical field, E. Comparing the Ohm's law and Drude model the electrical conductivity of a material can be determined from the following equation:

$$\sigma = \frac{ne^2\tau}{m} \quad \ldots \quad (2.41)$$

In a solid material, the relaxation time (τ) which influences the electrical conductivity varies mainly due to scattering effect caused by 1) impurities/defects and 2) temperature. The solid materials are classified based on their electrical conductivity (σ) values as insulators (< 10^{-8} S/m), semiconductors (10^{-6}-10^{4} S/m) and conductors (~10^{6} S/m).

2.9 Kinetics of phase transformation in Metals and alloys

In this section, we will simply look at the isothermal transformation kinetics of solute atoms to solid crystalline material. During the transformation process, there must be enough thermal energy for individual atoms to reorient themselves into solid crystalline material at constant temperature. The rate of transformation of solute fraction to crystalline material (f), is proportional to fraction of remaining solute atoms ($1-f$), ageing time (t) and is given by [Eqn. (2.43)]

$$\frac{df}{dt} = nk(1-f)t^{n-1} \qquad \cdots \qquad (2.42)$$

where n is the reaction order or Avrami exponent, k is the reaction rate constant. The solution of equation (2.42) is the fraction of solute atoms (f) transformed to crystalline material is given by Johnson–Mehl–Avrami (JMA) equation [**118**]:

$$f = 1 - \exp(-(kt)^n) \qquad \cdots \qquad (2.43)$$

The Avrami exponent (n) signifies the physical interpretation such as the growth of crystals occurring on the surface or in the matrix. The dependency of reaction rate constant at an absolute temperature (T) is based on the fraction of molecules having a minimum energy (known as activation energy (E_a)) to form products. The relationship between reaction rate constant (k) and (E_a) is given by Arrhenius equation [**119**]:

$$k = k_o e^{\left(\frac{-E_a}{RT}\right)} \qquad \cdots \qquad (2.44)$$

where k_0 is a constant for a given material and R is the gas constant. The kinetics of activated transformations can be described using these relationships.

3 Experimental Procedure

This chapter provides the information about the chemical composition of 304 HCu steel and its ageing conditions under different cold work conditions, for studying the precipitation kinetics behaviour. The details of the experimental techniques used to study the microstructural changes like X-ray diffraction and electrical conductivity would be presented. The details of hardness measurements carried out to evaluate the change in strength would also be briefed.

3.1 Material and heat treatment:

A seamless tube of Cu modified AISI type 304 stainless steel (304HCu steel with face centered cubic (f.c.c) structure) whose dimensions are 52 mm outer diameter and 9.5 mm wall thickness was considered for specimen preparation. (The 304HCu stainless steel specimens were prepared from tubular structure which is used as boiler tubes in advanced ultra super critical plants.) This tube was cut into rectangular specimen bars of approximately 51 mm (length) X 10 mm (width) X 7 mm (height) of dimension. The chemical composition of the as received 304HCu steel is shown in Table 3.1.

Table 3.1 Chemical composition of 304HCu steel (wt%)

Cr	Ni	Nb	Cu	C	Mn	Fe
18.00	9.00	0.45	3.00	0.10	1.00	Bal

The rectangular specimens were solution annealed (SA) at 1050 °C for 0.5 h followed by water quenching. These rectangular specimens were then cold worked (CW) for 10% (SA+10CW) and 20% (SA+20CW) reduction in thickness. These cold worked rectangular shape specimens were further cut into three pieces and they were isothermally aged at 650 °C for different ageing durations of 0.25, 0.5, 1, 3, 5, 22 and 100 h followed by water quenching.

3.2 Angle dispersive X-ray diffraction

3.2.1 Details of diffractometer

The angle dispersive X-ray diffraction (ADXRD) beamline BL-12 at INDUS-2, the Indian synchrotron radiation (SR) source is dedicated for determination of the crystallographic structures of materials. INDUS-2 is a synchrotron accelerator of electron particles of current 300 mA and energy 2.5 GeV. The beam acceptance is 2 mrad (H) X 0.15 mrad (V) and the photon energy lies in the spectral range of 5-25 keV. The optical layout of the beamline is shown in Fig. 3.1. The beamline consists of Si (311) based double crystal monochromator (DCM) for selecting the required photon energy. The second mirror in DCM is also used for sagittal plane focusing of the beam. The optical elements of pladium coated pre-mirror and post mirror are used for aligning the beam path as well as vertical focusing of the beam. The beam size can be focused to a size of 0.5 mm (width) and 0.6 mm (length). The available diffraction data acquisition detectors are NaI (Tl) Scintillation point detector, MYTHEN detector (based on silicon microstrip sensor) and Image plate (Mar 345) area detector. These setup of optics and detectors give highly parallel beam, low background and a resolving power of $\Delta E/E \sim 10^4$ (at 10 keV) [**11**,**120**].

3.2.2 XRD data acquisition and analysis

X-rays of energy ~15.46 keV is selected for data acquisition by aligning the DCM optical element. Few peaks positions of LaB_6 standard are used for calibrating the energy of monochromatic X-ray beam. Alignment of detector with beam is made based on half cut intensity method. The height of the specimen is adjusted by using the combination of both half cut intensity method and rock scan movement of specimen stand. The XRD pattern of the solution annealed and cold worked 304HCu samples were recorded for an angular range (2θ) from 17 to 48° with a step size of 0.01°. For obtaining the instrumental function, the complete 2θ spectrum under study from LaB_6 powder was recorded.

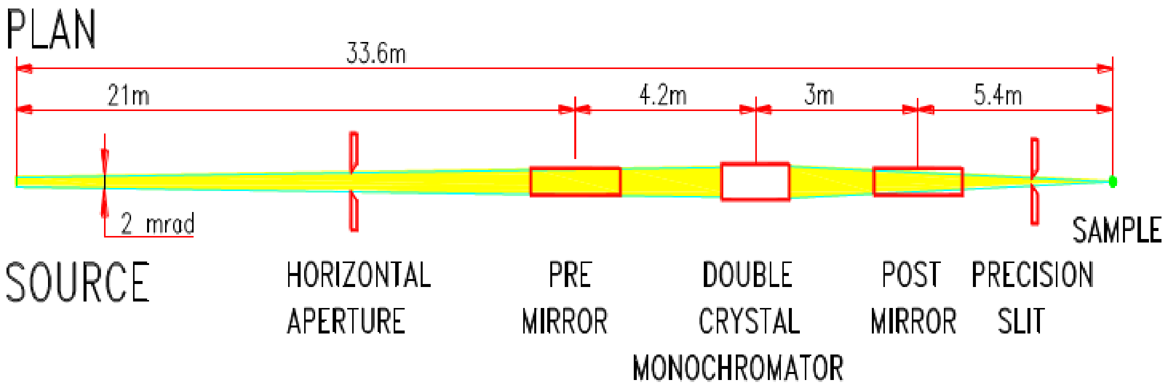

Fig. 3.1. Optical layout of the beam line [120].

The XRD profiles thus obtained are analysed by fitting each individual peak with pseudo-Voigt functions after accounting for a suitable background subtraction. The peak profile parameters like peak position, full width at half maximum (FWHM) and Gauss content are refined. However, the whole profile pattern fitting was carried out using BRASS code, in order to compare different methods as discussed in chapter 4. In BRASS code there are different parameters which are refined such as atomic positions, thermal and site occupancy parameters, parameters for background, lattice parameters, parameters representing instrumental geometrical-optical features and specimen aberration (e.g. specimen displacement and transparency) and specimen profile broadening parameters (S-parameters). These parameters are refined in each and every step with the calculation of residual.

3.3 Electrical conductivity

The electrical conductivity measurements of the specimens under study were carried using SIGMATEST 2.069 (Supplier, M/s. Foerster, U.S.A). The conductivity meter (SIGMATEST 2.069) is an eddy current based instrument which measures the electrical conductivity of non-ferromagnetic metals based on substantial changes in complex impedance of the measuring probe. The instrument can be operated in 5 different frequencies and appropriate operating frequencies among 60, 120, 240, 480, and 960 kHz can be selected. The electrical conductivity measurements were obtained at all of these frequencies and the average is used for the analysis. The instrument can be calibrated with the available standards of conductivity values 0.6097, 4.419, 17.32, 25.73, 34.74 and 58.34 M S/m (Mega Siemens/meter). After completion of calibration, the instrument was used to estimate the conductivity of specimens under study.

3.4 Hardness

The hardness measurements in 304HCu steel specimens were carried out at room temperature (300 K) using EW-423DAT digital Vickers hardness tester manufactured by M/s Innovatest. In Vickers hardness test, a square pyramid shape diamond indenter having 136° angle between opposite faces is used. This angle is chosen because of the following reasons: to maintain the ratio of indentation diameter to indenter same as that of ball indenter in the Brinell hardness test. The Vickers hardness number (VHN) is defined as the applied load (Kgf) divided by surface area (mm^2) of the indentation and it can be determined from following equation:

$$\mathrm{VHN} = \frac{2\mathrm{F}\sin(\theta/2)}{D^2} \quad \dots \qquad (3.1)$$

where F = applied load

D = average indentation diagonal length

Θ = angle at diamond tip between opposite faces

The range of the applied load used in this test varies between 1 and 120 kgf, depending upon the hardness of the material under study. In this study the hardness measurements were carried out with a load of 0.5 kgf with dwell time of 15 sec. The indentation diagonal length was measured with the help of microscope attached with the instrument and the hardness values were calculated by using Eqn. (3.1). A minimum of five readings were taken for each sample and the average value was determined.

Chapter 4

4 Comparison of various profile analysis approaches for separating precipitation and dislocation effect

In this chapter the microstrain estimated by different XRD line profile analysis (XRDLPA) methods like modified Williamson Hall (mWH) method, Fourier based Warren Averbach (WA) method and Stephens phenomenological model would be compared to understand the influence of precipitation and dislocation on microstrain development in a material. Towards this objective, isothermally aged 17-4PH SS has been chosen which has been studied earlier by mWH method [**47**]. In this material, during ageing at 380, 430 and 480 °C for 0.5, 1 and 3 h durations, simultaneous precipitation and dislocation annihilation would take place [**121**]. The comparative analysis of the various size-strain separation approaches adapted to study 17-4 PH steel would enable in understanding the influence of cold working on ageing behaviour of SS 304HCu steel which would be presented in the later chapters (5 and 6).

4.1 XRD profile refinement

The whole XRD powder patterns of 17-4 PH steel samples in the angular range of 33° to 122° were refined using BRASS code [**113**]. For all samples the R_{wp} is lesser than 15.75 and GoF is greater than 1.78. The refined peak fit and XRD experimental data are shown in Fig. 4.1 as solid line and open circles respectively, for solution annealed (SA) as well as isothermally aged 17-4 PH samples at 480 °C for 0.5 h & 1 h durations. The goodness of fit (GOF) for refined profiles of SA, isothermally aged samples at 480 °C for 0.5 h and 1 h durations is 2.12, 3.25 and 2.07 respectively. However, the goodness of fit (GOF) ranges from 1.78-2.79 for refined profiles of all other samples. In Fig. 4.1, the intense peaks correspond to (110), (200), (211), (220) and (310) reflections of primary martensite matrix phase. Indeed, the formation of additional *f.c.c* phase is observed in aged samples which are indexed in Fig. 4.1. The FWHM values directly obtained from least square fitting using pseudo Voigt function for solution annealed (SA), 0.5 h and 1 h aged 17-4 PH samples at 480 °C temperature and the values are given in Table 4.1.

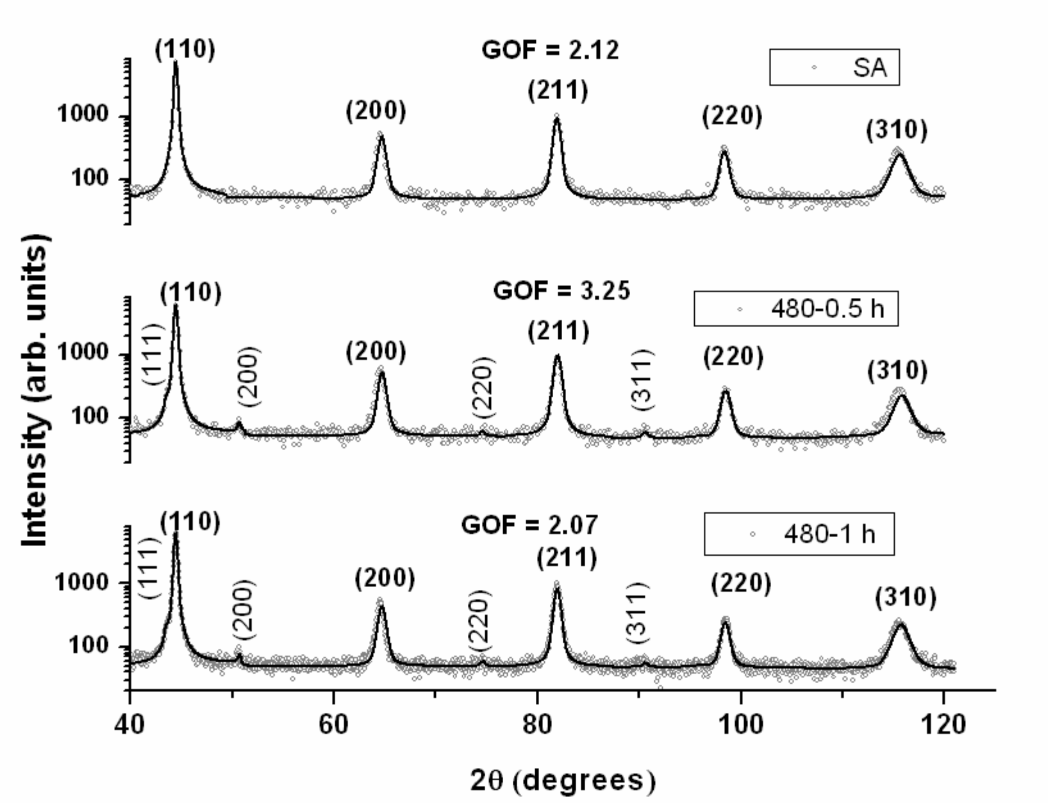

Fig. 4.1 The diffraction pattern (open circle) along with refined profile (solid line) X-ray diffraction

Table 4.1 The FWHM values obtained from least square fitting for SA, 0.5 h and 1 h aged 17-4 PH samples at 480 °C

Heat treatment	FWHM along with peak position of (hkl) reflecting planes				
	(110)	(200)	(211)	(220)	(310)
SA	0.3°	0.689°	0.567°	0.647°	1.315°
480 – 0.5 h	0.336°	0.709°	0.639°	0.771°	1.568°
480 – 1 h	0.303°	0.624°	0.597°	0.695°	1.439°

4.2 Stephens anisotropic model

The Reitveld refinement tool, BRASS code uses Stephens anisotropic model for carrying out profile analysis. The Stephens strain parameters (S_{400} & S_{220}) obtained for all the refined profiles are given in Table 4.2. In Table 4.2, it is seen that the Stephen's strain parameter S_{400} is a positive parameter which lies between 12.75E-2 and 8.20E-2 and S_{220} is a negative parameter which lies between -3.71E-4 and -1.30E-2. The earlier study of cubic system (Superconductor-RB_3C_{60}) carried out by Stephens [**108**] revealed the value of strain parameters S_{400} and S_{220} as 3.43E-8 and -1.13E-8 respectively. These strain parameters are used in calculating Stephens anisotropic broadening and normalised strain based on Eqn.(2.35) and Eqn.(2.36) respectively.

Table 4.2 The refined strain parameters from Stephens anisotropic model

Heat treatment		Stephens strain parameters	
Temperature (°C)	Time (h)	S_{400}	S_{220}
Solution annealed (SA)		11.11E-2	-2.75E-2
380	0.5	9.23E-2	-1.35E-2
	1	11.78E-2	-3.21E-2
430	0.5	10.39E-2	-1.94E-2
	1	12.75E-2	-3.38E-2
	3	10.22E-2	-1.30E-2
480	0.5	10.31E-2	-9.20E-3
	1	10.68E-2	-2.87E-2
	3	8.20E-2	-3.71E-4

4.2.1 Stephens anisotropic broadening

The full width at half maximum (FWHM) calculated by using Eqn.(2.35) based on Stephens strain parameters has shown anisotropic order-dependent broadening. It is also to be noted from Table 4.1 that the broadening observed for the 5 bcc reflections are not isotropic with diffraction angle and needs to be addressed. The observed increase of XRD peak broadening in Table 4.1 at initial ageing is due to increase in coherency strains caused by newly formed precipitate phases [**56**]. The dependency between the FWHM measured from Stephens model and the FWHM obtained from least square refinement is linear as shown in Fig. 4.2. The linear correlation indicates that the FWHM estimated from the model and experimental results are in agreement with each other. Stephens [**108**] showed a linear behaviour between the FWHM measured from the strain parameters and the FWHM refined from Le Bail fitting.

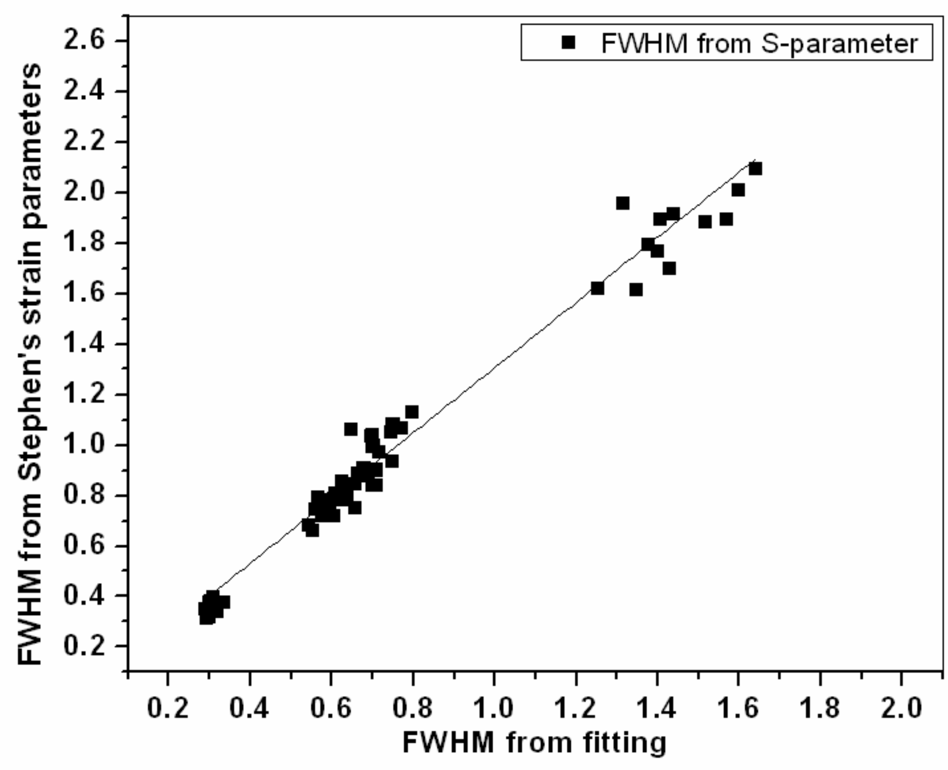

Fig. 4.2 The variation in FWHM from Eqn.(2.35) (Stephens model) is plotted with the FWHM determined from least square refinement.

4.2.2 Microstrain from Stephens model

The strain parameters S_{400} & S_{220} obtained from Reitveld refinement tool (BRASS code [**113**]) are used in Eqn. (2.36), for calculating the strain (δ_{hkl}) along all the *hkl* reflections. In this model, the Stephens normalized strain (α_S) is calculated from the root mean square of strains (δ_{hkl}) determined along (110), (200), (211), (220) and (310) directions based on the following equation:

$$\alpha_S = \sqrt{\frac{\sum \delta_{hkl}{}^2}{n}} \qquad \ldots \qquad (4.1)$$

where n is the number of peaks and herein five peak reflections are considered. The Stephens normalized strain (α_S) obtained for all the refined profiles are given in Table 4.2. The variations of microstrain (α_S) with isothermal ageing at temperature of 380, 430 and 480 °C are shown in Fig. 4.3. During initial ageing at 380 and 430 °C for 0.5 h, the microstrain α_S decreased (from SA condition) which indicates that the decrease in microstrain due to dislocation annihilation is much larger than the increase in coherency strains due to precipitation. However, on further ageing the increase in α_S is attributed to the increased contribution of precipitation induced strain. The variation of α_S derived from whole profile analysis (Stephens model) includes the tail region, which is affected by dislocations and precipitate induced effects.

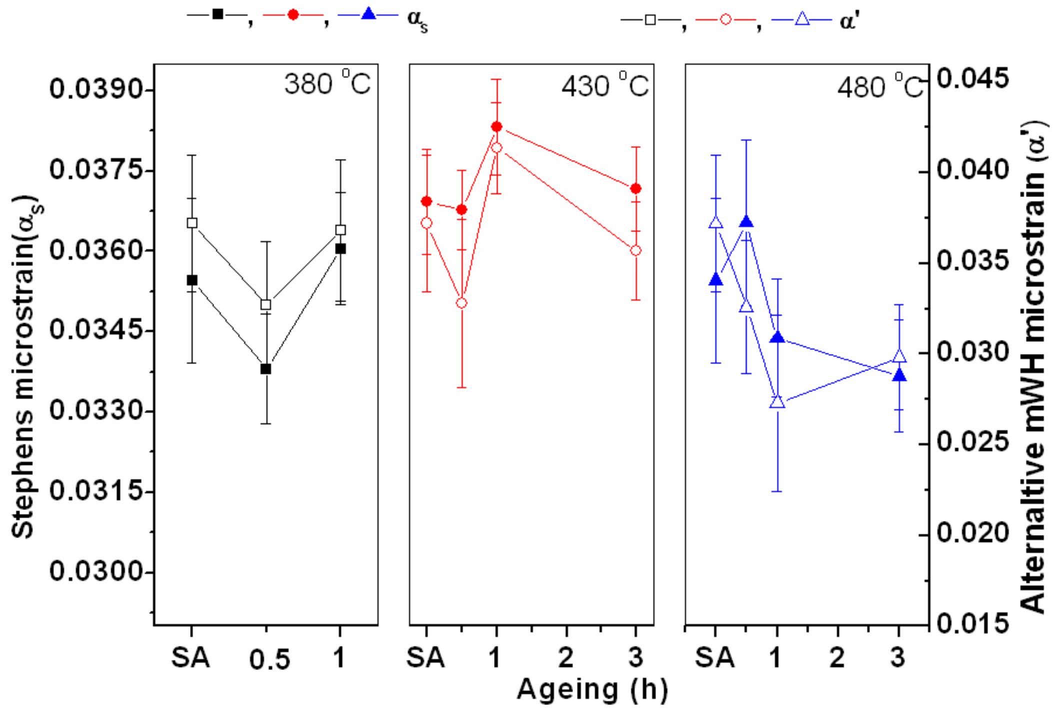

Fig. 4.3 The variations in microstrain (α_S) from Stephens model and microstrain (α') from alternative mWH analysis

4.3 Microstrain from mWH analysis

The microstrain (α) is determined from the slope of plot between FWHM and corrected diffraction vector ($K\bar{C}^{1/2}$) using mWH analysis based on Eqn. (2.30). The variation in α at different heat treatment is given in Table 4.3. The increase in microstrain during initial ageing for 0.5 h at 380 and 430 °C has indicated the early occurrence of precipitation [**47**]. After attaining peak microstrain at all isothermal temperatures, the observed reduction in microstrain indicated that the precipitate coarsening is dominant factor. The variation in microstrain is further discussed in § 4.7. A similar behaviour of precipitation on microstrain was also studied in M250 grade maraging steel using XRDLPA [**53**]. On the other hand, the microstructure of the solution annealed 17-4 PH SS is found to have parallel lath martensites having a high dislocation density. In this material, the influence of dislocation annihilation on the microstrain has not been thoroughly addressed. As the evaluated microstrain has contribution from coherent precipitates and dislocations which annihilate on ageing, it would be beneficial to separate these contributions. Assuming the strain broadening of diffraction profiles is due to dislocations alone, Ungar et al. [**111**] proposed a model based on modification of Williamson Hall method based on Eqn. (2.31). Using this approach for all aged samples, the microstrain (α′) is determined from mWH plot which starts with zero slope and the values are listed in the last column of Table 4.3. Fig. 4.4 shows the variation in XRD peak broadening of samples aged for 30 min at 380 °C and 480 °C with respect to $K\bar{C}^{1/2}$. The mWH plots fitted based on Eqn. (2.30) & (2.31) are also shown as dotted and continuous lines respectively. The mWH curve fitted with Eqn. (2.31) shows lesser weightage to the low angle peaks and revealed a higher value of microstrain (α′) as compared to microstrain (α) obtained from the fit with Eqn. (2.30). However, in deformed Cu specimens the XRD peak broadening are well fitted with a smooth curve based on Eqn. (2.31) showing a parabolic nature [**111**]. In Fig. 4.3, the variation in microstrain (α′) determined from Eqn. (2.31) is shown, it decreases at initial ageing for three different ageing temperatures, indicating the microstrain (α′) is more influenced by dislocation annihilation changes that occur during ageing.

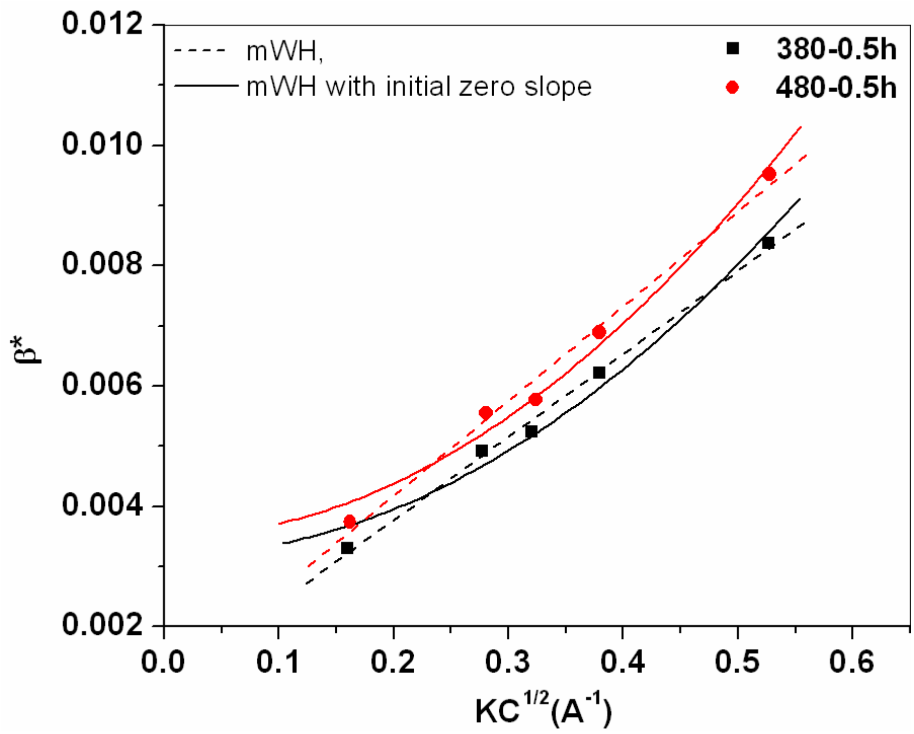

Fig. 4.4 The mWH plots based on Eqn. (2.30) & (2.31) for samples aged for 0.5 h at 380 and 430 °C

Table 4.3 The microstrain (α) from [Eqn.(2.36)] and microstrain (α′) from alternative mWH analysis [Eqn. (2.31)]

Heat treatment		mWH method	
Temperature (°C)	Time (h)	Microstrain (α)	Microstrain (α′)
Solution annealed (SA)		0.0126	0.03719
380	0.5	0.0145	0.03269
	1	0.0179	0.0328
430	0.5	0.0146	0.03726
	1	0.0180	0.04136
	3	0.0159	0.05069
480	0.5	0.0156	0.03258
	1	0.0145	0.04027
	3	0.0141	0.02982

4.4 The variation of crystallite size

The variation in crystallite size (*D*) obtained from mWH method based on Eqn.(2.30) is plotted in Fig. 4.5. From Fig. 4.5, the substructural refinement of solution annealed sample on ageing for 3 h at 430 °C and 480 °C is indicated with a change in *D* value from 62 nm to 139 nm and 95 nm respectively. The Williamson and Smallman [**122**] approach of calculation of dislocation density (ρ_D) from crystallite size is given by $\rho_D=3/D^2$. The dislocation density (ρ_D) from crystallite size increases with ageing of 3 h duration. The increase in dislocation density at 3 h ageing is attributed to formation of misfit dislocations during coarsening of precipitates. In order to confirm these findings the microstructure were obtained. Fig. 4.6 (a)-(c) show the microstructure of SA sample, samples aged for 3h at 430 and 480 °C. Fig. 4.6 (a), shows a typical martensitic structure with fine substructure which is indicative of higher dislocation density. The 3 h aged samples show decrease in substructure size at 480 °C as compared to 430 °C which is attributed to sub-boundary pinning by dislocations and misfit dislocations.

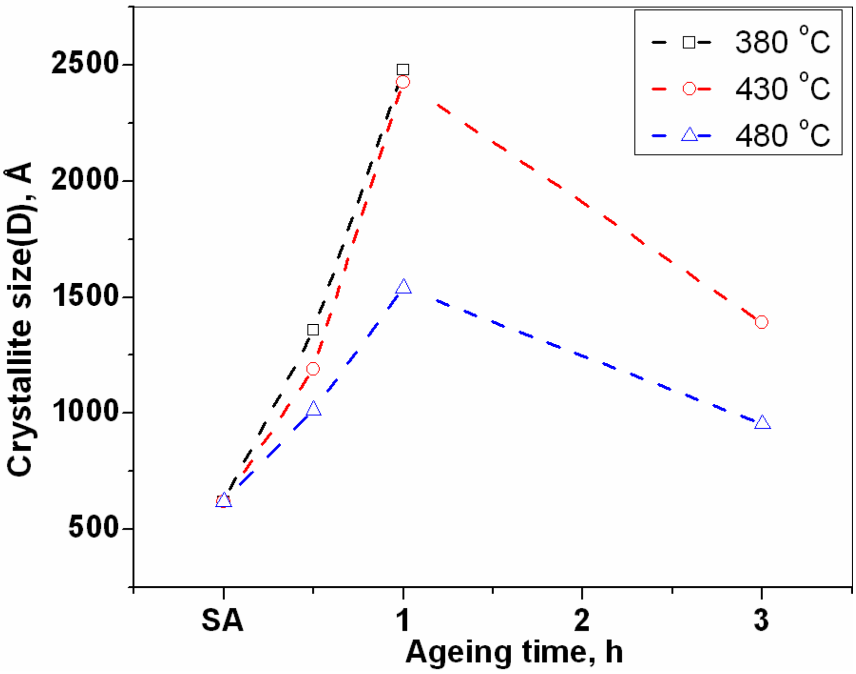

Fig. 4.5 The variation of crystallite size D with isothermal ageing duration at 380, 430 and 480 °C temperature.

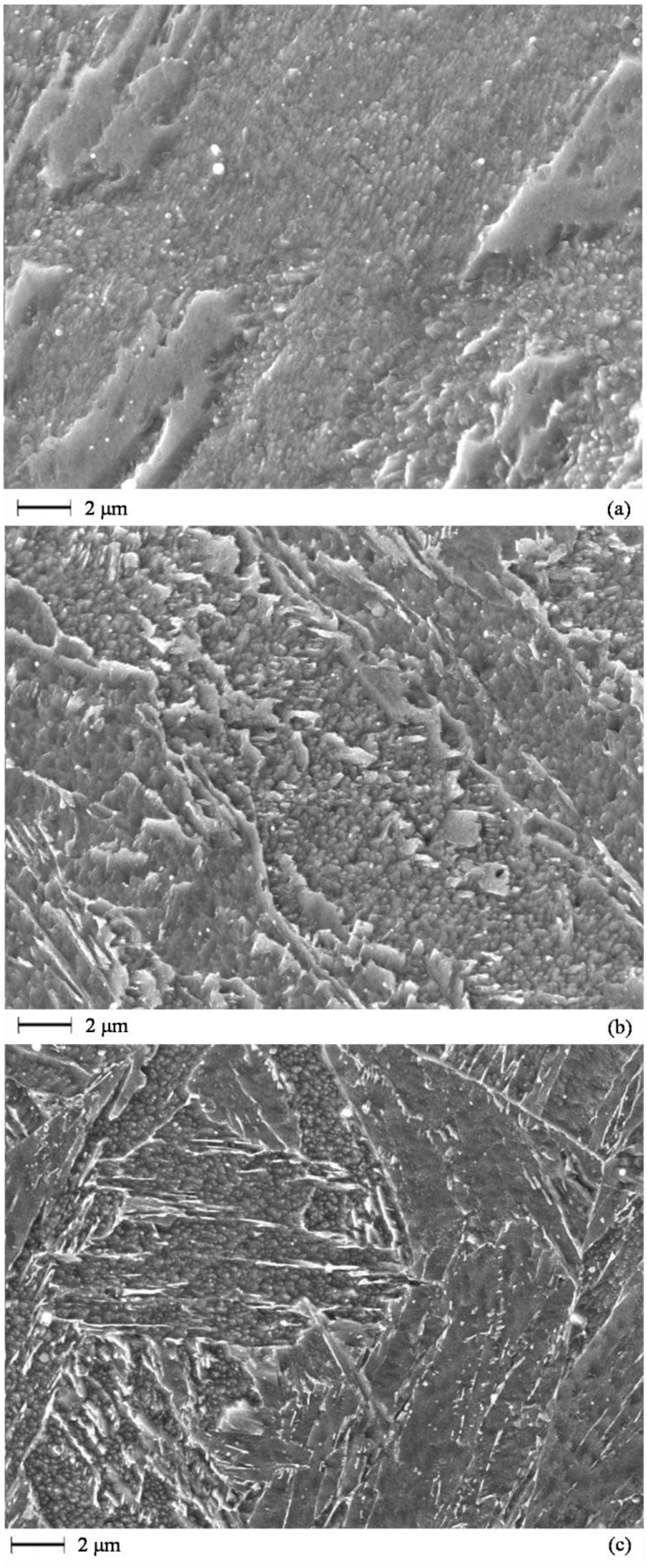

Fig. 4.6 The micrographs of (a) SA, (b) aged at 430 °C for 3 h, and (c) aged at 480 °C for 3 h samples obtained from SEM.

4.5 Comparison of microstrain α_S, α and α'

The dependency of microstrain determined from different profile analysis due to dislocations and precipitate induced effects is compared at various ageing duration. Fig. 4.7 shows the variation of microstrain (α') with the variation of microstrain (α_S) determined from Stephens model for all aged 17-4 PH specimens. The variation in α' and α_S shows a linear behaviour and hence it is understood that Stephens normalized strain (α_S) is equivalent to the microstrain determined from mWH method based on Eqn. (2.31).

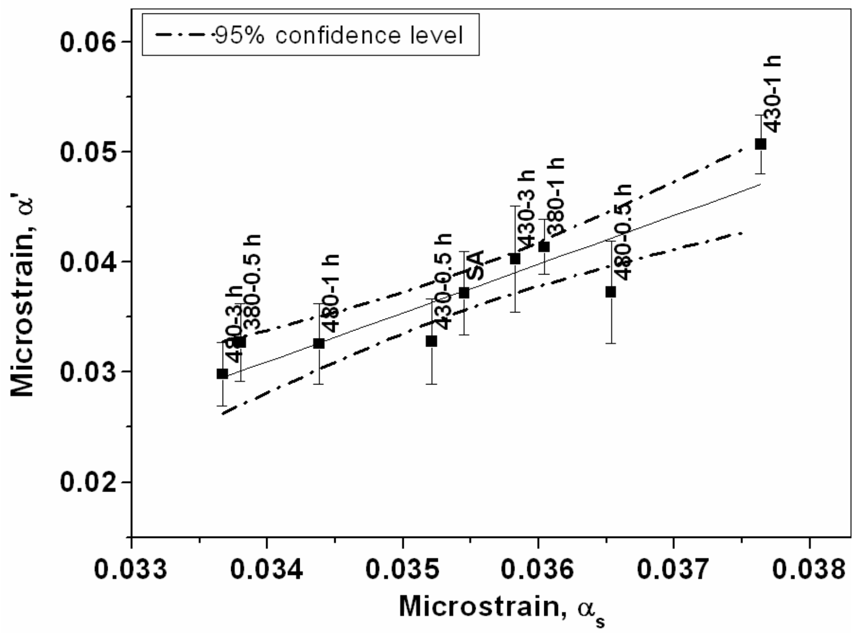

Fig. 4.7 The variation of microstrain (α') and microstrain (α_S) of Stephens model for aged 17-4 PH specimens.

During initial ageing of 0.5 h in 380 & 430 °C both α' and α_S decrease which is attributed to dominant dislocation annihilation induced strain (Fig. 4.3). On the other hand, the microstrain (α) increases at initial ageing of 0.5 h in 380 & 430 °C as shown in Table 4.3. which indicates that coherent precipitates induced strain is dominant. However, the peak value of α, α' and α_S is seen at same ageing durations in all temperatures. This is attributed to the increased contribution of precipitation induced strain to the increase in α' and α_S. At higher ageing durations of 3 h, α' and α_S is found to decrease, which is similar to the behaviour observed by α. This is attributed to the fact that precipitate coarsens and results in loss of coherency at larger ageing durations.

The variation in α which shows dominant precipitation effects [**47**] doesn't fall in line with the variations observed in α' and α_S which show both precipitation and dislocation annihilation effects. Hence, the difference $\Delta\alpha_d = (\alpha_S - \alpha)$ between microstrain α_S estimated from integral breadth (based on Stephens model) and α estimated from FWHM (mWH method) is a measure of the changes in tail region of the XRD profiles. The tail region of XRD profiles is mostly dominant by dislocation effects. So, the difference in α_S and α can be justified with the variation in dislocations.

4.6 Fourier based analysis

The Fourier analysis is based on the classical WA approach (based on Eqn.(2.27)) in which the two ordered peaks of bcc matrix (110) and (220) are considered which would give the strain as a function of column length along (110) direction based on the procedure mentioned in § 2.4.2. However, the peaks corresponding to (110), (211) and (220) having same H^2 values of 0.25 are considered for Fourier analysis. Using the Fourier method for these three peaks based on Eqn.(2.27), the slope between logarithm of Fourier amplitude with respect to $1/d^2_{hkl}$ (d_{hkl} –spacing between hkl planes) will provide the mean square strain $\langle\varepsilon^2(L)\rangle$ as a function of column length. The Fourier analysis is carried out for all aged 17-4 PH samples. Fig. 4.8 shows the plot between logarithm of Fourier coefficient [ln(A(L))] of solution annealed (SA) 17-4 PH sample with respect to $1/d^2_{hkl}$ at L values of 10, 20, 30, 40 and 50 Å. The R^2 value of the linear fit is greater than 0.98 and indicates the broadening of the reflections (110), (211) and (220) having same H^2 values are isotropical in nature.

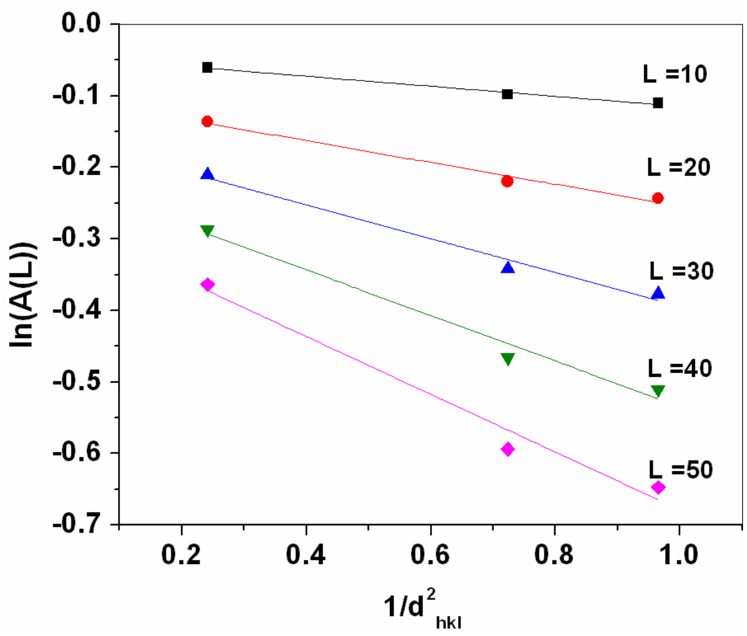

Fig. 4.8 The variation of logarithm of Fourier coefficient plotted versus $1/d^2_{hkl}$ at L values of 10, 20, 30, 40 and 50 Å

4.6.1 Dependency of microstrain on column length

The dependency of $\langle\varepsilon^2(L)\rangle$ on column length by various authors is discussed in § 2.3.3. Rothman and Cohen [**123**] assumed that the mean square strain which represents the strain field around dislocations, decay with the distance perpendicular to reflection planes (L) i.e., $\langle\varepsilon^2(L)\rangle \propto 1/L$. Similarly, Wilken's assumed the mean square strain with logarithmic approximation i.e., $\langle\varepsilon^2(L)\rangle \propto ln(1/L)$. The mean squared strain as a function of column length (L) of 17-4 PH steel aged at 480 °C for 0.5 h are fitted with Wilken's approximation, Rothman model and Balzar method (Eqn. (2.18)) and are shown in Fig. 4.9.

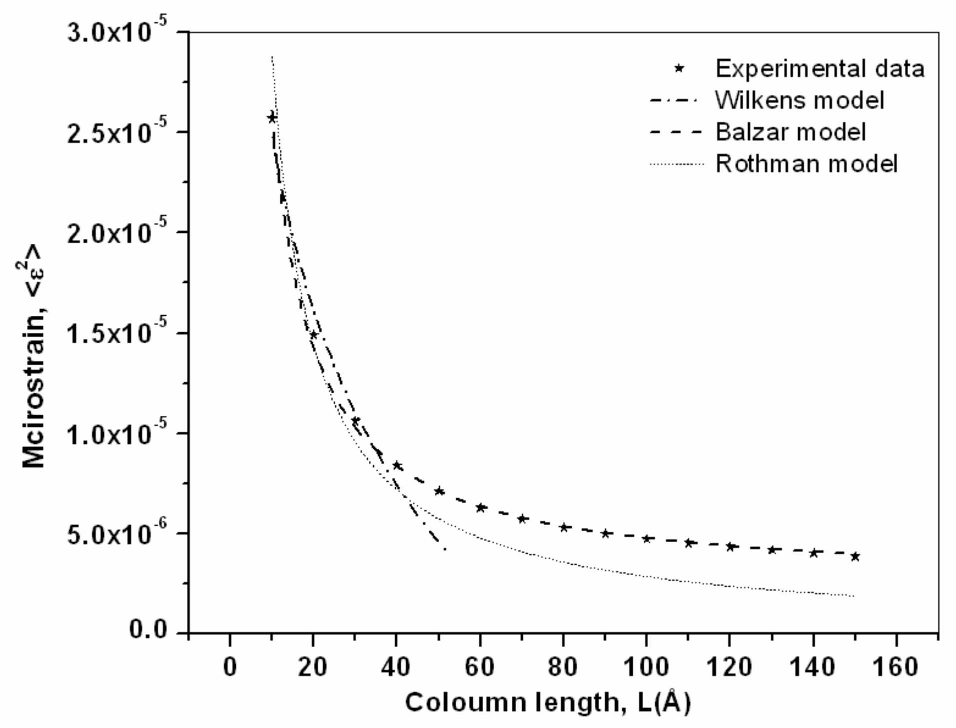

Fig. 4.9 The schematic shows the fit of Wilkens function for small values of L, Balzar approach and Rothman approach as a function of column length (L) for an experimental data.

In Fig. 4.9, the experimental data is shown as star symbol. It is observed that Wilken's method and Rothman method fitted well for smaller L values, but failed to fit at higher L values. However, Balzar method is able to fit the estimated strain $\langle \varepsilon^2(L) \rangle$ for all the column length range. The comparison of dependency of mean squared strain as a function of column length (L) shows that the residual of the fit from different approximations to the experimental data of $\langle \varepsilon^2(L) \rangle$ is different.

An alternative expression (Eqn. (4.2)) is proposed for fitting the mean square strain $\langle \varepsilon^2(L) \rangle$, which is similar to Balzar method with an inclusion of additional term as given by following equation:

$$\langle \varepsilon^2(L) \rangle = P_0 + \frac{P_1}{L} + \frac{P_2}{L^2} \qquad \dots \qquad (4.2)$$

where P_0 is long-range strain parameter, P_1 is short range strain parameter and P_2 is higher order term.

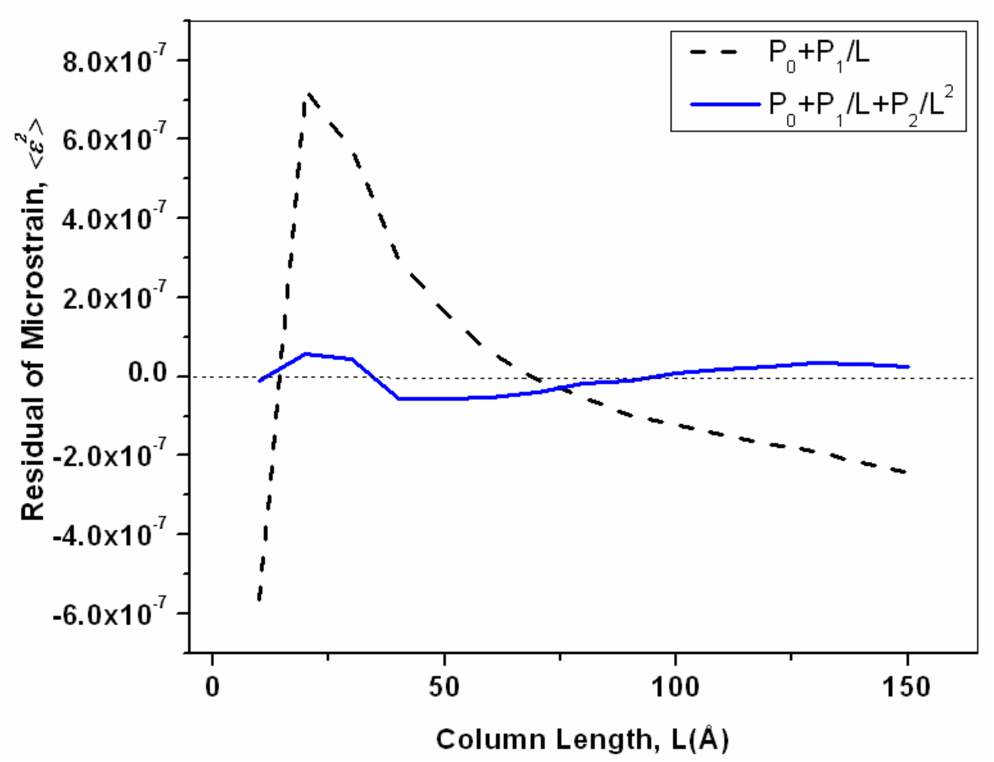

Fig. 4.10 Difference between estimated strain and fitted strain using Eqn. (2.18) and Eqn. (4.2) as a function of column length for SA sample.

The Eqn. (4.2) is identical to the logarithmic expansion of Wilkens model and limiting the same to second order term. Fig. 4.10 shows the difference (residual) between the estimated strain $\langle \varepsilon^2(L) \rangle$ and fitted strain from the approximation using Balzar model [Eqn. (2.18)] and proposed model [Eqn. (4.2)] as dashed line and solid line respectively for solution annealed 17-4 PH sample. In the Balzar model (dashed line fit), the Eqn. (2.18) is rewritten in terms of parameters P_0 and P_1 which are proportional to Cauchy (β_{DC}) and Gaussian $(\beta_{DG})^2$ component of broadening respectively. In Fig. 4.10 it is observed that the residual of

$\langle \varepsilon^2(L) \rangle$ is minimum when fitted with Eqn. (4.2) as compared to Eqn. (2.18) for SA 17-4 PH sample. Thus, the proposed model [Eqn. (4.2)] is an approximation to the Balzar method by including an additional term (P_2) improves the fit of column length dependent mean square strain $\langle \varepsilon^2(L) \rangle$. A different approximation was considered in the alternative approach of WA analysis studied by Van Berkum et al. [**124**], in which the Fourier coefficients of distortion is expanded into Taylor series of even order of L and $\langle \varepsilon^2(L) \rangle$. In their study, the approximation was carried out to minimize the random errors in experimental Fourier coefficients.

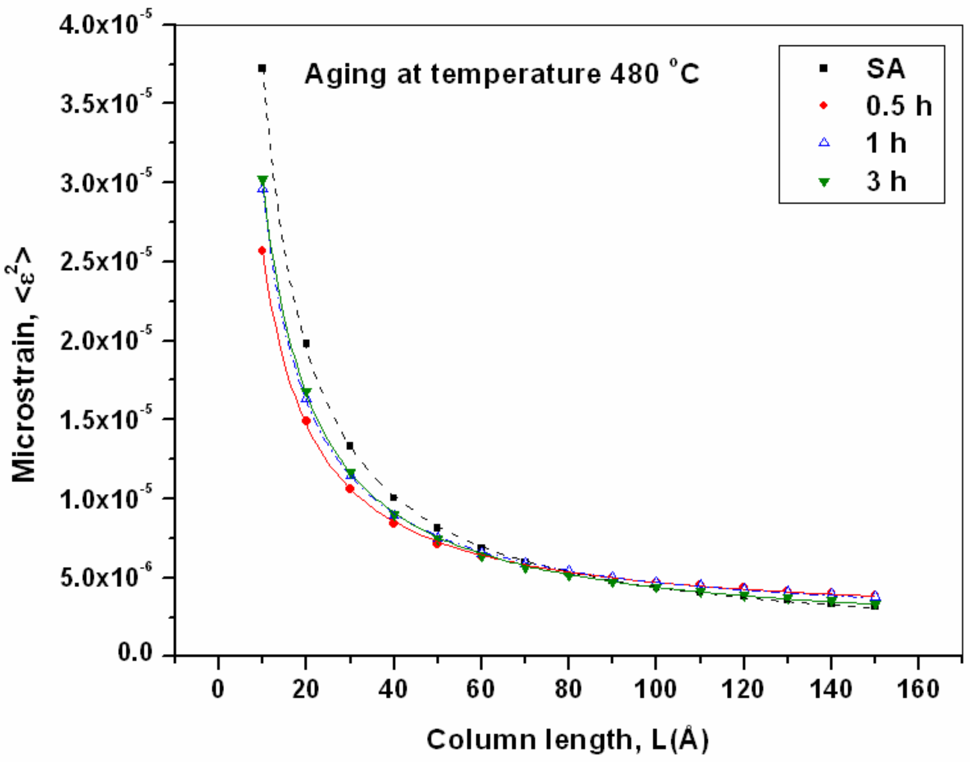

Fig. 4.11 The variation of microstrain as a function of column length along with the fit for the solution annealed (SA) and isothermally (480 °C) aged specimens

In this study, the estimated strain $\langle \varepsilon^2(L) \rangle$ is well fitted with Eqn. (4.2) and the parameters P_0, P_1 and P_2 are determined from the least square fit for all aged samples. These parameters P_0, P_1 and P_2 as a function of heat treatment are listed in Table 4.4. The variation in $\langle \varepsilon^2(L) \rangle$

as a function of column length L for solution annealed (SA) and 0.5, 1 and 3 h samples aged at 480 °C are shown as square, circle, triangle and inverted triangle symbols along with their fits using Eqn. (4.2) in Fig. 4.11. It is observed that the proposed Eqn. (4.2) fits well to $\langle \varepsilon^2(L) \rangle$ for all the aged samples.

Table 4.4 The values of P_0, P_1 and P_2 parameters for solution annealed and aged specimen under study are given below.

Heat treatment condition	P_0	P_1 (Å)	$\lvert P_2 \rvert$ (Å^2)	Strain at D_{eff} $\langle \varepsilon^2 \rangle^{0.5}$
SA	0.47×10^{-6}	3.95×10^{-4}	2.72×10^{-4}	0.00156
380-0.5h	1.47×10^{-6}	2.83×10^{-4}	1.64×10^{-4}	0.00169
380-1h	2.43×10^{-6}	2.54×10^{-4}	7.91×10^{-4}	0.00192
430-0.5h	1.30×10^{-6}	3.25×10^{-4}	2.75×10^{-4}	0.00169
430-1h	3.17×10^{-6}	2.56×10^{-4}	3.19×10^{-4}	0.00212
430-3h	1.78×10^{-6}	3.04×10^{-4}	2.20×10^{-4}	0.00185
480-0.5h	1.96×10^{-6}	2.86×10^{-4}	2.73×10^{-4}	0.00189
480-1h	1.77×10^{-6}	2.96×10^{-4}	1.79×10^{-4}	0.00182
480-3h	1.15×10^{-6}	3.28×10^{-4}	3.72×10^{-4}	0.00172

4.6.2 *The average strain ε^2 changes on ageing*

The observed variation of $\langle\varepsilon^2(L)\rangle$ as a function of column length L at different ageing conditions is defined by the three parameters P_0, P_1 and P_2. However, the average strain in the matrix is defined as the strain $\langle\varepsilon^2(L)\rangle$ at surface weighted size (D_{eff}) which is denoted by $\langle\varepsilon^2\rangle^{0.5}$. The variation of average strain $\langle\varepsilon^2\rangle^{0.5}$ at different heat treatment conditions are given in the last column of Table 4.4. The observed $\langle\varepsilon^2\rangle^{0.5}$ peaks at 1h ageing duration for 380 and 430 °C and on further ageing of 3 h duration it decreases. Thus, the variations in $\langle\varepsilon^2\rangle^{0.5}$ with ageing are similar to the changes observed in α_S as shown Fig. 4.3 apart from that, the $\langle\varepsilon^2\rangle^{0.5}$ doesn't show any dip at 0.5 h duration. During ageing treatment, the precipitate grows resulting peaking of microstrain and on over-ageing the precipitate gets coarsened causing the strain to decrease due to loss of coherency with the matrix. The earlier studies show the rearrangement of dislocations due to coarsening of precipitates takes place [**47**,**125**]. Thus, the variations observed in mean square strain $\langle\varepsilon^2(L)\rangle$ with ageing are influenced by simultaneous precipitation- and dislocations- induced effects. Krivoglaz [**96**,**104**] has classified lattice defects such as dislocations and point defects based on the decay of strain field as reciprocal or square of reciprocal of the distance from the defect. The $\langle\varepsilon^2(L)\rangle$ as a function of column length L based on Eqn. (4.2) suggests that $\langle\varepsilon^2(L)\rangle$ is combination of long range and short range strain fields represented by P_0 and P_1 respectively. The variation in P_0 and P_1 with ageing along with the variation in precipitation dominant microstrain (α) and dislocation desnity will be discussed in the following sections.

4.7 The microstrain α determined from mWH method and its equivalence with P_0

For comparison of microstrain (α) estimated by mWH method with P_0 derived from mean squared strain $\langle\varepsilon^2(L)\rangle$, the square root is analyzed i.e., $(P_0)^{0.5}$. Fig. 4.12 shows the variation of $(P_0)^{0.5}$ and α with ageing duration as solid and open symbols for temperatures of 380, 430 and 480 °C as squares, circles and triangles respectively. From Fig. 4.12, it is observed that solution annealed specimen has the lowest $(P_0)^{0.5}$ value. Upon ageing at 380 °C, it is observed that $(P_0)^{0.5}$ increases up to the ageing duration considered in the study. On ageing at 430 and 480 °C, $(P_0)^{0.5}$ increases up to 1 and 0.5 h respectively and beyond which $(P_0)^{0.5}$ decreases. The variation of α with ageing duration (open symbols) shows a similar trend as observed for P_0. It is to be noted that, the P_0 value corresponds to strain at longer column lengths, which in diffraction profiles corresponds to regions in the neighborhood of FWHM of the diffracted peaks. Hence, it is valid to use the parameter P_0 for studying the precipitation induced effects. However, it is noted that when dislocation density is high, the microstrain would extend to longer column lengths and dislocation contribution to P_0 cannot be ruled out. Hence, the changes in microstrain α determined from FWHM using the mWH method are similar to those of the long range strain parameter, P_0.

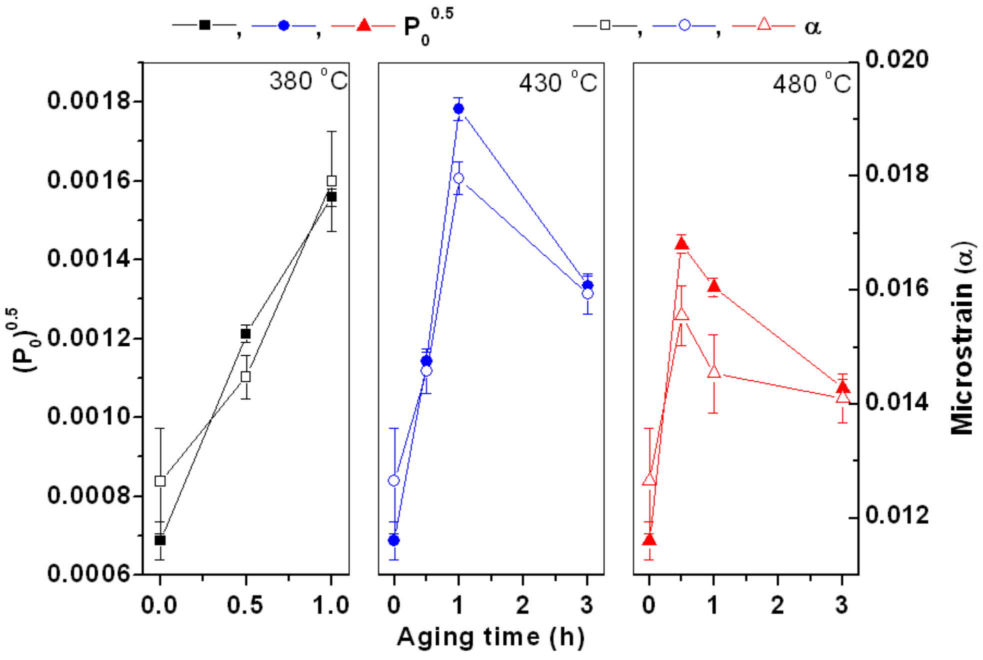

Fig. 4.12 Variation of the $(P_0)^{0.5}$ obtained from the fit to $\langle\varepsilon^2(L)\rangle$ using Eqn. (4.2) and microstrain (α) determined based on Eqn.(2.30).

4.8 Comparison of dislocation parameter with microstrain

The Williamson and Smallman [**122**] approach of calculation of dislocation density from crystallite size and strain broadening is used in this study. According to Williamson Smallman approach, the dislocation density (ρ_D) due to crystallite size is $3/D^2$ and the dislocation density (ρ_S) due to strain broadening is $4\varepsilon^2/b^2$ where D is the crystallite size, $\langle\varepsilon^2\rangle^{0.5}$ is the mean square strain and *b* is the burgers vector. Herein, the crystallite size (D) obtained from the mWH analysis [Eqn. (2.30)] and $\langle\varepsilon^2\rangle^{0.5}$, average mean square strain measured at a column length of surface weighted size (D_{eff}) obtained from Warren Averbach method [Eqn.(2.28)] are used. The variation of *D* and $\langle\varepsilon^2\rangle^{0.5}$ with ageing are discussed in § 4.4 & § 4.6.2. The average dislocation density ρ is given by $(\rho_D * \rho_S)^{0.5}$. The average dislocation density (ρ) is determined for all samples and it changes with ageing between 1.07E15 and 3.49E15 (m^{-2}).

In § 4.5, the observed behaviour of microstrain α and α_S with ageing suggests that, the difference $\Delta\alpha_d = (\alpha_S - \alpha)$ shows dominant dislocation effects. The difference $\Delta\alpha_d$ has been plotted with respect to dislocation density in Fig. 4.13. The figure also shows the linear fit obtained between these two parameters with 95% upper and lower confidence limits to the fit.

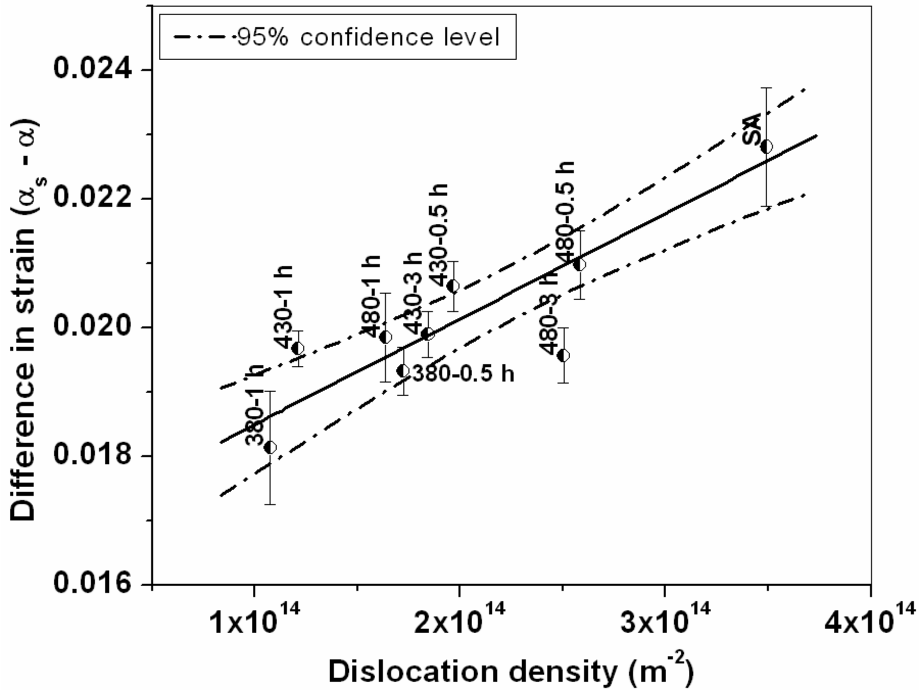

Fig. 4.13 The variation of differences in the microstrain (α_S- α)of Stephens model and mWH method with respect to dislocation density

4.9 Comparison of P_1 with dislocation density (ρ)

The variation of the parameter P_1 as a function of ageing duration for the temperatures 380, 430 and 480 °C is shown in Fig. 4.14 as solid squares (black), circles (red) and triangles (blue) respectively. It is clear from the figure that the parameter P_1 decreases on ageing up to 1 h for all three isothermal conditions. Since precipitation causes an increase in microstrain due to ageing (as shown in § 4.7), the observed decrease in the value of the parameter P_1 has been analyzed based on its dependency with dislocation density. It is well known that the strain fields of dislocations decay as a function of 1/L. The variation of average dislocation density (ρ) as a function of ageing duration is shown in Fig. 4.14 with open symbols for different ageing temperatures. The variation of parameters P_1 and dislocation density, ρ with ageing shows similar behaviour which is in accordance with the 1/L dependency of mean squared strain $\langle \varepsilon^2(L) \rangle$ due to dislocations [**98**].

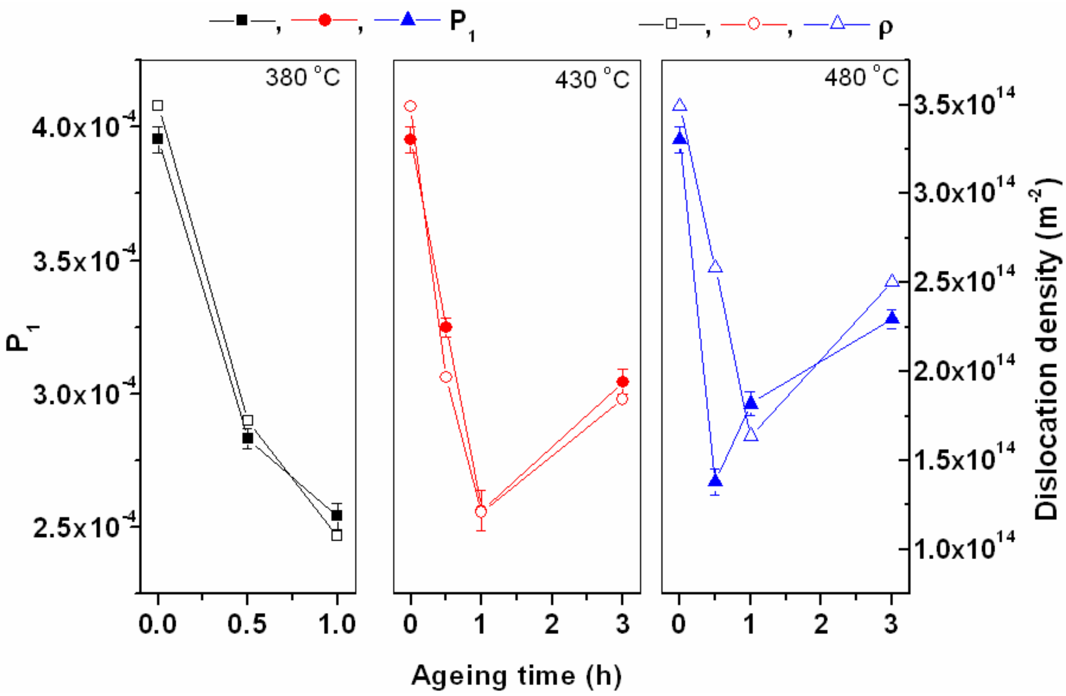

Fig. 4.14 The variations of parameter P_1 obtained from column length distribution of strain using Fourier method and dislocation density ρ determined from Williamson-Smallman approach.

4.10 Summary

- The variation in microstrain (α′) from mWH method [based on Eqn. (2.31)] show similar trend to that of microstrain (α_S) with dominant dislocation induced effects at initial ageing and above 0.5 h ageing, show dominant precipitate induced effects till peak ageing.

- The difference in behaviour of microstrain α with α′ and α_S is $\Delta\alpha_d = (\alpha_S - \alpha)$ which shows a linear correlation with dislocation density (ρ).
- The dependency of microstrain with a new expression which consists long range (P_0) and short range (P_1) strain fields along with second order term is proposed.
- The term P_0, estimated from strain as a function of column length, indicates the long range strain fields and is correlated with the strain determined from the mWH method (using Eq. (4) with FWHM). This strain is attributed to precipitate induced effects.
- The term P_1, which is linked to the 1/L dependency of strain as a function of column length, shows a good correlation with variation in dislocation density.
- The difference in microstrain ($\Delta\alpha_d$) between strain estimated by Stephens model and mWH method shows a linear behaviour with dislocation density.
- The above analysis clearly shows that line profile analysis using various methods can be effectively used to distinguish the precipitation and dislocation induced changes that take place simultaneously during ageing of 17-4 PH steel.
- In order to validate the above approach, it would be beneficial to study precipitation and strain hardening behaviour of different materials using different XRDLPA methods.

Chapter 5

5 Comparison of precipitation kinetics in 304HCu steel using hardness and electrical conductivity under different prior cold working conditions

In this chapter, hardness and electrical conductivity measurements of isothermally aged (at 650 °C, 923 K) 304HCu steel which are prior cold worked at 10 and 20% reduction in thickness are presented. The variation in hardness and conductivity with isothermal ageing are analysed using Johnson-Mehl-Avrami equation. A comparison of the results obtained by the two approaches would be made. Finally, the observed change in precipitate kinetics due to deformation is analyzed to evaluate an equivalent change in activation energy which is attributed to an equivalent of increase in ageing temperature.

5.1 Hardness measurements

5.1.1 Influence of cold work on hardness

The variation in hardness with cold work is shown in Fig. 5.1. The legend SA+CW indicates solution annealed followed by cold worked (CW) samples. The legend 0.25 h and 3 h indicates the duration of ageing carried out at 650 °C on SA+CW samples. In Fig. 5.1, the hardness of solution annealed sample increases from ~ 148 VHN to 245 and 285 VHN with 10% and 20% cold deformation respectively. The change in hardness is attributed to deformation induced strengthening. Shintani and Murata [**126**] reported an increase in hardness by ~ 160 VHN for a cold work of 20% reduction in thickness in 304 stainless steel and attributed the change in hardness due to increase in yield stress. It is well known that the hardness increases with ageing due to thermal induced precipitation [**55**]. In Fig. 5.1 at 3 h ageing duration, the observed increase in hardness is smaller for un-deformed (SA) sample as compared with prior deformed (SA+10CW & SA+20CW) samples. The influence of prior cold work on the variation in hardness during isothermal ageing at 650 °C is discussed in following sections.

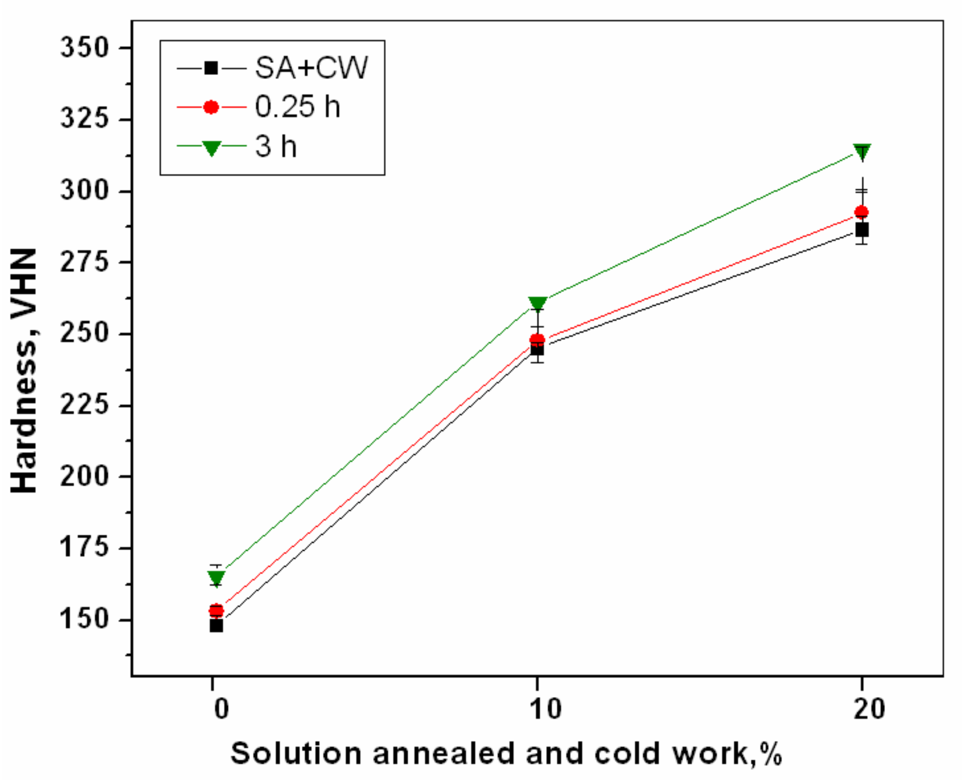

Fig. 5.1 Variation of hardness with prior cold working followed by ageing at 0.25 and 3 h durations

5.1.2 Variation in hardness of solution annealed samples during ageing

The variation in hardness of solution annealed sample with ageing time at 650 °C is shown in Fig. 5.2. In Fig. 5.2, the continuous line is an exponential growth fit to describe the variation in hardness. During initial ageing, the hardness increases rapidly from 148 VHN, after 5 h ageing duration it reaches a peak value of 177 VHN and on further ageing it gets saturated. The change in hardness is ~ 30 VHN during ageing which is mainly attributed due to precipitate induced strengthening. The fine precipitate particles that are formed during ageing at 650 °C are Cu-rich phase, chromium rich carbides ($M_{23}C_6$) and niobium rich carbonitrides (MX) phases which are responsible in increasing the strengthening of the matrix. Ren et al. [**66**] have attributed the strengthening from precipitation of Cu phase in 304HCu austenitic steel. Jiang et al. [**127**] discussed about the strengthening mechanism in 304HCu steel to the Cu-rich phase, $M_{23}C_6$ and MX type precipitates to the total strengtheing. In the study, they attributed that at least 60% of yield strength results from the nano-size Cu-rich precipitate phase. Haung et al. [**65**] reported the change in hardness during creep at 650 °C and 195 MPa reaches peak value after 500 h and retained the high value till rupture. The TEM images of 304HCu steel samples aged for 500 h duration at 650 °C revealed the presence of Cu-rich, $M_{23}C_6$ and Nb(C,N) precipitates which was analysed by Wang et al. [**128**]. These precipitates were very fine and scattered which were attributed to precipitation strengthening and resulted in a change in hardness of 34 HB from the as-received condition by (from 157 HB to 191 HB) ageing for 500 h [**128**]. Thus, the change in hardness is directly related to the kinetics of precipitation.

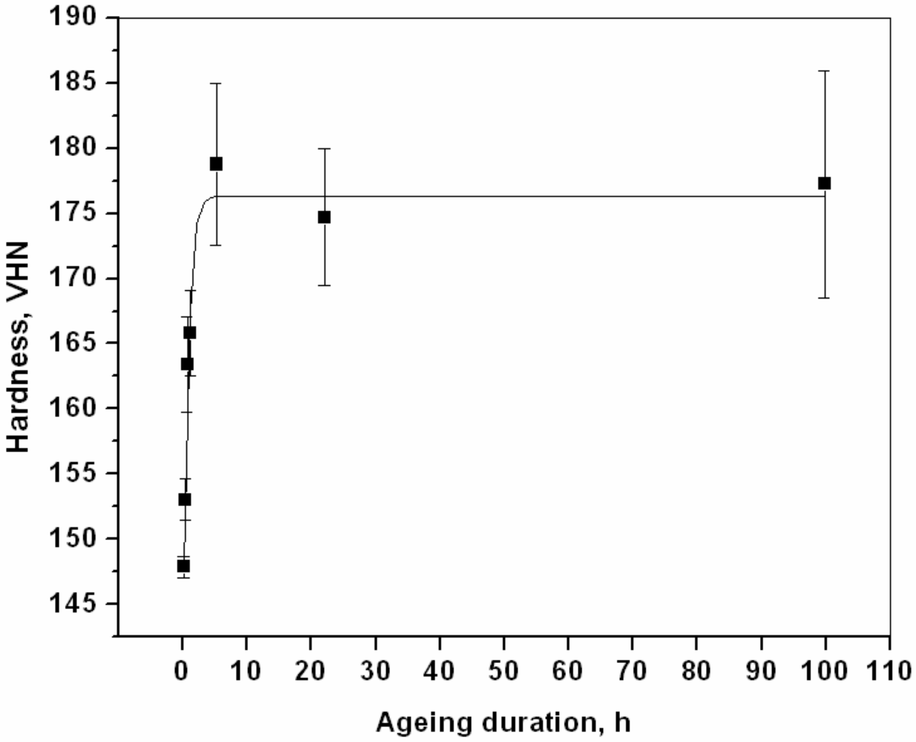

Fig. 5.2 The variation of hardness of solution annealed sample with ageing duration

5.1.3 Variation in hardness of cold worked samples during ageing

The variations in hardness with ageing of SA samples, SA followed by 10% (SA+10CW) and 20% (SA+20CW) prior deformation are shown as square, circle, triangle in Fig. 5.3. Fig. 5.3 shows the increase in hardness of 10% and 20% CW samples which peaks at 5 and 3 h ageing duration to a value of 268 and 314 VHN respectively. The increase in hardness due to ageing is ~ 30 VHN for all the three different initial conditions which is attributed to precipitation strengthening. The observed change in hardness of solution annealed sample due to ageing is lesser than the change observed in hardness due to 10% deformation. In 10% deformed samples (red), during initial ageing from 0-1 h, the hardness changes slowly and on further ageing, the hardness increases rapidly to a peak value of 268 HV at above 5 h of ageing time after which the change in hardness is minimal. On the other hand, in 20% cold work samples the hardness increases rapidly and peaks at ~ 3 h, which is much faster than SA and 10% cold worked samples. The early peaking of hardness in prior cold worked samples during ageing treatment is attributed to formation of additional deformation induced precipitates. The age-hardening behaviour in Ni-martensitic stainless steel revealed early peaking of hardness due to increased precipitation rate under the influence of prior cold working [**129**].

In 20% cold work samples, the hardness decreases at higher ageing times of 22 h and 100 h which is associated with annihilation of dislocations. Similarly, the reduction in hardness with ageing in both un-deformed and prior deformed conditions is observed after reaching peak hardness in Ni-martensitic stainless steel [**129**], The decrease in hardness was addressed due to coarsening of precipitation, dislocation annihilation and formation of reverted austenitic phase. In this study it is observed that, the defects that are formed during deformation acts as favorable nucleation sites for precipitates and it enhances the precipitate strengthening during ageing.

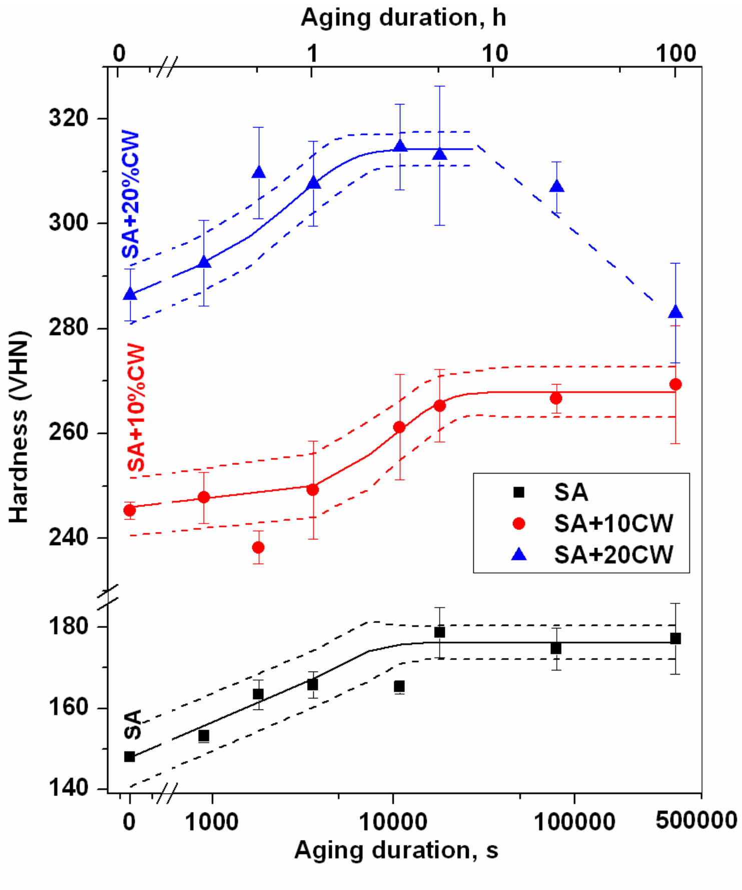

Fig. 5.3 The variation of hardness for SA, SA+10% and SA+20% cold worked 304HCu steel samples with ageing duration

5.1.4 Precipitate kinetics based on hardness measurements

The change in hardness with ageing is fitted with Johnson–Mehl–Avrami (JMA) equation [Eqn. (2.43)] in order to study the kinetics of precipitation in 304HCu steel, under various initial conditions (SA, SA+%CW). The solid line in Fig. 5.3 represents the JMA fit to hardness variation and the scatter in hardness values is within the confidence band of 90 %, as shown by dotted lines in Fig. 5.3. The reaction rate constant (k) and Avrami exponent (n) determined from the fit represents the total change in volume fraction of all kind of precipitates that takes place and the values *k* and *n* determined for three different initial conditions are given in Table 5.1. The reaction rate from hardness measurements lies in the range of 1.12E-4 to 3.70E-4 in all initial conditions. The errors in reaction rate constant are one order less and the results would be discussed in § 5.3. In the present dissertation, the hardness measurements are influenced by total volume change of all kind of precipitates that occur during ageing. However, in earlier study the strengthening from Cu-rich phase has shown the maximum contribution (~60%) towards total yield strength [**127**] and hence the changes in hardness can be attributed to precipitation of Cu-rich phase alone. The earlier studies showed the change in hardness during ageing was able to characterize the kinetics of precipitation [**47**,**48**].

In Table 5.1, the decrease in k value for 10% CW samples from hardness measurements is attributed to the combined effect of annihilation and precipitation. However, in the 20% CW samples, the precipitation behaviour dominates to cause an increase in reaction rate. This behaviour is clearly seen in Fig. 5.3. Thus, the accelerated precipitation process based on pipe diffusion mechanism [**81**] along dislocations enhances the hardness changes. The Avrami exponent (*n*) estimated lies in the range of 1-1.3 for SA and cold worked samples, indicating that the kinetics is due to growth of the precipitates of appreciable initial volume [**130**].

Table 5.1 The reaction rate constant and Avrami exponent obtained from Eqn. (2.43) based on electrical conductivity and hardness values are given below.

Cold work (%)	**JMA fit to hardness**		**JMA fit to electrical conductivity**	
	Reaction rate constant (k, s^{-1})	Avrami Exponent (n)	Reaction rate constant (k, s^{-1})	Avrami Exponent (n)
0	3.13E-4	1.16±0.27	7.66E-5	1.17±0.05
10	1.12E-4	1.25±0.27	8.42E-5	0.72±0.10
20	3.70E-4	1.28±0.15	1.33E-4	0.70±0.17

5.2 Electrical conductivity measurements

5.2.1 Influence of cold work on electrical conductivity

The variations in electrical conductivity with cold work for un-aged, 0.25, 1 and 5 h samples are shown in Fig. 5.4. The variation in conductivity with cold work (of un-aged samples) is minimal. The defects that are introduced in the matrix during deformation are mostly line defects such as dislocations, which has scattered the electron flow causing decrease in conductivity. The observed decrease in conductivity due to 20% cold deformation is ~ 5 X 10^3 S/m. However, in all aged samples, the conductivity of 20% prior cold work shows higher value as compared with un-deformed and aged samples. In Fig. 5.4, it is observed that the change in conductivity with cold work for 1 h aged samples is high. On ageing for 5 h duration, the change in conductivity with cold work reduces leading to saturation. The influence of conductivity on further ageing is discussed in following section.

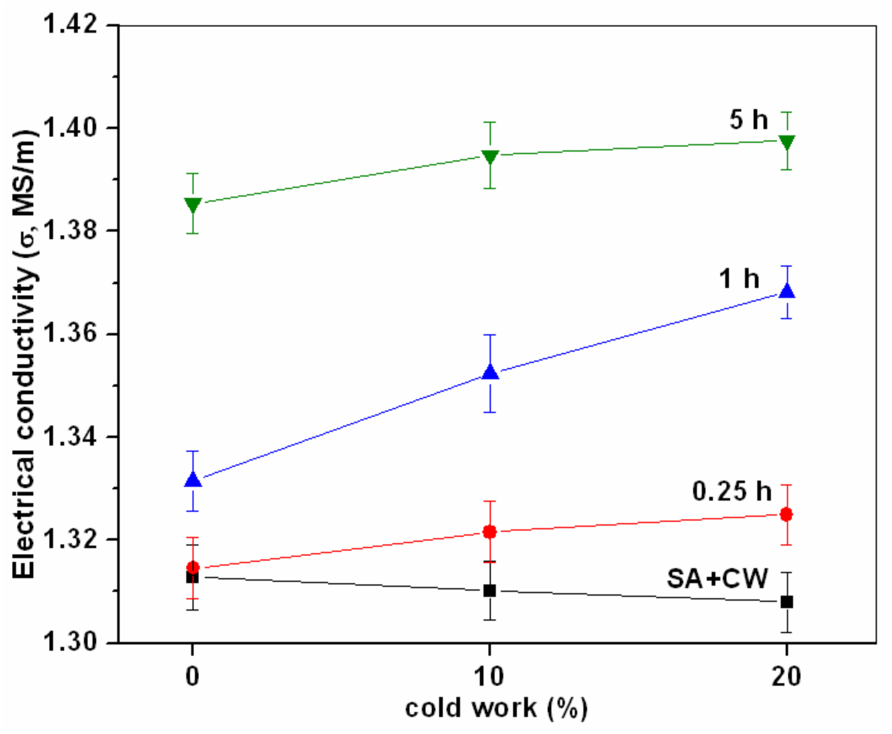

Fig. 5.4 The variation of electrical conductivity with cold work for un-aged, 0.25, 1 and 5 h aged samples.

5.2.2 *Variation in electrical conductivity with ageing of SA and cold worked samples*

The change in electrical conductivity of SA and cold worked samples with ageing duration is shown as hollow symbols of square (black), circle (red) and triangle (blue) in Fig. 5.5. In Fig. 5.5, it can be observed that on isothermal ageing of SA and cold worked samples, the conductivity has increased by ~90 X 10^3 S/m and reaches saturation above 10 h of ageing. The increase in conductivity with ageing duration is attributed to decrease in scattering effect as a result of precipitation/clustering of solute atoms. In § 5.2.1, the change in conductivity due to cold working alone is minimal in contrast to that observed during ageing treatment. These findings reveal that, the response of conductivity for different type of defects like dislocations and solute atoms is different. Thus, it is inferred that conductivity increases with ageing time in 304HCu steel which is significantly influenced by precipitation. However, Ren et al. [**66**] suggested that the change in electrical resistivity is influenced by three different factors such as reduction in scattering caused by Cu-solute atoms, reduction in defects during ageing and thirdly, the formation of Cu-precipitates which has lower conductivity than austenitic phase.

5.2.3 Precipitate kinetics based on electrical conductivity

The variation in electrical conductivity is directly related to the total precipitation process. Hence, the Johnson–Mehl–Avrami (JMA) equation is fitted to the conductivity variations observed during ageing of solution annealed and SA+10% and 20% cold worked for studying the kinetics of precipitation. The JMA fitted to the conductivity variation is shown as solid line in Fig. 5.5. It is clear from Fig. 5.5 that, the change in conductivity with ageing time is much faster for 20% cold work sample as compared to both SA as well as 10% cold worked samples. Viswanathan et al. [**56**] studied precipitation kinetics at 395, 455 and 352 °C with the help of resistivity measurements and observed a rapid change in resistivity at higher temperature. Thus, the increase in rate of precipitation due to deformation is able to correlate with that of changes due to ageing temperature.

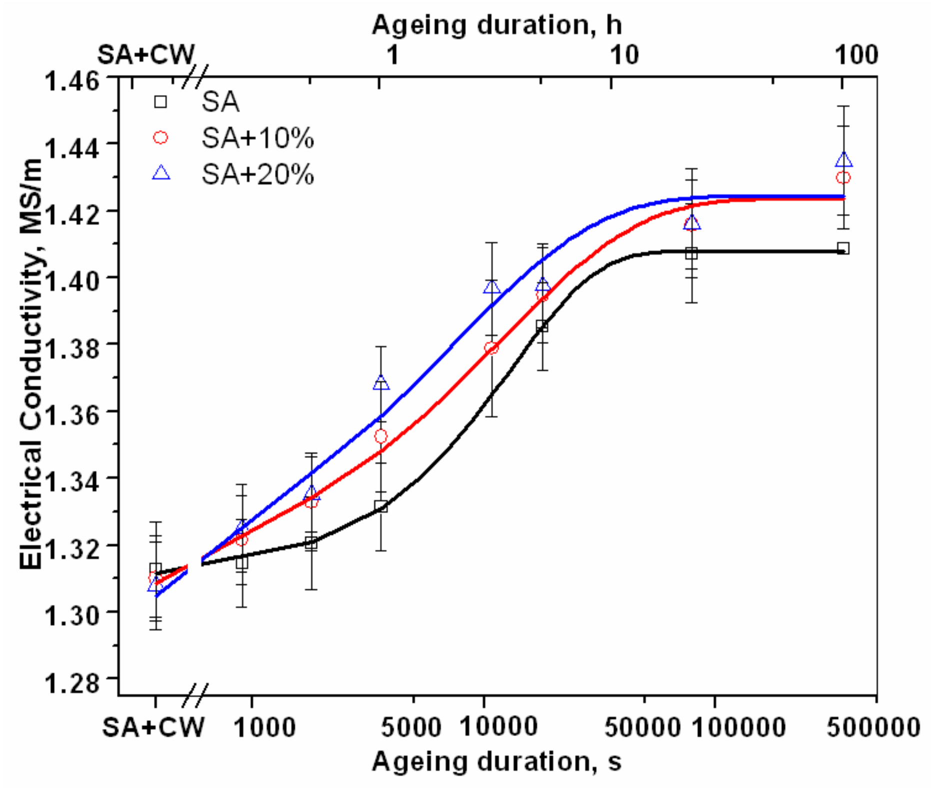

Fig. 5.5 The variation of electrical conductivity of solution annealed followed by cold worked samples with respect to ageing duration. The solid line indicates the JMA fit

The reaction rate constant (*k*) and Avrami exponent (*n*) obtained from electrical conductivity are also shown in Table 5.1. From Table 5.1, it is seen that the reaction rate constant (*k*) increases with cold work, indicating accelerated precipitation kinetics. The Avrami exponent (*n*) determined from hardness and conductivity of SA sample is 1.16 and 1.17 respectively, the value of *n* indicates growth of precipitates with appreciable initial volume. The decrease in *n*-value from 1.17 to 0.7 on cold working can be attributed to precipitation on dislocations [**130**] as well as dislocation pinning by C or N atoms to form Cottrell atmosphere. In 347 grade austenitic steel, the strain-induced defects in the matrix (due to cold work) resulted in early formation of precipitates is mainly along the deformation bands [**82**]. Zhou et al. [**131**] while considering $M_{23}C_6$ precipitates in 304H steel estimated rate constant (k) for ageing temperature of 650 °C to 800 °C was 0.002 to

0.105 (h^{-1}) which is equal to 5.55E-7 to 3.33E-5 (s^{-1}) respectively. Wang et al. [**128**] measured the $M_{23}C_6$ precipitation rate value as 0.554 (h^{-1}) or 1.54E-4 (s^{-1}) in 304HCu steel aged at 650 °C. In these studies, the volume fraction of $M_{23}C_6$ was calculated from SEM micrographs using which the precipitation kinetics was determined. The reaction rate observed in the present study lies in the range of 7.66E-5 to 3.70E-4 from both hardness and electrical conductivity measurements in all initial conditions. Thus, the k value is of the same order of reaction rate as observed in earlier studies.

5.2.4 Analysis of variation of reaction constant due to deformation

The observed variation in reaction rate constant estimated based on variation in conductivity is analyzed further. In general, cold deformation stores some part of the strain-induced energy in the matrix which alters the activation energy of precipitation and in turn changes the reaction rate. Dutta et al. [**81**] reported that deformation causes lowering of activation energy for precipitation on dislocation and increases the nucleation rate. The dependency of reaction rate constant (k) upon the activation energy and ageing temperature is given by Arrhenius equation [Eqn. (2.44)] and the logarithm form of Eqn. (2.44) is written as

$$ln(k) = \frac{-E_a}{RT} + ln(k_0) \qquad \cdots \qquad (5.1)$$

where k_0 is a constant for a given material, E_a is the activation energy, R is the gas constant, and T is the absolute temperature. For a particular system if the initial microstructure is un-altered, the reaction rate constant is dependent on ageing temperature. If the initial microstructure is changed due to cold work, the apparent activation energy will be changed to E_a^c, which would modify Eqn. (5.1). Assuming that changes in k_0 due to cold working is minimal, the difference in activation energy ($\Delta E_a = E_a^c - E_a$) can be obtained as

$$(E_a^c - E_a) = RT[ln(k) - ln(k^c)] \qquad \cdots \qquad (5.2)$$

where k^c represents reaction rate constant for cold worked samples. The reaction rate constants (k) obtained based on conductivity measurements are considered in Eqn. (5.2) and the change in activation energy (ΔE_a) due to 10% and 20% cold deformation is calculated as 0.73 kJ/mol and 4.225 kJ/mol respectively for an ageing temperature of 650 °C.

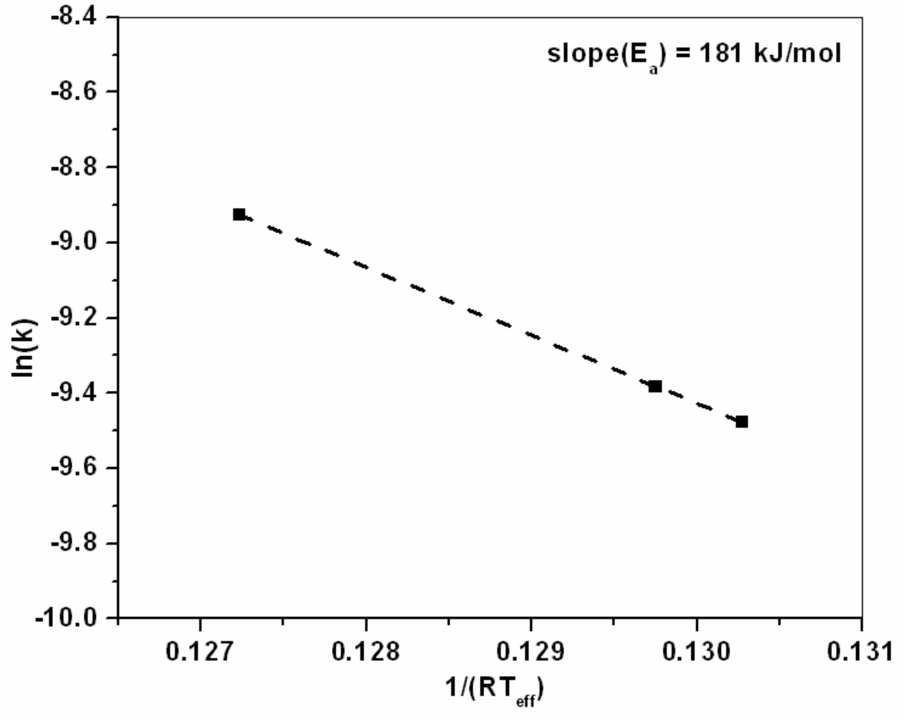

Fig. 5.6 The variation of ln(k) with equivalent thermal energy (RT_{eff}) by using an activation energy of 181 kJ/mol

The earlier study of precipitation kinetics in 304HCu steel revealed that the reaction rate increases with increase in ageing temperature from 600 to 800 °C. Thus, it would be worthwhile to consider the observed changes in precipitation kinetics due to cold work with an equivalent thermal energy (RT_{eff}). Towards this objective, activation energy of 181 kJ/mol for Cu precipitation in austenitic steels as reported by Ren et al. [**132**] is considered. Using this value of activation energy and k value obtained for solution annealed sample, $\ln(k_o)$ is determined from Eqn. (5.1). Assuming that k_o and E_a for precipitation remains unchanged due to cold working, an equivalent temperature is estimated for the 10% and 20% coldworked samples using the k value obtained in these conditions. Fig. 5.6 shows the variation of $1/\ RT_{eff}$ with $\ln(k)$ and the line corresponding to a slope of 181 kJ/mol. The temperatures thus obtained are 654 °C and 672 °C for 10% and 20% CW samples.

However, in this steel, MX and $M_{23}C_6$ type carbides form during ageing. The activation energy of MX precipitates is 294 kJ/mol [**133**] and $M_{23}C_6$ precipitate (calculated from the reaction rate constants given in Table 5 of Ref. [**131**]) is 209 kJ/mol. Considering the activation energy of MX and $M_{23}C_6$ precipitates along with Cu precipitate, the effective temperature lies between 652- 654 °C and 664-672 °C for 10% and 20% CW samples respectively. It is well known that hardness and conductivity are influenced by the different precipitate phases which form in 304HCu steel. The effects of individual phase evolution can also be studied by using the multiphase KJMA model in computational thermodynamic software or experimentally by observing the evolution of these phases by suitable imaging techniques [**134**].

5.3 Comparison of electrical conductivity and hardness

The results presented in § 5.1and § 5.2 clearly indicate that the increase in hardness (H) and conductivity (σ) with ageing time for SA and cold worked samples is associated with precipitation from solid solution. However, the variation in hardness and conductivity show different features with prior cold work. An increase in hardness by 50% is observed at 40, 130 and 33 min of ageing time for SA, 10% and 20% cold worked samples respectively.

The higher ageing time required to attain 50% peak hardness for SA+10%CW sample is attributed to the simultaneous precipitation (which would increase the hardness) and annihilation of dislocations (which would reduce the hardness). This is also corroborated by the fact that, hardness changes are minimal during initial ageing up to 1 h duration for 10% CW samples.

On the other hand, the conductivity increases by 50% at ~ 170, 130 and 80 min for SA, 10% and 20% cold worked samples respectively. The reduction in time for an increase in conductivity by 50% is attributed to accelerated precipitation due to pre-existing dislocations. Further it should be noted that conductivity changes were found to be insensitive to initial cold work as discussed in § 5.2. The observed increase in hardness and conductivity by 50% in solution annealed samples at ~40 and 170 min respectively shows the differing sensitivity of these properties to precipitation. Similar behaviour is reported by Vasudevan et al. [**50**], in their study the peaking of hardness occurred at an earlier ageing duration as compared to the minimum in resistivity observed at later ageing times in T-250 grade maraging steel on ageing at different temperatures.

From Table 5.1, an increase in reaction rate constant (*k*) (estimated from conductivity) with cold work indicates increase in the rate of precipitation. The reaction rate estimated from hardness for SA+10%CW is 1.12E-4, which is lower than that obtained for SA and SA+20%CW samples. This reduction is attributed to the sensitivity of hardness to simultaneous precipitation and annihilation of dislocations causing the hardness to change slowly during initial ageing. The Avrami exponent (*n*) 0.72, 0.70 for SA+10%CW and SA+20%CW samples obtained from electrical conductivity is attributed to precipitation on dislocations. However, the variation in Avrami exponent from 1.16 to 1.28 obtained through hardness measurements is attributed to the combined influence of precipitation and annihilation of pre-existing dislocations. In contrast, the lower *n* values obtained from electrical conductivity indicates insensitivity of conductivity variation to dislocation annihilation during ageing. Hence, in order to explain the change in precipitation kinetics due to deformation, the electrical conductivity based measurements are considered to determine an equivalent change in activation energy as well as to determine an equivalent of increase in temperature as presented in § 5.2.4.

5.4 Summary

- Ageing induced precipitation causes increase in hardness and conductivity in SA and SA followed by cold worked samples.
- The study reveals that the variation in conductivity due to deformation induced dislocations is minimal.
- The peaking of hardness was observed at earlier durations as compared to that of conductivity with ageing time.
- The ageing behaviour of cold worked 304HCu steel has been studied by using electrical conductivity and hardness measurements. Further, the JMA equation is used to characterize the precipitation kinetics based on hardness and electrical conductivity measurements.
- The study reveals that the increase in reaction rate, *k* with cold work as determined from conductivity measurements, indicates an increase in rate of precipitation. The deformation induced precipitation process enhances the changes in electrical conductivity and hardness.

- The enhanced changes in electrical conductivity and hardness are consequences of lower activation energy for precipitation on dislocations. The apparent change in activation energy in overall system is calculated as 0.73 and 4.225 kJ/mol due to 10% and 20% cold deformation.
- The change in rate of precipitation due to 10% and 20% deformation is attributed to an equivalent ageing temperature of 654 and 672 °C, respectively.

Chapter 6

6 Influence of prior deformation on isothermal ageing behaviour of 304HCu steel by XRD analysis

In this chapter, the analysis of XRD peak profiles of prior deformed 304HCu steel samples followed by isothermal ageing at 650 °C, (923 K) for various durations up to 100 h is presented. The synchrotron source is able to reveal the formation of very fine precipitates during thermal ageing. The variation in lattice parameter is studied to understand the influence of deformation on precipitation. The effect of simultaneous precipitation and dislocation annihilation on changes in microstrain that occur during isothermal ageing is studied. The microstrain is determined using modified Williamson Hall and Warren Averbach approach. The microstrain estimated from XRD line profile analysis (XRDLPA) is used to explain the observed changes in dislocation density. The parameter P_1 determined from the analysis of mean squared strain $\langle \varepsilon^2(L) \rangle$ as a function of column length L which is discussed in chapter 4 is used to study the influence of pre-existing dislocations on precipitation behaviour. Finally, a comparison of the results obtained from XRDLPA with hardness and electrical conductivity is made.

6.1 XRD line profiles of 304HCu steel

The XRD peak profiles from the synchrotron source were obtained for undeformed and prior cold worked 304HCu steel samples with ageing conditions as mentioned in § 3.1. Fig. 6.1 shows the XRD patterns of un-aged SA sample along with 22 h aged samples of SA, SA+10CW and SA+20CW as open circle (green), square (black), circle (red) and triangle (blue) symbols, respectively. In Fig. 6.1, the XRD spectrum is plotted in the reciprocal space ($Q = 2sin\theta/\lambda$) by correcting the back ground intensity with a 5th order polynomial.

The intense peak reflections (111), (200), (220), (311), (222) and (400) represent the austenitic matrix peaks which arise from the FCC structure. The intensity of precipitate peaks of $M_{23}C_6$ and MX carbonitrides are well resolved due to the highly intense synchrotron radiation source. The XRD pattern of SA samples under un-aged condition reveals the pre-existence of precipitate peaks of MX and $M_{23}C_6$. On ageing for 22 h, the growth of precipitate peaks is seen. As discussed in § 5.1.4 & § 5.2.3 the precipitation kinetics of un-deformed samples with ageing shows *n*-values of 1.16 and 1.17. These *n*-values have been attributed to growth of pre-existing particles which is confirmed from the XRD profiles for SA sample. The complete dissolution of MX type precipitates is above 1350 °C which is higher than the melting point of the 304HCu steel. The presence of Nb-rich precipitate particles in 304HCu steel under SA condition was reported by Chi et al. from their SEM investigations [**135**].

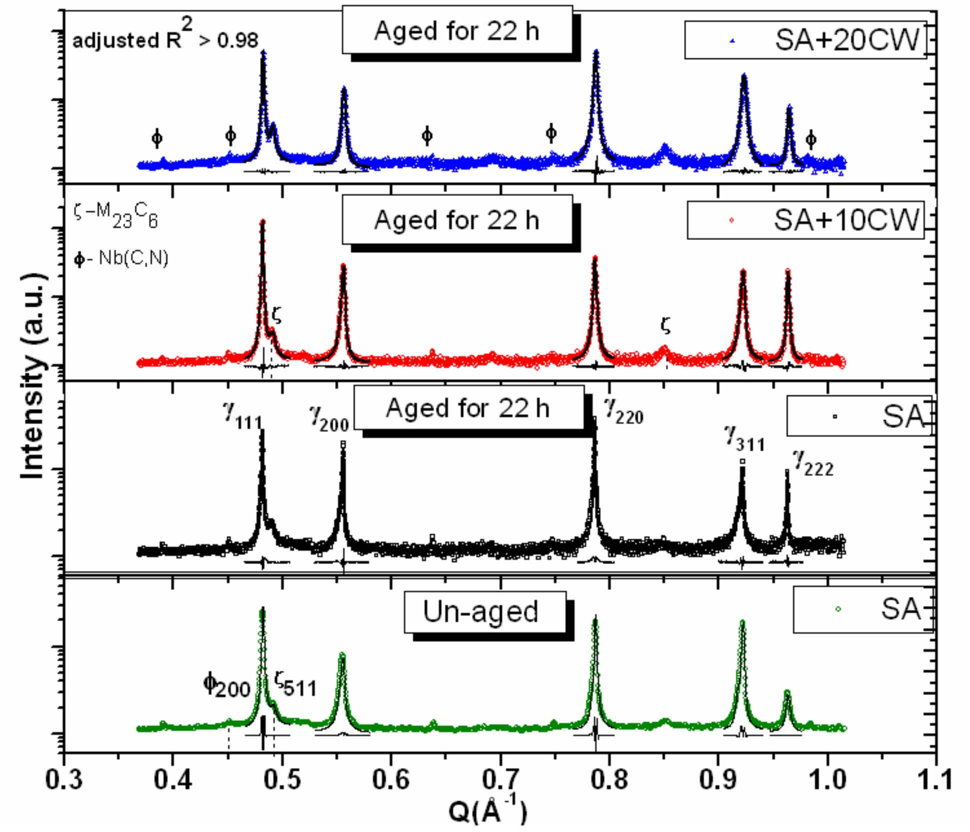

Fig. 6.1 The XRD peak profiles in reciprocal space for un-deformed (SA) and deformed 304HCu steel.

The precipitate peaks in XRD spectrum of aged samples are clearly visible as compared with un-aged samples. In Fig. 6.1, increase in intensity of (511) reflection of $M_{23}C_6$ precipitates (located at the right shoulder of (111) matrix peak) is clearly observed in 22 h aged prior cold worked samples. In addition to $M_{23}C_6$ and MX carbonitrides, the precipitation of Cu-rich phase occurs during ageing. The Cu-rich phase is not identified separately in the XRD pattern of aged samples because the lattice parameter of coherent Cu phase is ~3.604 Å [**136**], is very close to the austenite matrix phase. The pseudo Voigt function is used to fit austenitic phase reflects for profile refinement. The fit along with difference plot is shown by continuous solid line (black) in Fig. 6.1. A double peak profile fitting is carried out to estimate the profile parameters of the (111) matrix peak, in order to separate the $M_{23}C_6$ peak from the shoulder of (111) matrix peak. The adjusted R-square value is above 0.98 for all deformed and aged 304HCu samples.

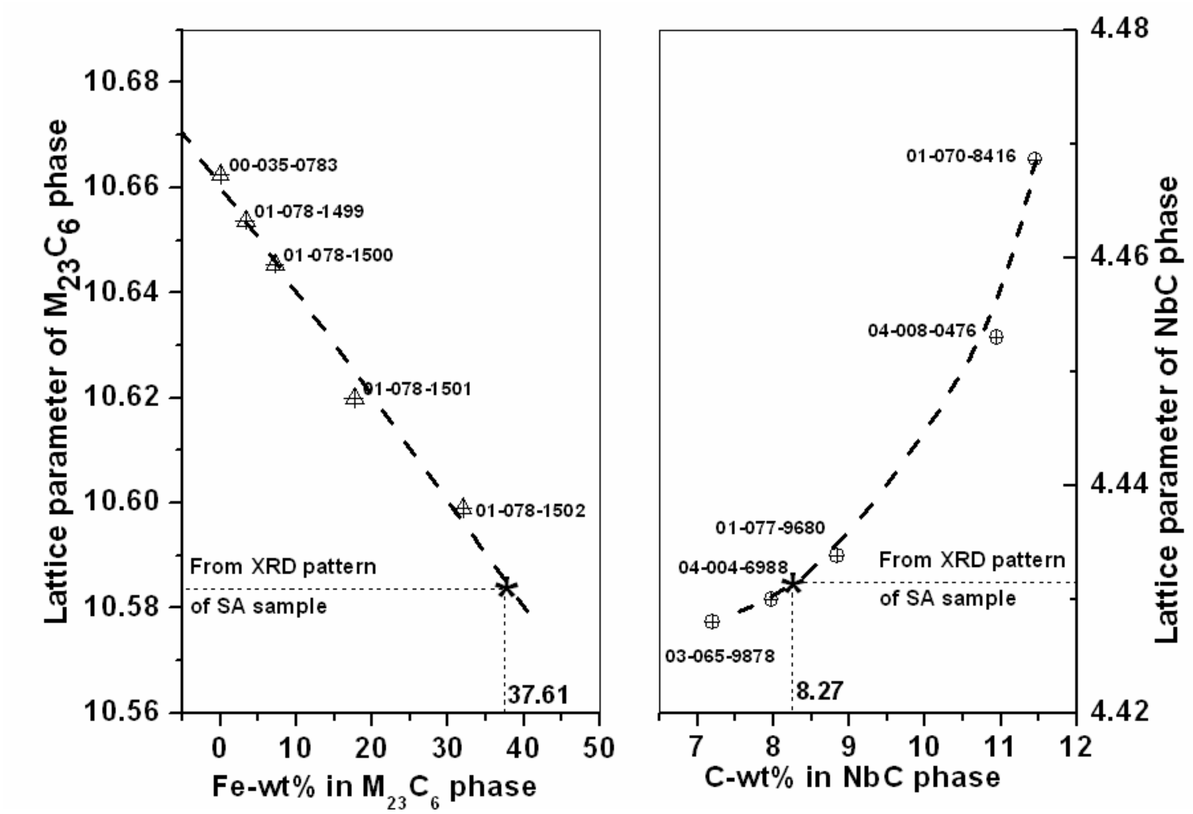

Fig. 6.2 The variation in lattice parameter of $M_{23}C_6$ and NbC phases with Fe and C wt% based on ICDD data respectively (The legends indicate the Powder diffraction file available from ICDD). (units missing in y-axis)

The (511) reflection and (200) reflection of $M_{23}C_6$ and NbC phases are the 100% intensity peaks. The lattice parameter of $M_{23}C_6$ and NbC phases are calculated from the peak position of (511) reflection of $M_{23}C_6$ and (200) reflection of NbC phase. Fig. 6.2 shows the variation in lattice parameter of $M_{23}C_6$ and NbC phases collated from Powder Diffraction Files (PDF) available from International Centre for Diffraction Data – ICDD with varying Fe and C wt% respectively. In Fig. 6.2, the observed variation of lattice parameter of $M_{23}C_6$ with Fe- wt% is linear. However, the variation of lattice parameter of NbC with C wt% is a polynomial which is shown as dashed line in Fig. 6.2. The lattice parameter measured from

XRD pattern of SA 304HCu sample for $M_{23}C_6$ phase is 10.599 Å and NbC is 4.469 Å which is presented in their corresponding fits shown as star symbol. Based on the fit to the ICDD data, the calculated Fe- wt% in $M_{23}C_6$ is ~ 37.6 % and C- wt% in NbC is ~ 8.3 %.

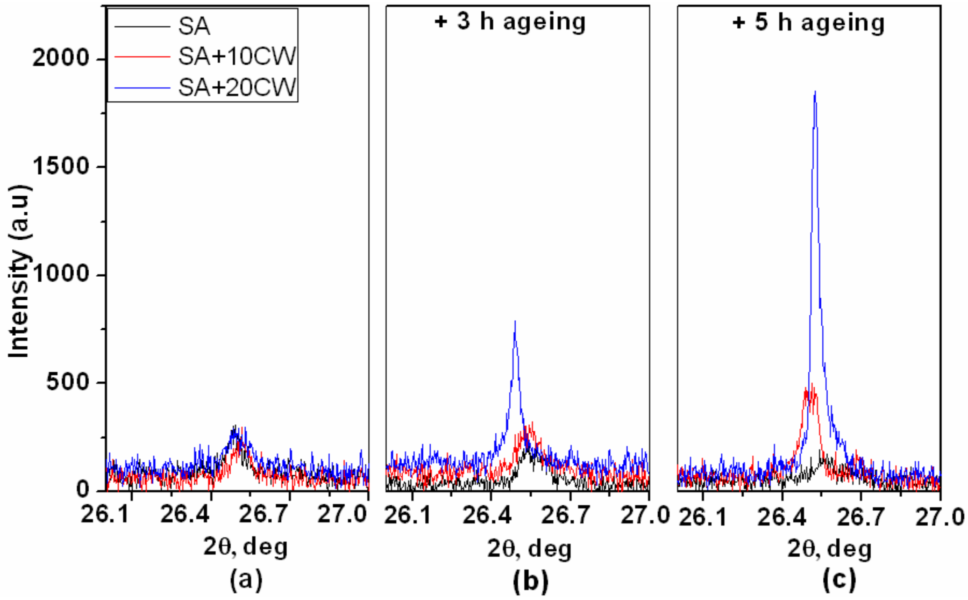

.

Fig. 6.3 The (220) reflection peak of precipitate Nb(C,N) for (a) SA and cold worked samples (b) aged at 3 h and (c) 5 h durations.

Fig. 6.3(a), (b) & (c) show the (220) reflection corresponding to MX phase for un-aged; aged at 3 h and 5 h duration respectively of SA, SA+10% and SA+20% cold worked samples. No significant variation in peak intensity due to cold working is seen in Fig. 6.3(a). In Fig. 6.3(b) & (c), it is observed that on ageing for 3 h and 5 h duration, there is a definite increase in peak intensity of prior cold worked samples. Qualitatively, though the volume fraction of MX phase in these samples is very small, the XRD pattern reveals a notable change in precipitate peak intensities as shown in Fig. 6.3.

6.1.1 Variation in lattice parameter with ageing time

Fig. 6.4 shows the XRD peak profile of the $(420)_\gamma$ reflection corresponding to the 10% and 20% prior cold worked and aged (1, 5 and 100 h) 304HCu steel samples. From Fig. 6.4, it is observed that the peak position of the $(420)_\gamma$ peak reflection shifts towards right side with increase in ageing duration for both the 10% and 20% cold worked samples. The shift in peak position indicates reduction in lattice parameter of the matrix with ageing. Boeuf et al. [**137**] observed that the lattice parameter decreases (increase in peak position) as a function of ageing time, indicating an increase in volume fraction of $M_{23}C_6$ carbide precipitates. Hence the observed right shifting of the $(420)_\gamma$ peak also indicates precipitation of $M_{23}C_6$, Nb(C,N) and Cu phase with ageing time.

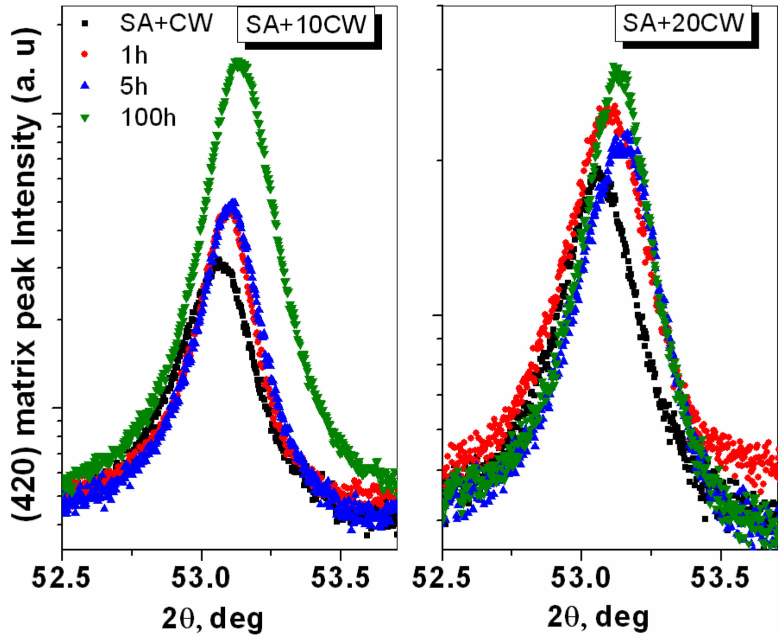

Fig. 6.4 The (420) matrix peaks for 10 % and 20 % cold worked samples aged at 0, 1, 5 and 100 h durations.

The peak position (2θ) of the γ phase reflections (111), (200), (220), (311), and (222) are determined after profile refinement for all the cold worked and aged 304HCu samples. Using the peak positions of these five reflections of γ phase, the lattice parameter is estimated by Nelson-Riley method [**14**]. The variations in lattice parameter of SA, 10% and 20% cold deformed 304HCu samples aged for different durations are shown in Fig. 6.5. From Fig. 6.5, a reduction in lattice parameter with ageing time is observed which is also dependent on the initial condition. The reduction in lattice parameter due to ageing of SA, SA+10CW and SA+20CW samples for 22 h duration is around 0.002, 0.004 and 0.007 Å. The reduction in lattice parameter upon ageing is attributed to the contraction of the matrix due to migration of precipitate forming elements from the matrix. The larger reduction in lattice parameter with ageing time for 10% and 20% cold worked samples as compared with SA samples indicates higher precipitation. The higher precipitation behaviour in deformation modified 304HCu steel is attributed to the dislocation nodes created during deformation acting as nucleation sites for precipitation due to pipe diffusion along dislocations. Ren et al. [**66**] found the footprint of Cu-precipitation in 304HCu steel after 6 h ageing at 700 °C from reduction in the lattice parameter (Δa_{γ}) by 0.0041Å. In this study, the change in lattice parameter due to 10%CW and 20%CW is 0.003 and 0.006 Å for an ageing of 5 h duration respectively.

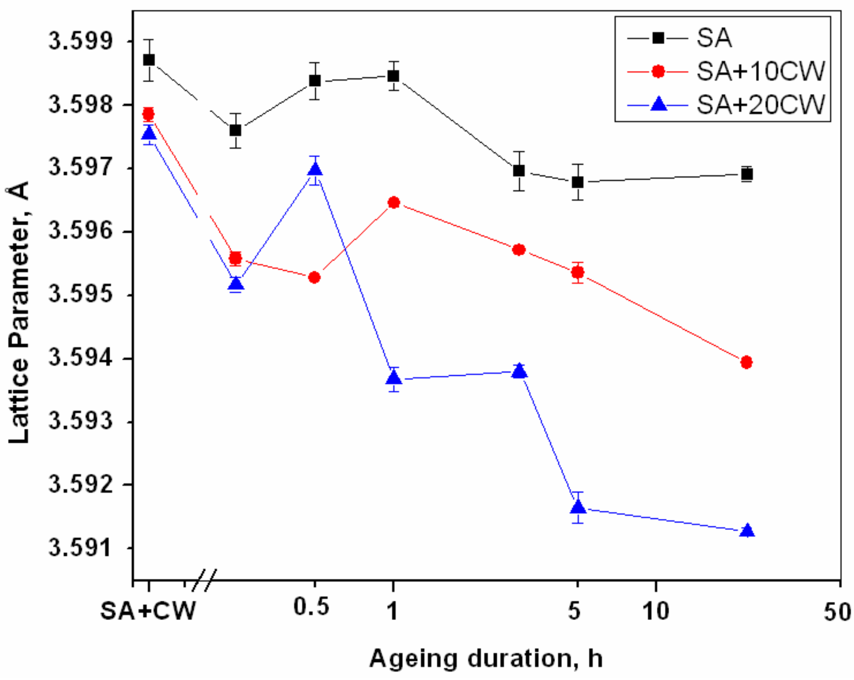

Fig. 6.5 The variations in lattice parameter for SA, SA+10CW and SA+20CW with thermal ageing up to 22 h duration.

From Fig. 6.5, it is clearly seen that the lattice parameter initially decreases followed by an increase after 0.25 h ageing duration for all the three initial conditions. The decrease and increase in the lattice parameter in different materials have been attributed to the compositional change that occurs in the matrix during formation and dissolution of secondary phases [**16**,**17**]. The equilibrium precipitate phase diagram [**138**] of 304HCu steel shows the formation and dissolution of different phases such as Cu-rich phase, sigma, alpha, Cr_2N, $M_{23}C_6$, MX type and other precipitates. Thus, the increase in lattice parameter above 0.25 h can be attributed to the dissolution of sigma and alpha phases in to the matrix and the reduction in lattice parameter with ageing duration are directly related to the formation of Cu-rich phase, $M_{23}C_6$ and MX type precipitates. Rai et al. [**16**] have ascribed the increase in lattice parameter to dissolution of $Ni_2(Cr,Mo)$ and γ'' phases while the decrease in lattice parameter to the formation of δ phase in Inconel 625 superalloy. Khan et al. [**17**] have addressed the decrease in lattice parameter of γ & γ' phases in Ni-based alloy on annealing above 800 °C to depletion of Cr content and also due to the formation of α phase.

6.1.2 Peak broadening with cold working followed by isothermal ageing

The variations in peak broadening with diffraction vector (K) for SA, 10% and 20% cold worked 304HCu samples are shown in Fig. 6.6(a) which indicates anisotropic broadening. It is also observed that the anisotropic broadening increases with cold working. Fig. 6.6(b) & (c) shows the peak broadening of 10% and 20% prior CW and aged (for 0.25 h and 1 h) samples respectively. From Fig. 6.6(b) in 10% CW samples, the peak broadening decreases on ageing up to 1 h duration. In Fig. 6.6(c) for 20% CW samples, the peak broadening increases with highest broadening observed on ageing for 1 h duration. In all deformed samples due to presence of long range internal stresses developed during deformation of crystal structure, the XRD pattern shows asymmetric broadening. The asymmetric broadening observed is minimal within the limit of 0.05° and it has been addressed by a suitable profile fitting function. By using XRD peak profile analysis, the effect due to crystallite size and microstrain are separated from broadening of deformed samples and the material characterization is presented in following sections.

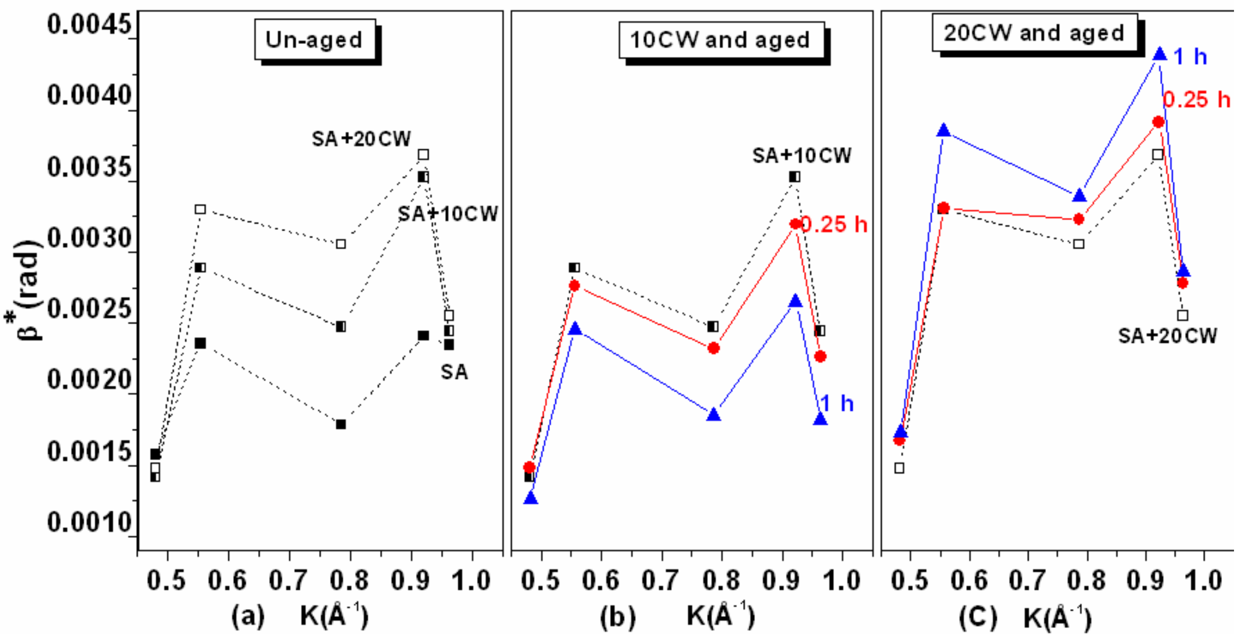

Fig. 6.6. The variation in broadening with diffraction vector (K) for (a) un-aged SA, SA+10CW and SA+20CW (b) SA+10CW followed by 0.25 h and 1 h aged (c) SA+20CW followed by 0.25 h and 1 h aged samples

6.1.3 The dislocation dependent anisotropic strain factor

In Fig. 6.6, the Williamson-Hall (WH) plot shows anisotropic peak broadening and hence to estimate the strain parameter a correction factor known as average contrast factor ($\bar{C}$) is introduced which addresses the dislocations dependent anisotropic strain. The average contrast factor is defined in terms of the $\bar{C}_{h00}$ and q values as given by Eqn. (2.29). Ungar et al. [**110**] have compiled the $\bar{C}_{h00}$ and q values as a function of elastic constants for FCC and BCC crystals containing dislocations. Substituting the elastic constants estimated by Ledbetter [**139**] for 18-8 type austenitic materials, the average $\bar{C}_{h00}$ and q values lies in the range of 0.29 to 0.33 and 1.7 to 2.5 respectively (from ref. [**110**]), depending upon the percentage of edge and screw dislocations present in the material. In the present study, for modified Williamson Hall (mWH) analysis, the average $\bar{C}_{h00}$ is taken as 0.31 by assuming that the material consists of equal amount of edge and screw dislocations.

The q value for all samples is determined from the linear regression of quadratic form of Eqn. (2.30) which is given by Eqn. (6.1):

$$[(\beta^*)^2 - (1/D)^2]/\mathrm{K}^2 \approx \alpha^2 \bar{C}_{h00}(1 - qH^2) \quad \cdots \qquad (6.1)$$

The q value increases for SA+10CW to SA+20CW from 2.35 to 2.54. The q-values of the aged samples vary in a range of 2.15 to 2.65 indicating a change in the character of dislocations. Further analysis of the change in character of dislocation is not carried out in this study. Shintani and Murata [**126**] have attributed the change in q-value with cold work to the change in dislocation character from screw to edge dislocations.

6.2 Modified Williamson Hall method

The anisotropic peak broadening caused by dislocation contrast is accounted by using modified Williamson Hall method. The mWH plots of SA, SA+10CW and SA+20CW specimens aged for 22 h are shown in Fig. 6.7. The slope of the linear mWH plot obtained by accounting for the average contrast factor reveals that the normalized mean square strain or microstrain (α) in SA sample is much lower than that in SA+10CW and SA+20CW 304HCu samples.

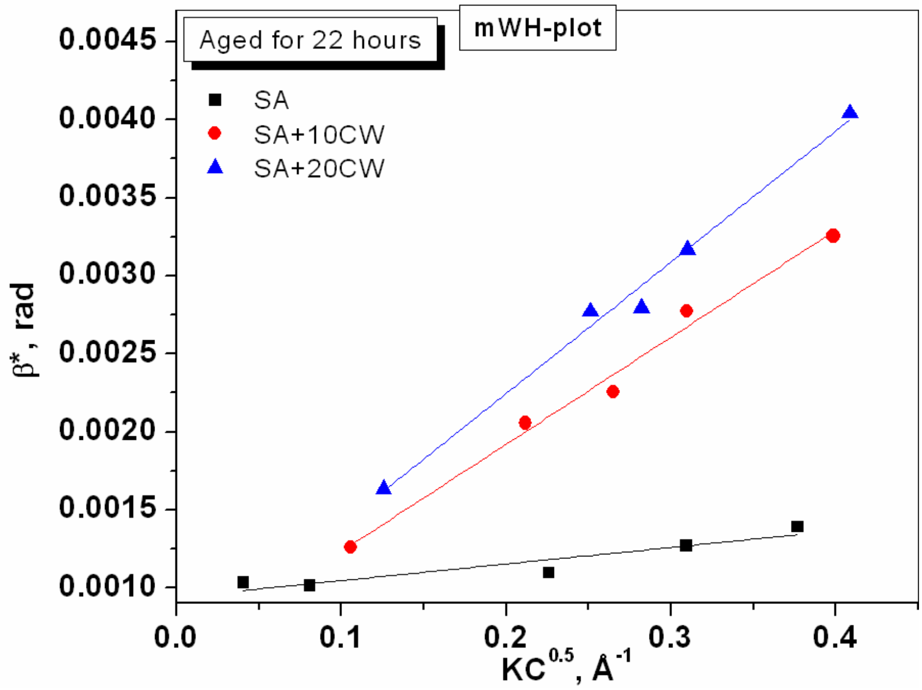

Fig. 6.7 The mWH plot of SA, SA+10CW and SA+20CW 304HCu samples aged for 22 h duration.

6.2.1 Dislocation induced microstrain of cold worked samples

The variation in microstrain (α) determined from mWH method of un-aged 304HCu steel samples with cold working is shown in Fig. 6.8. The deformation induced dislocations have introduced lattice distortion in the matrix due to 10% cold work which causes increase in microstrain ~ 0.006 as shown in Fig. 6.8. However, an additional deformation from 10% to 20% CW has introduced a change in α from 0.007 to 0.0085. The deformation which causes increase in microstrain also influences the strengthening with an increase in hardness by ~100 VHN and ~140 VHN due to 10% and 20% cold work. It is also observed that the strengthening due to cold deformation is linear with the microstrain (α).

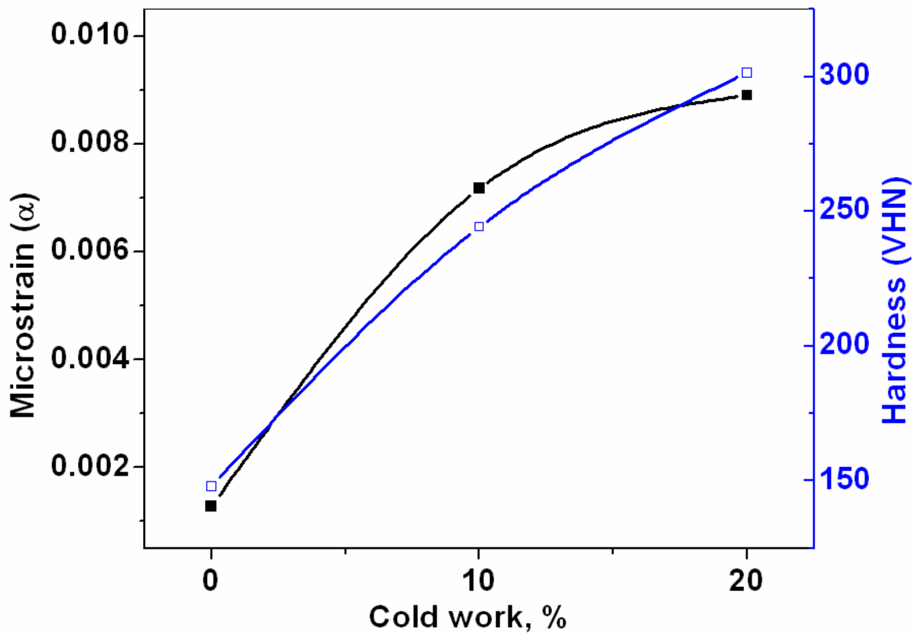

Fig. 6.8 The variation of microstrain (α) with cold work of un-aged 304HCu steel.

6.2.2 Microstrain changes on ageing

Fig. 6.9(a)-(c) show the variations in normalized mean square strain (α) determined from mWH plot (based on Eqn.(2.30)) with ageing for SA, SA+10CW and SA+20CW 304HCu samples, respectively. As seen in Fig. 6.9(a) the microstrain (α) value for solution annealed and aged samples lie in the range of 0.001 to 0.002 and the change with ageing is insignificant. Due to the presence of coherent precipitates, a misfit (δ) is introduced in the matrix which is calculated from the difference in lattice parameter of coherent Cu precipitate phase (a_{Cu} ~3.604 Å) with respect to the lattice parameter of austenitic phase (a_γ) which changes with ageing as shown in Fig. 6.5. The misfit strain (ε) [**47**] for the misfit value (δ) is given by

$$\varepsilon = \frac{2}{3}\delta = \frac{4(a_{Cu} - a_\gamma)}{3(a_{Cu} + a_\gamma)}$$

On ageing the solution annealed samples for 22 h, the calculated misfit strain is ~ 0.001. It is observed that the microstrain value for SA and aged samples is similar to that of the misfit strain due to thermally induced precipitates. Bai et al. [**140**] have reported a misfit strain of 0.0005 in super 304H steel which is half the value estimated here. It is to be noted that the misfit strain due to BCC Cu precipitate in solution annealed 17-4 PH steel was reported as 0.018 which is close to the microstrain determined from mWH method [**47**].

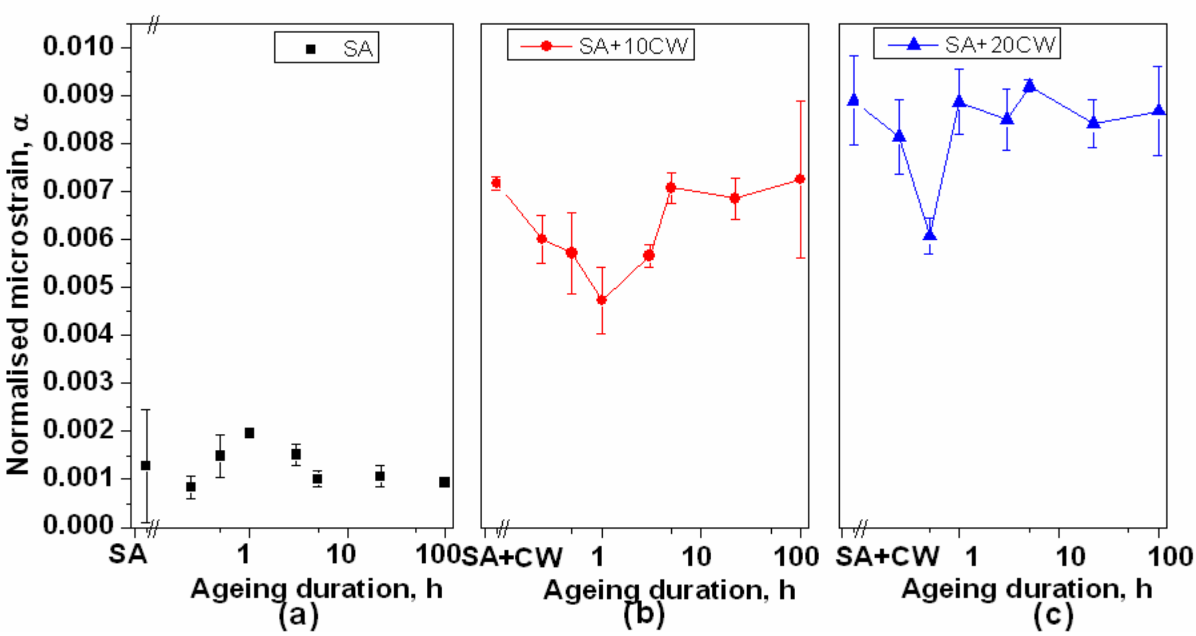

Fig. 6.9 The normalized mean square strain obtained from mWH method for (a) SA, (b) SA followed by 10% and (c) 20% cold worked samples.

6.3 Warren Averbach method

In addition to mWH method, the Warren Averbach (WA) method has been used for determination of mean square strain $\langle\varepsilon^2(L)\rangle$ as a function of column length (L). The Warren Averbach (WA) approach has been carried out using ordered peaks (111) and (222) reflections of the austenitic phase. Manojkumar et al. [**121**] have shown that the analysis of mean square strain $\langle\varepsilon^2(L)\rangle$ determined from WA can be expressed as a summation of three strain coefficients P_0, P_1 and P_2 as given in Eqn. (4.2). The term P_0 indicates strain field at longer column lengths, while P_1 and P_2 correspond to strain field with 1/L and $1/L^2$ dependency, respectively. These strain parameters are estimated by fitting $\langle \varepsilon^2(L) \rangle$ with Eqn. (4.2) for 10% and 20% cold worked and all aged samples. The coefficient of 1/L term, P_1 is linked to dislocation density. The dislocation density (ρ) is determined by using Williamson and Smallman approach ($\rho = 2\sqrt{3}\langle \varepsilon^2(L) \rangle^{1/2}/\boldsymbol{b}D$) wherein the microstrain (α) and crystallite size (D) obtained from mWH method are considered in estimating the dislocation density (ρ). Both short range strain field term P_1 and dislocation density (ρ) have been estimated for deformation modified and thermally aged 304HCu steel specimens.

6.3.1 Comparison of P_1 estimated from Fourier method with dislocation density (ρ)

Fig. 6.10 The variation of parameter P_1 determined from WA analysis with the change in dislocation density ρ for 10 and 20% cold worked 304HCu samples. Fig. 6.10 shows the variation of strain parameter P_1 and dislocation density (ρ) with ageing duration of prior deformed samples. The dislocation density decreases with ageing duration in both 10 and 20 % cold worked samples till 3 h and 0.5 h ageing duration, respectively. After reaching a minimum, an increase in dislocation density is observed which is attributed to formation of additional dislocations due to misfit between coherent precipitates and the matrix [**141**]. The observed variations in P_1 and ρ are in line with the observations made while studying the ageing behaviour of 17-4PH steel which were presented in § 4.8. Thus, the linear behaviour between P_1 and ρ validates the use of P_1 to monitor changes in dislocation density (ρ).

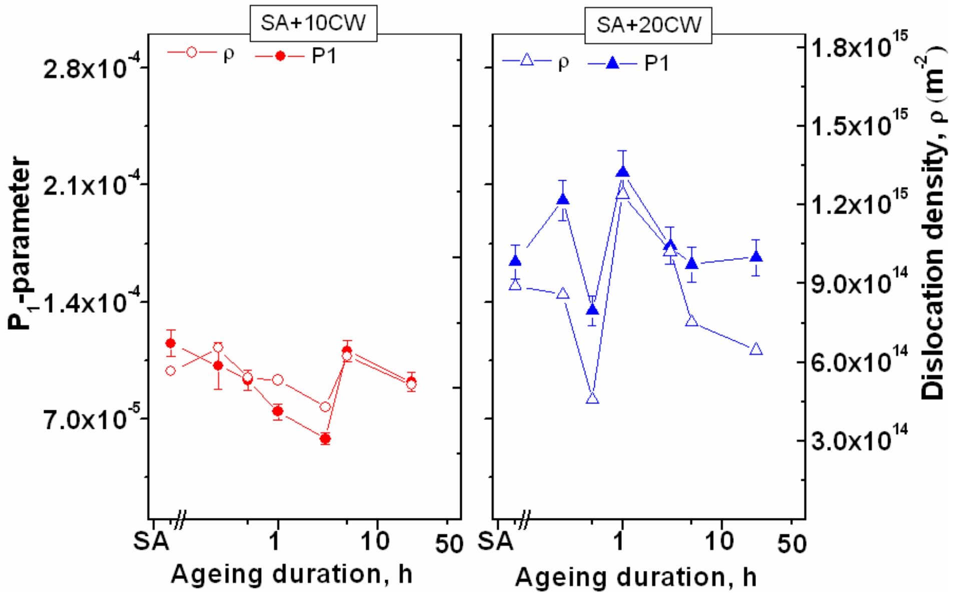

Fig. 6.10 The variation of parameter P_1 determined from WA analysis with the change in dislocation density ρ for 10 and 20% cold worked 304HCu samples.

6.4 Comparison of XRD parameters with electrical conductivity and hardness

6.4.1 Comparison of lattice parameter with conductivity

Changes in lattice parameter are directly linked to the change in volume of the unit cell of austenitic phase. In general, the change in volume per unit cell is directly related to the total volume fraction of all kinds of precipitates [**49**]. The change in volume per unit cell (ΔV) with thermal ageing of deformation modified austenitic steel is calculated as

$$\Delta V = |(a^3 - a_{SA}^3)| \quad \cdots \quad (6.2)$$

where a & a_{SA} represent the lattice parameters of thermally aged and un-aged 304HCu steel specimens under three different initial conditions, respectively. The change in volume (from Eqn. (6.2)) is given in Table 6.1. Since the observed variation in the volume of unit cell is similar to that of variations in conductivity (Refer to Fig. 5.4 in chapter 5), a plot is made between electrical conductivity and change in volume of unit cell as shown in Fig. 6.11. The effect of initial deformation is very marginal on both electrical conductivity and the volume of unit cell. (Kindly refer to figures in this chapter and earlier chapter for clarity). Please note that δV has been made zero in all 3 cases. However, ageing led to significant changes in volume of unit cell as well as electrical conductivity due to migration of precipitate forming alloying elements from the matrix. The higher electrical conductivity at same ageing duration in prior cold worked samples indicates formation of larger precipitation.

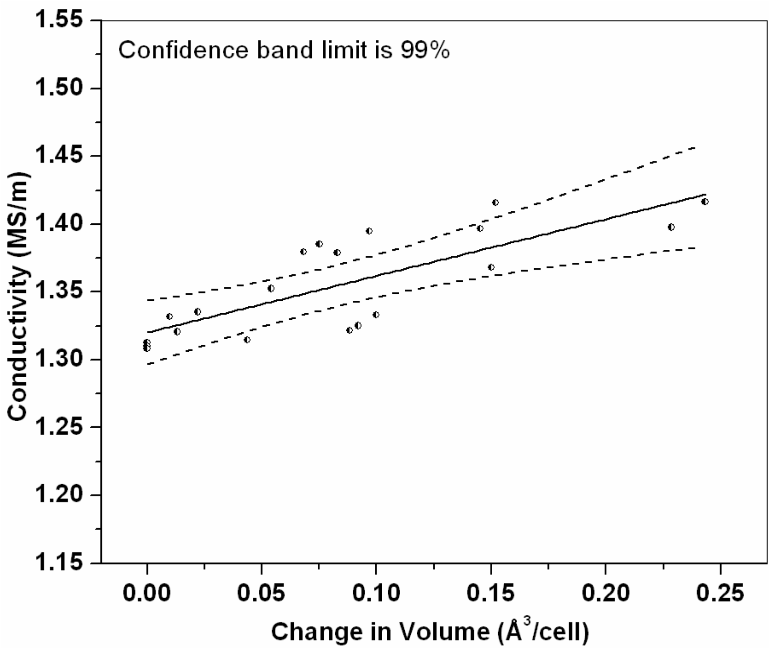

Fig. 6.11. The variation in conductivity with change in volume per unit cell of the matrix.

The electrical conductivity shows a linear correlation with the change in volume per unit cell of austenitic phase, as shown in Fig. 6.11. Thus, the observed variations in lattice parameter are in line with the conductivity changes and hence, it can be used for understanding the precipitation behaviour.

Table 6.1 The variation in change in volume of matrix phase with ageing duration for SA,SA+10% and SA+20% cold worked 304HCu steel

Thermal ageing duration (h)	Change in Volume (Å^3/cell)		
	Un-deformed samples (SA)	10% cold worked samples (SA+ 10CW)	20% cold worked samples (SA+ 20CW)
Un-aged	0	0	0
0.25	0.04365	0.0884	0.0920
0.5	0.01311	0.0998	0.0220
1	0.00989	0.0540	0.1499
3	0.0682	0.0830	0.1451
5	0.0751	0.0968	0.2285
22	0.07031	0.1519	0.2432

6.4.2 Comparison of microstrain with hardness

In addition to precipitation, changes in dislocation density takes place during thermal ageing of deformation modified 304HCu steels. In this study, the simultaneous influence of dislocation annihilation and precipitation is observed in the microstrain determined from mWH method. It should be noted that deformation induced dislocations increased the hardness of solution annealed sample (148 VHN) by ~ 100 VHN to 245 VHN as discussed in § 5.1.1. However, the change in hardness with precipitation due to ageing is ~ 30 VHN for prior cold worked samples. Thus, the contribution of deformation induced dislocations to strengthening is higher than that of precipitation strengthening. The observed variation in hardness due to deformation is similar to the variation observed in microstrain which increased from 0.002 to 0.007. In order to understand the dependency of precipitation and dislocation density with hardening, the microstrain from mWH method and hardness for SA, SA+10CW and SA+20CW aged for different ageing durations are plotted in Fig. 6.12. The microstrain is linearly correlated to hardness with a confidence limit of 98% which is clearly shown in Fig. 6.12.

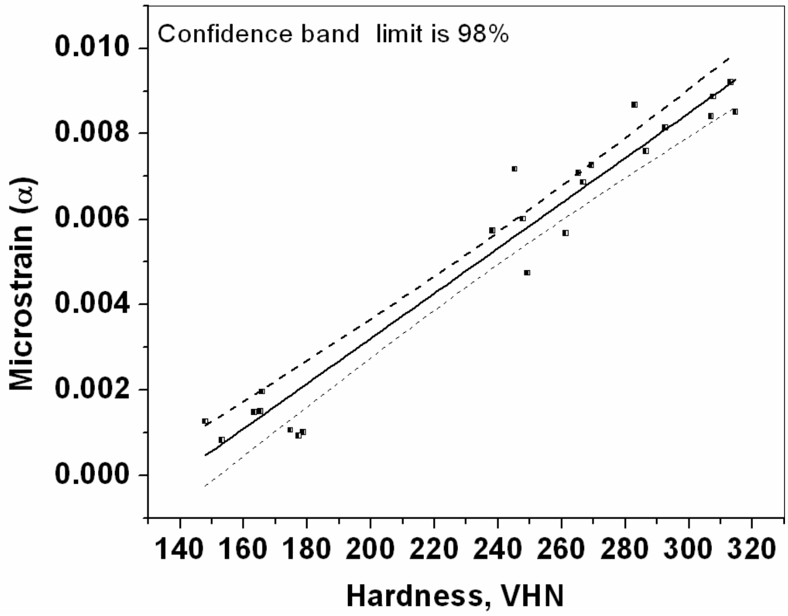

Fig. 6.12. The variation in microstrain with hardness measurements at different ageing durations with different initial conditions

6.5 Summary

The microstructural characterisation of prior deformed 304HCu steel during thermal ageing is achieved by determining lattice parameter, microstrain, hardness and electrical conductivity.

- The XRD line profile analysis has been successfully applied for characterizing the ageing behaviour of deformation modified 304HCu steel. The characterization is carried out by determination of lattice parameter, microstrain, dislocation density and strain parameter P_1.

- The larger change in lattice parameter in deformation modified 304HCu steel indicates that the precipitation gets accelerated with prior cold working aided by the dislocation nodes acting as nucleation sites.
- The decrease in lattice parameter with thermal ageing is linearly correlated with conductivity indicating the similar influence of precipitation process on conductivity and lattice changes.
- The comparative analysis of dislocation density ρ with parameter P_1 derived from WA method substantiates the 1/L dependency of strain due to dislocations as shown in chapter 4.
- On initial ageing of 10% and 20% deformation modified 304HCu steel, the microstrain decreases due to dislocation annihilation followed by an increase in microstrain due to the precipitation process.
- It is observed that the changes in hardness and microstrain are similar due to initial deformation and during ageing.

References

[1] H. M. Rietveld, "A profile refinement method for nuclear and magnetic structures," *J. Appl. Cryst.*, vol. 2, pp. 65-71, 1969.

[2] R. A. Young and D. B. Wiles, "Profile shape functions in Rietveld refinements," *J. Appl. Cryst.*, vol. 15, pp. 430-438, 1982.

[3] William Henry Bragg and William Lawrence Bragg, "The reflection of X-rays by crystals," in *Proc. R. Soc. Lond. A.*, vol. 88, pp. 428-438, 1913.

[4] W. Friedrich, P. Knipping, and M. V. Laue, "Interferenzerscheinungen bei Röntgenstrahlen "*Ann. der Physik*, vol. 346, pp. 971-988, 1913.

[5] P. Debye and P. Scherrer, "Interference of irregularly oriented particles in x-rays," *Physik. Z*, vol. 17, pp. 277-283, 1916.

[6] A. W. Hull, " A new method of X-ray crystal analysis" *Phys. Rev.*, vol. 10, pp. 661-696, 1917.

[7] V. I. Veksler, "A new method of accelerating relativistic particles," in *Comptes Rendus de l'Académie des Sciences de l'URSS*, vol. 43, pp. 346-348, 1944.

[8] Edwin M. McMillan, "The synchrotron-A proposed high energy particle accelerator," *Phys. Rev.*, doi: 10.1103/PhysRev.68.143, vol. 68, pp. 143-144, 1945.

[9] David J. Jackson and W.K.H. Panofsky, "Edwin Mattison Mcmillan," National academy of sciences, Washington D. C., Biographical Memoir, 1996.

[10] R. V. Nandedkar and G. Singh, "Indus-1 and Indus-2: Indian synchrotron radiation sources," *Synchrotron Radiation News*, vol. 16, pp. 43-48, 2003.

[11] Raja Ramanna Centre for Advanced Technology, Indus-2 (Booster-cum-storage ring). [Online]. http://www.rrcat.gov.in/technology/accel/indus2.html

[12] A. Borbély and T. Ungár, "X-ray line profiles analysis of plastically deformed metals," *C. R. Phys.*, vol. 13, pp. 293-306, 2012.

[13] J-L. Béchade, D. Menut, S. Doriot, S. Schlutig, and B. Sitaud, "X-ray diffraction analysis of secondary phases in zirconium alloys before and after neutron irradiation at the MARS synchrotron radiation beamline," *J. Nucl. Mater.*, vol. 437, pp. 365–372, 2013.

[14] B. D. Cullity and R. S. Stuart, *Elements of X-ray Diffraction.*: Prentice Hall, the University of Michigan, 2001.

[15] S. Vives, E. Gaffet, and C. Meunier, "X-ray diffraction line profile analysis of iron ball milled powders," *Mater. Sci. Eng., A*, vol. 366, pp. 229-238, 2004.

[16] K. Sanjay Rai, Anish Kumar, Vani Sankar, T. Jayakumar; K. Bhanu Sankar Rao, and Baldev Raj, "Characterization of microstructures in Inconel 625 using X-ray diffraction peak broadening and lattice parameter measurements," *Scr. Mater.*, vol.

51, pp. 59-63, 2004.

[17] S. Khan, S. D. Kaushik, A. Verma, J. B. Singh, V. Siruguri, and D. Srivastava, "Lattice parameter instabilities during multi-phase precipitation in Alloy 693," *J. Alloys Compd.*, vol. 700, pp. 149-154, 2017.

[18] L. Alexander and H. P. Klug, "Basic Aspects of X-Ray Absorption in Quantitative Diffraction Analysis of Powder Mixtures," *Anal. Chem.*, vol. 20, pp. 886-889, 1948.

[19] Eric Lifshin, Ed., *X-ray Characterization of Materials*.: John Wiley & Sons, USA, 1999.

[20] A. R. Stokes and A. J.C. Wilson, "The diffraction of X rays by distorted crystal aggregates - I," *Proc. Phys. Soc.*, vol. 56, pp. 174-181, 1944.

[21] T. Ungár, "Dislocation densities, arrangements and character from X-ray diffraction experiments," *Mater. Sci. Eng., A.*, vol. 309-310, pp. 14-22, 2001.

[22] C. P. Khattak and D. E. Cox, "Profile analysis of X-ray powder diffractometer data: structural refinement of La0.75Sr0.25CrO3," *J. Appl. Cryst.* , vol. 10, pp. 405-411, 1977.

[23] G. K. Wertheim, M. A. Butler, K. W. West, and D. N. E. Buchanan, "Determination of the Gaussian and Lorentzian content of experimental line shapes," *Rev. Sci. lnstrum.*, vol. 11, p. 1369, 1974.

[24] M. M. Hall, V. G. Veeraraghavan, H. Rubin, and P. G. Winchell, "The approximation of symmetric X-ray peaks by Pearson type Vll distributions.," *J. Appl. Cryst.*, vol. 10, p. 66, 1977.

[25] J. I. Langford, "A Rapid Method for Analysing the Breadths of Diffraction and Spectral Lines using the Voigt Function ," *J. Appl. Cryst.*, vol. 11, p. 10, 1978.

[26] J.I. Langford, "Some applications of pattern fitting to powder diffraction data," *Prog. Cryst. Growth and Charact.*, vol. 14, pp. 185-211, 1987.

[27] J. I. Langford, D. Louër, and P. Scardi, "Effect of a crystallite size distribution on X-ray diffraction line profiles and whole-powder-pattern fitting," *J. Appl. Cryst.*, vol. 33, pp. 964-974, 2000.

[28] P. Scardi and M. Leoni, "Whole Powder Pattern Modeling.," *Acta Cryst.*, vol. A58, pp. 190-200, 2002.

[29] G. Ribárik, T. Ungár, and J. Gubicza, "MWP-fit: a program for multiple whole-profile fitting of diffraction peak profiles by ab initio theoretical functions," *J. Appl. Cryst.*, vol. 34, no. 5, pp. 669-676, 2001.

[30] G. Ribárik, J. Gubicza, and T. Ungár, "Correlation between strength and microstructure of ball-milled Al–Mg alloys determined by X-ray diffraction.," *Mater. Sci. Eng., A*, vol. 387-389, pp. 343-347, 2004.

[31] Radomır Kuzel, "Kinematical diffraction by distorted crystals – dislocation X-ray line broadening," *Z. Kristallogr.*, vol. 222, pp. 136-149, 2007.

[32] G. K. Williamson and W. H. Hall, "X ray line braodening from filed aluminum and wolfram," *Acta Metall.*, vol. 1 , pp. 22-31, 1953.

[33] B. E. Warren and B. L. Averbach, "The separation of cold-work distortion and particle size broadening in X-ray patterns," *J. Appl. Phys.*, vol. 23, p. 497, 1952.

[34] S. Enzo, G. Fagherazzi, A. Bendetti, and S. Polizzi, "A profile -fitting procedure for analysis of broadened X-ray diffraction," *J. Appl. Cryst.*, vol. 21, pp. 536-542, 1988.

[35] Davor Balzar and Hassel Ledbetter, "Voigt-Function Modeling in Fourier analysis of size and strain broadened X -ray diffraction peaks," *J. Appl. Cryst.*, vol. 26, pp. 97-103, 1993.

[36] T. Ungár and A. Borbély, "The effect of dislocation contrast on x-ray line broadening: A new approach to line profile analysis," *Appl. Phys. Lett.*, vol. 69, no. 21 , pp. 3173-3175, 1996.

[37] Th. H. de Keijser, J. I. Landford, E. J. Mittemeijer, and A. B. P. Vogels, "Use of the Voigt function in a single-line method for the analysis of X-ray diffraction line broadening," *J. Appl. Cryst.*, vol. 15, pp. 308-315, 1982.

[38] J. N. Eastabrook and A. J. C. Wilson, " The diffraction of X-rays by distorted-crystal aggregates III: remarks on the interpretation of the fourier coefficients," *Proc. Phys. Soc., B*, vol. 65, pp. 67-75, 1952.

[39] M Tournarie, "Utilisation du 2nd moment comme critere delargissement des raies debye-scherrer," *C. R. Acad. Sci. Paris;*, vol. 242, p. 2161, 1956.

[40] A. J. C. Wilson, "On variance as a measure of line broadening in duffractometry. II: Mistakes and Strain," *Proc. Phys. Soc.*, vol. 81, pp. 41-46, 1963.

[41] R. K. Nandi and Sen Gupta S. P., "The analysis of X-ray diffraction profiles from imperfect solids by an application of convolution relations," *J.Appl. Cryst.*, vol. 11, pp. 6-9, 1978.

[42] R. K. Nandi, H. K. Kuo, W. Schlosberg, G. Wissler, J. B. Cohen, and B. Crist JR., "Single peak methods for Fourier analysis of peak shapes," *J. Appl. Cryst.*, vol. 17, pp. 22-26, 1984.

[43] Bojan Marinkovic, Roberto Ribeiro de Avillez, Alvaro Saavedra, and Fernando Cosme Rizzo Assuncao, "A comparison between the Warren-Averbach method and alternate methods for X-Ray Diffraction microstructure analysis of polycrystalline specimens," *Mater. Res.*, vol. 4, no. 3, pp. 71-76, 2001.

[44] J. Ghosh, S. K. Chattopadhayay, A. K. Meikap, and S. K. Chatterjee, "Microstructure characterization of titanium-base aluminium alloys by x-ray diffraction using Warren-Averbach and Rietveld method," *J. Alloys Compd.*, vol. 453, pp. 131-137, 2008.

[45] R. W. Cheary and A. Coelho, "A fundamental parameters approach to X-ray line-profile fitting," *J. Appl. Cryst.*, vol. 25, pp. 109-121, 1992.

[46] George E Dieter, *Mechanical Metallurgy*.: McGraw Hill Education, 1989.

[47] S. Mahadevan, R. Manojkumar, T. Jayakumar, C. R. Das, and B. P.C. Rao, "Precipitation induced changes in microstrain and its relation with hardness and tempering parameter in 17-4 PH stainless steel," *Metall. Mater. Trans. A*, vol. 47A, pp. 3109-3118, 2016.

[48] H. Mirzadeh and A. Najafizadeh, "Aging kinetics of 17-4PH stainless steel," *Mater. Chem. Phys.*, vol. 116, pp. 119-124, 2009.

[49] S. Mahadevan, "X-ray diffraction based characterization of ageing behaviour of precipitation hardenable steels," Homi bhabha national institute, Indira Gandhi Centre for Atomic Research, Kalpakkam, Doctor of philosophy, Doctor of philosophy, http://www.hbni.ac.in/students/dsp_ths.html?nm=engg/ENGG02200804019.pdf, 2015.

[50] Vijay K. Vasudevan, Sung J. Kim, and C. Marvin Wayman, "Precipitation reactions and strengthening behavior in 18 wt pct Nickel maraging steels," *Metall. Trans. A*, vol. 21, pp. 265-2668, 1990.

[51] D. K. Bhattacharya, T. Jayakumar, V. Moorthy, and S. Vaidyanathan, "Characterization of microstructures in 17-4-PH stainless steel by magnetic Barkhausen noise analysis," *NDT&E INT*, vol. 26, pp. 141-148, 1993.

[52] K. V. Rajkumar, Anish Kumar, T. Jayakumar, B. Raj, and K. K. Ray, "Characterization of Aging Behavior in M250 Grade Maraging Steel Using Ultrasonic Measurements," *Metall. Mater.Trans. A.*, vol. 38A, pp. 236-243, 2007.

[53] S. Mahadevan, T. Jayakumar, B.P.C. Rao, Anish Kumar, K.V. Rajkumar, and Baldev Raj, "X-Ray Diffraction Profile Analysis for Characterizing Isothermal Aging Behavior of M250 Grade Maraging Steel," *Metall. Mater. Trans. A*, vol. 39A, pp. 1978-1984, 2008.

[54] Z. Guo, W. Sha, and D. Li, "Quantification of phase transformation kinetics of 18 wt.% Ni C250 maraging steel.," *Mater. Sci. Eng., A.*, vol. 373, pp. 10-20, 2004.

[55] U. K. Viswanathan, S. Banerjee, and R. Krishnan, "Effects of aging on the microstructure of 17-4 PH Stainless Steel," *Mater. Sci. Eng., A*, vol. 104, pp. 181-189, 1988.

[56] U. K. Viswanathan, P. K. K. Nayar, and R. Krishnan, "Kinetics of precipitation in 17–4 PH stainless steel," *Mater. Sci. Technol.*, vol. 5, no. 4, pp. 346-349, 1989.

[57] Shigeharu Ukai, Shunji Mizuta, Masayuki Fujiwara, Takanari Okuda, and Toshimi Kobayash, "Development of 9Cr-ODS martensitic steel claddings for fuel pins by means of ferrite to austenite phase transformation," *J. Nucl. Sci. Technol.*, vol. 39, pp. 778-788, 2002.

[58] N. Sallez, X. Boulnat, A. Borbely, J. L. Bechade, D. Fabregue, M. Perez, Y. Carlan de, L. Hennet, C. Mocuta, D. Thiaudiere, and Y. Brecheta, "In situ characterization of microstructural instabilities: Recovery,recrystallization and abnormal growth in nanoreinforced steel powder," *Acta Mater.*, vol. 87, pp. 377-389, 2015.

[59] R. Viswanathan and W. Bakker, "Materials for Ultrasupercritical Coal Power Plants—

Boiler Materials: Part 1," *J. Mater. Eng. Perform.*, vol. 10, p. 83, 2001.

[60] Chengyu Chi, Hongyao Yu, Jianxin Dong, Xishan Xie, Zhengqiang Cui, Xiaofang Chen, and Fusheng Lin, "Strengthening effect of Cu-rich phase precipitation in 18Cr9Ni3CuNbN austenitic heat-resisting steel," *Acta Metall. Sinica*, vol. 24, no. DOI: 10.11890/1006-7191-112-141, pp. 141-147, 2011.

[61] Manmathkumar Dash, T. Karthikeyan, R. Mythili, V.D. Vijayanand, and S. Saroja, "Effect of Long-Term Thermal Exposures on Microstructure and Impression Creep in 304HCu Grade Austenitic Stainless Steel," *Metall. Mater. Trans. A*, vol. 48A, pp. 4883-4894, 2017.

[62] Jun Jiang and Lihui Zhu, "Strengthening mechanisms of precipitates in S30432 heat-resistant steel during short-term ageing," *Mater. Sci. Eng., A*, vol. 539, pp. 170-176, 2012.

[63] A. Iseda, H. Okada, H. Semba, and M. Igarashi, "Long term creep properties and microstructure of SUPER304H, TP347HFG and HR3C for A-USC boilers," *Energy Materials*, vol. 2, pp. 199-206, 2007.

[64] V. Ganesan, K. Laha, and A. K. Bhaduri, "Creep rupture properties of indigenously developed 304HCu austenitic stainless steel," *Trans. Indian Inst. Met.*, vol. 69, pp. 247-251, 2016.

[65] Xiang Huang, Qingwen Zhou, Wei Wang, Wen Sheng Li, and Yan Gao, "Microstructure and property evolutions of a novel Super304H steel during high temperature creeping," *Mater. High Temp.*, vol. 35, pp. 438-450, 2017.

[66] Ling Ren, Li Nan, and Ke Yang, "Study of copper precipitation behavior in a Cu-bearing austenitic antibacterial stainless steel," *Mater. Des.*, vol. 32, pp. 2374-2379, 2011.

[67] D. F. Lahrman, R. D. Field, R. Darolia, and H. L. Fraser, "Investigation of techniques for measuring lattice mismatch in a rhenium containing nickel base superalloy," *Acta metall.*, vol. 36, pp. 1309-1320, 1988.

[68] T. Ungar, Ashok Choudhary, A. k. Mukharjee, and P. Szucs, "Creep behaviour of a Cr-Mo-V steel after seventeen years of service," *J. Mater. Sci.*, vol. 25, pp. 905-908, 1990.

[69] C. C. Tang, P. A. Lynch, R. W. Cheary, and S. M. Clark, "An in situ method for the study of strain broadening using synchrotron X-ray diffraction," *J. Appl. Cryst.*, vol. 40, pp. 642-649, 2007.

[70] Jun-Li, Kun Mo, Di Yun, Yinbin Miao, Xiang Liu, Huijuan Zhao, David T. Hoelzer, Jun-Sang Park, Jonathan Almer, Guangming Zhang, Zhangjian Zhou, James F. Stubbins, and Abdellatif M. Yacout, "In situ synchrotron tensile investigations on 14YWT, MA957, and 9-Cr ODS alloys," *J. Nucl. Mater.*, vol. 471, pp. 289-298, 2016.

[71] Tatyana Vershinina and Maria Leont'eva-Smirnova, "Dislocation density evolution in the process of high-temperature treatment and creep of EK-181 steel," *Mater. Charact.*, vol. 125, pp. 23-28, 2017.

[72] E.O. Hall, "The deformation and ageing of mild stee l: III Discussion of results," *Proc. Phys. Soc. B*, vol. 64, pp. 747-753, 1951.

[73] N.J. Petch, "The cleavage strength of polycrystals.," *J. Iron Steel Inst.*, vol. 174, pp. 25-28, 1953.

[74] J. C. M. Li, "Petch relation and grain boundary sources.," *Trans. Metall. Soc. AIME*, vol. 227, pp. 239-247, 1963.

[75] V. Gerold and H. Haberkorn, "On the critical resolved shear stress of solid solutions containing coherent precipitates," *Phys. Status Solidi.*, vol. 16, no. 675-684, 1966.

[76] P. M. Kelly, "The quantitative relationship between microstructure and properties in two phase alloys," *Int. Metall. Rev.*, vol. 18, pp. 31-36, 1973.

[77] M. Vasudevan, S. Venkadesan, P. V. Sivaprasad, and L. S. Mannan, "Use of the Larson-Miller parameter to study the influence of ageing on the hardness of cold-worked austenitic stainless steel," *J. Nucl. Mater.*, vol. 211, pp. 251-255, 1994.

[78] K. V. Rajkumar, Anish Kumar, T. Jayakumar, B. Raj, K. K. Ray, "Characterization of aging behaviour in M250 grade maraging steel using eddy current non-destructive methodology," *Mater. Sci. Eng., A*, vol. 464, pp. 233–240, 2007.

[79] J. Lendvai, T. Ungár, I. Kovács, and G. Groma, "Correlation between resistivity increment and volume fraction of G.P. zones in an Al-3·2 wt % Zn-2·2 wt % Mg alloy," *Philos. Mag.*, vol. 33, pp. 209-212, 1976.

[80] R. Manojkumar, S. Mahadevan, A. Viswanath, S. ArunKumar, B. Purna Chandra Rao, and K. V. Rajkumar, "Application of electrical conductivity as an nde tool for microstructural evolution during cold rolling and thermal ageing," in *Indian National Seminar and Exhibition on Non Destructive Evaluation NDE-2015*, Hyderabad, 2015.

[81] B. Dutta, E. J. Palmier, and C. M. Sellars, "Modelling the kinetics of strain induced precipitation in Nb microalloyed steels," *Acta mater.*, vol. 49, pp. 785-794, 2001.

[82] Sung-Min Hong, Myung-Yeun Kim, Dong-Joon Min, Kyu-ho Lee, Jae-Hyeok Shim, Dong-Ik Kim, Jin-Yoo Suh, Woo-Sang Jung, and In-Suk Choi, "Unraveling the origin of strain-induced precipitation of M23C6 in the plastically deformed 347 Austenite stainless steel," *Mater. Charact.*, vol. 94, pp. 7-13, 2014.

[83] P. Suortti, M. Ahtee, and L. Unonius, "Voigt function fit of X-ray and neutron powder diffraction profiles," *J. Appl. Cryst.*, vol. 12, pp. 365- 369, 1979.

[84] J. M. Adams and A. W. Hewat, "Hydrogen atom positions in dickite," *Clays Clay Miner.*, vol. 29, pp. 316-319, 1981.

[85] S.A. Howard and R.L. Snyder, "An evaluation of some profile models and the optimization procedures used in profile fitting," *Adv. in X-ray Anal.*, vol. 26, pp. 73-81, 1983.

[86] W. I. F. David and J. C. Matthewman, "Profile refinement of powder diffraction patterns using the Voigt function," *J. Appl. Cryst.*, vol. 18, p. 461, 1985.

[87] Prabal Dasgupta, "On use of pseudo-Voigt profiles in diffraction line broadening analysis," *Fisika A*, vol. 9, pp. 61-66, 2000.

[88] C. G. Darwin, "XXXIV The theory of X-ray reflexion," *Philos. Mag. series 6*, vol. 27, pp. 315-333, 1914.

[89] G. Caglioti, A. Paoletti, and F.P. Ricci, "Choice of collimators for a crystal spectrometer for neutron diffraction," *Nucl. Instrum. Methods*, vol. 3, p. 223, 1958.

[90] P. Scherrer, " Bestimmung der Größe und der inneren Struktur von Kolloidteilchen mittels Röntgenstrahlen," *Nachr. Ges. Wiss. Göttingen.*, vol. 26, pp. 98-100, 1918.

[91] H. P. Klug and L. E. Alexander, *X-Ray Diffraction Procedures*.: Wiley publisher, the University of California, USA, 1974.

[92] J. I. Langford and A. J. C. Wilson, "Scherrer after sixty years: A survey and some new results in the determination of crystallite size," *J. Appl. Cryst.*, vol. 11, 1978.

[93] J. Aitchison and J. A. C. Brown, *The lognormal distribution*. Cambridge, England: Cambridge University press, 1957.

[94] T. Ungár, "The meaning of size obtained from broadened X-ray diffraction peaks," *Adv. Eng. Mater.*, vol. 5, pp. 323-329, 2003.

[95] T. Ungar, "Microstructural parameters from X-ray diffraction peak," *Scr. Mater.*, vol. 51, pp. 777-781, 2004.

[96] M. A. Krivoglaz and K. P. Ryaboshapka, "Theory of X-ray scattering by crystals containing dislocations," *Phys. Met. Metall.*, vol. 15, pp. 18–31, 1963.

[97] M. Wilkens, "The mean square stress for restrictedly random distributions of dislocations in a cyclindrical body," *Acta Metall.*, vol. 17, pp. 1155-1159, 1969.

[98] M. Wilkens, "Theoretical aspects of kinematical X-ray diffraction profiles from crystals containing dislocation distributions," in *Fundamental aspects of dislocation theory*, Washington, DC, USA, pp. 1195-1221, 1970.

[99] M. Wilkens, "The determination of density and distribution of dislocations in deformed single crystals from broadening X-ray diffraction profiles," *Phys. Status Solidi A*, vol. 2, pp. 359-370, 1970.

[100] I. Gaál, *Acta Phys. Acad. Sci. Hung.*, vol. 33, pp. 411-418, 1973.

[101] N. C. Halder and C. N. J. Wagner, "Separation of particle size and lattice strain in integral breadth measurements," *Acta Cryst.*, vol. 20, pp. 312-313, 1966.

[102] Rajan Bhambroo, S. Roychowdhury, Vivekananda kain, and V. S. Raja, "Effect of reverted austenite on mechanical properties of precipitation hardenable 17-4 stainless steel," *Mater. Sci. Eng., A*, vol. 568, pp. 127-133, 2013.

[103] B. E. Warren, *X-ray Diffraction*.: Addison-Wesley, New York, USA, 1969.

[104] M. A. Krivoglaz, *Theory of X-Ray and Thermal Neutron Scattering by Real Crystals*.:

Springer-Verlag, Berlin, 1996.

[105] I. Groma, T. Ungar, and M. Wilkens, "Asymmetric X-ray Line Broadening of Plastically Deformed Crystals. I.Theory," *J. Appl. Cryst.*, vol. 21, pp. 47-53, 1988.

[106] J. Rodriguez-Carvajal, M. T. Fernandez-Diaz, and J. L. Martinez, "Neutron diffraction study on structural and magnetic properties of La2NiO4," *J. Phys. Condens. Mater.*, vol. 3, pp. 3215-3234, 1991.

[107] N. C. Popa, "The (hkl) dependence of diffraction-line broadening caused by strain and size for all Laue groups in Rietveld refinement," *J.Appl.Cryst.*, vol. 31, pp. 176-180, 1998.

[108] Peter W. Stephens, "Phenomenological model of anisotropic peak broadening in powder diffraction," *J. Appl. Cryst.*, vol. 32, pp. 281-289, 1999.

[109] T. Ungár and G. Tichy, "The effect of dislocation contrast on X-Ray line profiles in untextured polycrystals," *Phys. Status Solidi. A*, vol. 171, pp. 425-434, 1999.

[110] T. Ungár, I. Dragomir, Á. Révész, and A. Borbély, "The contrast factors of dislocations in cubic crystals: the dislocation model of strain anisotropy in," *J. Appl. Cryst.*, vol. 32, pp. 992-1002, 1999.

[111] T. Ungar, J. Gubicza, G. Ribarik, and A. Borbely, "Crystallite size distribution and dislocation structure determined by diffraction profile analysis: principles and practical application to cubic and hexagonal crystals," *J. Appl. Cryst.*, vol. 34, pp. 298-310, 2001.

[112] S.A. Howard and R.L. Snyder, "The use of direct convolution products in profile and pattern fitting algorithms. I. Development of the algorithms," *J. Appl. Cryst.*, vol. 22, pp. 238-243, 1989.

[113] J. Birkenstock, R. X. Fischer, and T. Messner. http://www.brass.uni-bremen.de, 2005.

[114] P. Scardi and M. Leoni, "Fourier modelling of the anisotropic line braodening of X ray diffraction profiles due to line and plane lattice defects," *J. Appl. Cryst.*, vol. 32, pp. 671-682, 1999.

[115] A. C. Larson and R. B. Von Dreele, "General Structure Analysis System (GSAS)," Los Alamas National Labouratory Report Laur, 2004.

[116] J. Rodriguez-Carvajal, "Reference guide for the computer program FullProf.," Laboratoire Leon Brillouin (CEA-CNRS), 1996.

[117] M. Leoni and P. Scardi, "A computer program for structural refinement from thin film XRD patterns," *Mater. Sci. Forum*, vol. 278-281, pp. 177-182, 1998.

[118] M. Avrami, "Granulation, phase change, and microstructure," *J. Chem. Phys.*, vol. 9, pp. 177-184, 1941.

[119] S. A. Arrhenius, "Über die dissociations wärme und den einfluß der temperatur auf den dissociationsgrad der elektrolyte," *Z. Phys. Chem.*, vol. 4, pp. 96-116, 1889.

[120] A. K. Sinha, Archna Sagdeo, Pooja Gupta, Anuj Upadhyay, Ashok Kumar, M. N.

Singh, R. K. Gupta, S. R. Kane, A. Verma, and S. K. Deb, "Angle dispersive x-ray diffraction beamline on indus-2 synchrotron radiation source: commissioning and first results," *J. Phys. Conf. Ser.*, vol. 425, p. 072017, 2013.

[121] R. Manojkumar, S. Mahadevan, C. k. Mukhopadhyay, and B. P. C. Rao, "Aging behavior of 17-4 PH stainless steel studied using XRDLPA for separating the influence of precipitation and dislocations on microstrain," *J. Mater. Res.*, vol. 32, pp. 4263-4271, 2017.

[122] G. K. Williamson and R. E. Smallman, "Dislocation densities in some annealed and cold-worked metals from measurements on the X-ray Debye-Scherrer spectrum," *Philos. Mag.*, vol. 1, pp. 34-46, 1956.

[123] R. L. Rothman and J. B. Cohen, "X-Ray study of faulting in BCC metals and alloys," *J. Appl. Phys.*, vol. 42, no. 3, pp. 971-979, 1971.

[124] J.G.M. Van Berkum, A.C. Vermeulen, R. Delhez, H. De Keijser, and E. J. Mittemeijer, "Applicabilities of the Warren-Averbach analysis and an alternative analysis for separation of size and strain broadening," *J. Appl. Cryst.*, vol. 27, pp. 345-357, 1994.

[125] Sato Shigeo, Takahashi Yohei, Wagatsuma Kazuaki, and Suzuki Shigeru, "Characterization of aging behavior of precipitates and dislocations in copper-based alloys," *Powder Diffr*, pp. 104-107, 2010.

[126] T. Shintani and Y. Murata, "Evaluation of the dislocation density and dislocation character in cold rolled Type 304 steel determined by profile analysis of X-ray diffraction," *Acta Mater.*, vol. 59, pp. 4314-4322, 2011.

[127] Jun Jiang and Lihui Zhu, "Strengthening mechanisms of precipitates in S30432 heat-resistant steel during short-term ageing," *Mater. Sci. Eng., A*, vol. 539, pp. 170-176, 2012.

[128] X. Wang, Y. Li, D. Chen, and J. Sun, "Precipitate evolution during the aging of Super304H steel and its influence on impact toughness," *Mater. Sci. Eng. A*, vol. 754, pp. 238-245, 2019.

[129] N. Kauss, T. Halle, and P. Rosemann, "Age-hardening behaviour, microstructure and corrosion resistance of the copper alloyed stainless steel 1. 4542," *IOP Conf. Ser.: Mater. Sci. Eng.*, vol. 373, p. 012020, 2018.

[130] C. V. Robino, P. W. Hochanadel, G. R. Edwards, and M. J. Cieslak, "Heat Treatment of Investment Cast PH 13-8 Mo Stainless Steel: Part II. Isothermal Aging Kinetics," *Metall. Mater. Trans. A*, vol. 25A, pp. 697-704, 1994.

[131] Qingwen Zhou, Shaobo Ping, Xiaobo Meng, Ruikun Wang, and Yan Gao, "Precipitation kinetics of M23C6 carbides in the super304H austenitic heat-resistant steel," *J. Mater. Eng. Perform.*, vol. 26, pp. 6130–6139, 2017.

[132] Ling Ren, Jinming Zhu, Li Nan, and Ke Yang, "Differential scanning calorimetry analysis on Cu precipitation in a high Cu austenitic stainless steel," *Mater.Des.*, vol. 32, pp. 3980-3985, 2011.

[133] Ying-hui Zhou, Chen-xi Liu, Yong-chang Liu, Qian-ying Guo, and Hui-jun Li, "Coarsening behavior of MX carbonitrides in type 347H heat-resistant austenitic steel during thermal aging," *Int. J. Miner. Metall. Mater.*, vol. 23, pp. 283-293, 2016.

[134] Ernst Kozeschnik, *Modeling Solid-State Precipitation.*: Momentum Press, New york, USA, 2013.

[135] C.Y. Chi, H.Y. Yu, J. X. Dong, W. Q. Liu, S. C. Cheng, Z. D. Liu, and X. S. Xie, "The precipitation strengthening behavior of Cu-rich phase in Nb contained advanced Fe–Cr–Ni type austenitic heat resistant steel for USC power plant application," *Prog. Nat. Sci.: Mater. Int.*, vol. 22, pp. 175-185, 2012.

[136] "JCPDS-International Centre for Diffraction Data, ICDD card no 04-009-2090,".

[137] A. Boeuf, C. Crico, R. caciuffo, F. Rustechelli, I. Pomot, G. Uny, "Effect of M23C6 precipitation on the latttice parameter of AISI 304 stainless steel," *Mater. Lett.*, vol. 3, pp. 115-118, 1985.

[138] Chengyu Chi, Hongyao Yu, and Xishan Xie, "Advanced Austenitic Heat-Resistant Steels for Ultra-SuperCritical (USC) Fossil Power Plants," in *Alloy Steel - Properties and Use*, Dr. Eduardo Valencia Morales, Ed. Croatia : InTech, pp. 171-200, 2011.

[139] H. M. Ledbetter, "Predicted monocrystal elastic constants of 304-type stainless steel," *Phys. B*, vol. 128, pp. 1-4, 1985.

[140] J. W. Bai, P. P. Liu, Y. M. Zhu, X. M. Li, C. Y. Chi, H. Y. Yu, X. S. Xie, and Q. Zhan, "Coherent precipitation of copper in Super304H austenite steel," *Mater. Sci. Eng. A*, vol. 584, pp. 57-62, 2013.

[141] J. W. Martin, *Micromechanisms in particle-hardened alloys*.: Cambridge University Press, New York, NY, 1980.

Thesis Highlights

Name of the Student: Manoj Kumar Raja

Name of CI: Indira Gandhi Centre for Atomic Research**Enrolment No.:** ENGG 02 2011 04029

Thesis Title: *XRD line profile analysis for understanding the influence of cold work on ageing behaviour in 304HCu steel*

Discipline: Engineering Sciences **Sub-Area of Discipline:** XRD and NDT

Date of viva voce: 30/04/2021

The 304HCu steel is a Cu modified austenitic heat resistant stainless steel used for high temperature boiler tube applications. It has high strength and creep resistance due to formation of fine Cu-rich phases; $M_{23}C_6$ and MX type carbonitrides during ageing. To study the influence of cold work on precipitation behavior, 304HCu steel is solution annealed (SA) followed by cold worked (CW) for 10% and 20% reduction in thickness and isothermally aged at 650 °C. The CW 304HCu steel during isothermally ageing are characterized by using XRD technique, hardness and electrical conductivity measurements.

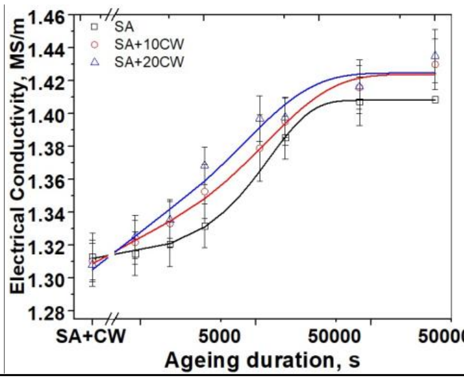

Fig. 1 Variation of conductivity with ageing for SA, 10% and 20% CW.

The changes in hardness and electrical conductivity (σ) with ageing are fitted with Johnson-Mehl-Avrami equation. The hardness increases due to both CW and ageing. However, the σ shows no change due to cold working but it increases with ageing as shown in Fig. 1. The early peaking of σ in CW samples is attributed to accelerated precipitation kinetics. The change in kinetics of σ due to 10% and 20% deformation is equated to an apparent change in activation energy of 0.73 and 4.225 kJ/mol and as an equivalent increase in ageing temperature of 654 and 672 °C respectively.

The microstrain estimated from various XRD line profile analyses (XRDLPA) viz. modified Williamson Hall (mWH) method, Warren-Averbach (WA) method and Stephens phenomenological model are compare for isothermally aged 17-4 precipitation hardenable steel. To separate the effects due to precipitation and dislocations on microstrain, the column length dependency of microstrain from WA analysis is proposed with the equation: $<\varepsilon^2(L)> = P_0+P_1/L+P_2/L^2$ --[1] where P_0 - long range strain parameter and (P_1 & P_2) - short range strain parameters. The parameters P_0 and P_1 are correlated with microstrain (α) determined from mWH method and dislocation density (ρ) determined from Williamson-Smallman method respectively as shown in Fig.2. This indicates the simultaneous effects due to precipitates and dislocations are separated by determining P_0 and P_1 terms.

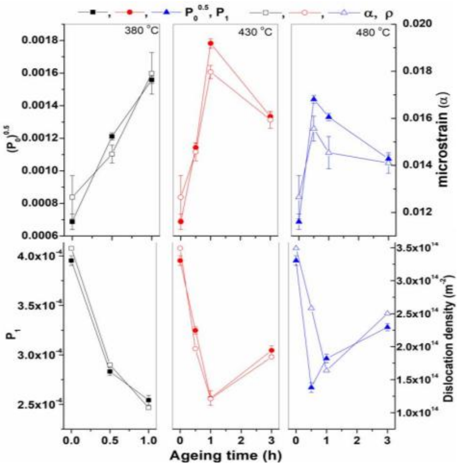

Fig. 2. shows linear behavior of $(P_0)^{0.5}$ with α and P_1 with ρ respectively.

Further, the XRD profiles obtained from synchrotron source for prior CW 304HCu steel has revealed variation in lattice parameter and microstrain with ageing. A reduction in lattice parameter with ageing is observed due to migration of precipitate forming elements from the matrix and it is higher for cold worked samples due to enhanced precipitation on dislocations. The variation in α determined from mWH method with ageing of prior cold worked 304HCu steel showed dominant dislocation annihilation effects on initial ageing and dominant precipitation effects on further ageing as shown in Fig. 3. Further, the microstrain obtained from WA analysis fitted with proposed Eqn-[1] has revealed linear behavior between P_1 and ρ.

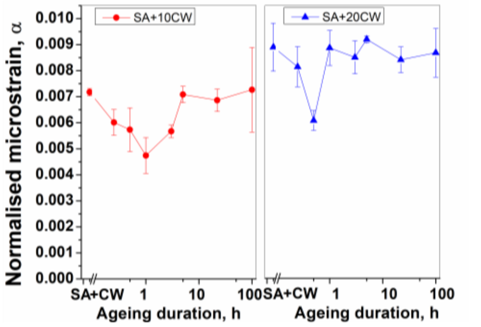

Fig. 3. Variation of normalized microstrain (α) with ageing for 10% and 20% CW 304HCu steel.